2011

Localized Damage Detection in Structures: A Statistics Based Algorithm Using a Densely Clustered Sensor Network

Elizabeth L. Labuz
Lehigh University

Localized Damage Detection in Structures:

A Statistics Based Algorithm Using a Densely Clustered Sensor Network

by

Elizabeth L. Labuz

A Thesis

Presented to the Graduate and Research Committee

of Lehigh University

in Candidacy for the Degree of

Master of Science

in

Structural Engineering

Lehigh University

May, 2011

This thesis is accepted and approved in partial fulfillment for the requirements of the Master of Science in Structural Engineering.

_____
Date

_____
Dr. Shamim N. Pakzad
Thesis Advisor

_____
Dr. Stephen Pessiki
Department of Civil and Environmental Engineering

Acknowledgments

This research was conducted at the Advanced Technology for Large Structural Systems (ATLSS) Research Center at Lehigh University in Bethlehem, PA, USA. Research funding is partially supported by the National Science Foundation through Grant No. CMMI-0926898 by Sensors and Sensing Systems program, and by a grant from the Commonwealth of Pennsylvania, Department of Community and Economic Development, through the Pennsylvania Infrastructure Technology Alliance (PITA). This financial support is gratefully acknowledged.

I would like to thank my thesis advisor, Dr. Shamim N. Pakzad, for his mentorship and guidance throughout my master's studies. The support provided by John Hoffner and the ATLSS laboratory instrumentation and technician staff were invaluable in the construction of my experimental specimens and the completion of testing. The computer technical support provided by Peter Bryan is much appreciated. I would like to acknowledge Dr. James Ricles, Ian Hodgson, and the people at SidePlate for allowing us to instrument the earthquake moment connections. I am grateful for the assistance provided by my research mentees throughout this process: Diane Wurst, Carrie Sporck, Gregory Stolowski, Kelsey Sheridan, Mallory Nigro, and Andrew Moss. Thanks are also extended to my fellow graduate students, especially Siavash Dorvash, for their assistance with many technical and nontechnical challenges.

Finally, thank you to my family and friends, especially Brian LaCrosse, for their continued love and support throughout this journey.

Table of Contents

List of Tables

List of Figures

Abstract

In order to maintain healthy structures, it is important to find means of Structural Health Monitoring (SHM) that are effective, economical, and easy to implement. In this thesis, a promising localized damage detection method is proposed. This output-only method uses structural responses collected from densely instrumenting a structure. It then applies linear regression analysis to relate responses of pair-wise nodes within the sensor network. The resulting influence coefficients become damage indicators when they reflect a deviation from the baseline healthy-state coefficients. Two parameters, evaluation accuracy and normalized estimation error, are introduced to assess the reliability of each coefficient to identify the most effective damage indicators. Furthermore, a statistical framework is adopted to monitor the change point of the influence coefficients over time in order to identify damage to a 95% confidence level.

Performance evaluation of the proposed method is achieved through application to two simulated models and three experimental specimens tested at Lehigh University's ATLSS Center. The first experimental prototype consists of a simple beam-column connection that represents a local joint in a structure. Experimental results are collected using parallel wired and wireless sensor networks to verify not only the performance of the detection algorithm, but also the effectiveness of the wireless sensor network. Damage is identified statistically by applying the hypothesis testing framework to the influence coefficients.

The second model is designed for representation of either a building frame or a bridge girder, taking the form of a two-bay, uneven span frame. The frame is densely

instrumented with 21 wired accelerometers for dynamic testing and 6 linear variable displacement transducers (LVDTs) for static testing. Both simulations and preliminary experimental results show the effectiveness of the method for damage detection in a more complex structure.

A third model demonstrates damage detection of a large-scale earthquake moment connection that is cyclically loaded to failure. It shows the ability of the algorithm to capture increasing degrees of damage severity. In this case, the subassembly is instrumented with a network of strain gauges, which points to the widespread applicability of the proposed method to various response types.

Chapter 1 Introduction

1.1 Overview

Structural health monitoring (SHM) plays an integral role in maintaining the integrity of important civil, mechanical, and aerospace engineering systems. Structures experience a number of dynamic influences on a daily basis ranging from typical ambient vibrations to more extreme wind and earthquake loadings. Whether the damaging effects of these load cases are visible immediately or appear more gradually in time, it is important to be able to detect the damage before it propagates and becomes detrimental to the entire structure and its surroundings. With renewed interest in the deteriorating state of the nation's infrastructure, the need for effective, efficient, and affordable damage detection methods is becoming more and more apparent. In its *2009 Report Card for American Infrastructure*, the American Society of Civil Engineers reported that "more than 26%, or one in four, of the nation's bridges are either structurally deficient or functionally obsolete," and estimated a need for a $2.2 trillion dollar investment to bring the nation's infrastructure up to an acceptable conditions (ASCE 2010). Maintenance of these structures is crucial for preventing catastrophic failures and ensuring public safety. Local damage detection can help reduce the cost of these repairs by identifying the exact parts of structures that need to be repaired, instead of conservatively retrofitting an entire structure. Additionally, continuous or semi-continuous monitoring of these structures over time will help ensure that they do not fall to serious states of disrepair in the future, which will save on the cost of maintenance in the long term.

Some of the traditional non-destructive evaluation (NDE) techniques include but are not limited to visual inspection, liquid penetrant, magnetic particle, radiography, eddy currents, ultrasonic waves, acoustic emission, and infrared thermography (Trimm 2007). While these methods can be useful in certain circumstances, they require *a priori* knowledge of the location of damage. Also, in order to implement these techniques one must have direct access to the location of damage, which may be difficult to reach, especially after an event such as an earthquake. Furthermore, NDE techniques are costly, difficult to use with complex equipment, and provide only a temporary means of SHM.

Advancements in wireless sensing technology have allowed for the development of new SHM methods that can be applied on a temporary or semi-permanent basis for continual monitoring of structures (Straser and Kiremijian 1998; Lynch and Loh 2006; Farrar *et al.* 2005; Crossbow Technology Inc. 2007; Intel Corporation 2005). These sensor networks are especially applicable for the implementation of vibration based SHM methods, which rely on changes in modal properties—natural frequencies, mode shapes, and modal damping—to reveal changes in the physical properties of the structure—mass, stiffness, and damping, i.e. structural damage (Doebling *et al.* 1998; Alvandi and Cremona 2006).

While this concept may be intuitive, its application is not without obstacles. A major issue is the shear amount of data involved with vibration-based damage identification. Time domain histories can include thousands or more data points, which must be condensed to a manageable amount of data in order for it to be useful. In choosing which data to use, it is important for a method to be able to identify and select the most significant information. Additionally, many methods require *a priori* knowledge

of damage locations, which can limit the application of the method to certain locations in a structure. Finally, the effect of ambient influences on the vibration data can contribute to estimation errors, larger than the influence of the actual structural damage. (Doebling *et al.* 1998)

Furthermore, modal properties only reflect global state of the structure, requiring a great amount of damage before detection is feasible. Current SHM practices involving global-based damage detection also require knowledge of specific structural properties, including mass, stiffness, or damping ratio, for which it is often difficult to determine correct values (Koh *et al.* 1995; Morassi and Rovere 1997; Sohn and Law 1997; and Ratcliffe 1997). Additionally, global detection techniques, which are based on global properties of the structure, are not sensitive to local damage and, therefore, cannot identify damage or determine its locations damage (Farrar *et al.* 1994; Chang *et al.* 2003). Other proposed local damage detection methods, for example the damage locating vector (DLV) method (Bernal 2002), also require the knowledge of structural properties, or require homogeneity of the structural properties as in the two-dimensional gapped smoothing method (Yoon *et al.* 2005).

This study explores an effective damage detection method that uses vibration responses collected via densely clustered sensors to achieve localized damage detection without the need for exact knowledge of structural properties. Influence coefficients, obtained from linear regression between every two node responses, are used as the index for determining the existence of damage. The change point of time-variant influence coefficients can also be determined using a Bayesian statistical framework (Pakzad 2008).

The effectiveness of the proposed local damage detection method is demonstrated and verified through a variety of applications including simulated and experimental results as well as a number of small-scale and full-scale structures.

1.2 Research Objectives

The purposes of this research are to develop an effective local damage detection algorithm considering both ease of implementation and cost-effectiveness, as well as to verify the proposed method for application in SHM of real world structures. The following objectives are established:

1. To develop a damage detection algorithm that utilizes the linear behavior of a structure via linear regression.
2. To create a statistical framework by which to monitor damage indicating parameters to determine when a statistically significant amount of damage has been incurred.
3. To compare simulated and experimental results of a beam-column connection and a two-bay frame for validation of the proposed method.
4. To validate the damage localization method for use with sensor networks comprised of tethered and wireless piezoelectric accelerometers as well as strain gauges.
5. To instrument a full-scale moment connection during failure testing to verify the proposed method for full-scale application and to determine the point of earliest detection.

1.3 Scope of Research

In order to accomplish these research objectives, the following work was completed. A damage detection algorithm was developed based on linear regression and Bayesian statistics. A small-scale beam-column connection, representing a local joint, was constructed in the laboratory and instrumented with two densely clustered sensor networks, one comprised of wired accelerometers and one of wireless accelerometers. Additionally, an experimental two-bay moment frame was developed and instrumented with a dense network of wired accelerometers, in addition to a network of linear variable displacement transducers (LVDTs). Both sets of experimental models were compared with simulated finite element models for performance verification. Finally, a full-scale beam-column moment connection was instrumented with a network of strain gauges and the damage detection algorithm was applied to better understand the effectiveness of the method.

1.4 Organization of Thesis

This thesis consists of six chapters as follows.

Chapter 1 introduces the study providing a general overview, research objectives, and organization of the thesis.

Chapter 2 presents background information related to SHM methods and more specifically local damage detection methods. The proposed localized damage detection method and the statistical framework are developed.

Chapter 3 presents the application of the proposed method to both simulated and experimental models of a local beam-column joint. The experimental model is instrumented with both wired and wireless accelerometers for a side-by-side comparison of both networks.

Chapter 4 discusses the development and application of a two-bay plane frame in both simulated and prototype form. The application demonstrates the proposed method with respect to a more complex structure with a variety of damage scenarios.

Chapter 5 presents the implementation of the proposed method for a large-scale earthquake moment connection as it is cyclically loaded to failure. The performance of the method is assessed within the scope of progressive unknown damage.

Chapter 6 presents a summary of the thesis work, conclusions, and possible future work.

Chapter 2 Development of the Localized Damage Detection Algorithm and Statistical Framework

2.1 Introduction

This chapter pertains to the development of the damage detection algorithm and the statistical framework. Damage identification methods can achieve various levels of identification from merely determining the existence of damage, to identifying the location of said damage, to quantifying the extent of said damage, to the ultimate goal of predicting the remaining service life of the structure, levels 1 through 4 respectively (Doebling *et al.* 1998). The proposed method, which was originally introduced in Pakzad 2008, is classified as level 2, with potential to reach level 3.

This algorithm bases its damage detecting capabilities on the premise that a structure's response changes when physical properties change, i.e., due to damage. The response of the structure is monitored at various locations via a spatially dense sensor network, and linear regression influence coefficients are extracted. When damage is incurred the linear relationship changes, which is reflected in the influence coefficients indicating the existence of damage. In addition to identifying that damage has occurred, considering the locations of sensors associated with changing coefficients allows for localization of the damage as well. Furthermore, a statistical framework that utilizes hypothesis testing can be implemented to determine damage exists at a significant confidence level.

2.2 Structural Theory

Damage detection methods can be classified in a number of ways. One common classification is as linear or nonlinear damage. The definition of linear damage is "the case when the initially linear-elastic structure remains linear-elastic after damage" (Doebling *et al.* 1998). One advantage of having a linear damage state is that the linear equations of motion still apply. Additionally, a linear damage method can utilize finite element models to predict the structure's response to certain damage states. The proposed method relies on this assumption of linearity. The following sections show why this assumption is reasonable for the structures to which the proposed method will be applied.

2.2.1.1 Linear Behavior of System

In order to demonstrate the linear-elastic assumptions of this method, a rigid beam-column joint is considered, as shown Figure 2.1. The general free body diagram has 9 unknowns (x_i, y_i, r_i, x_j, y_j, r_j, x_k, y_k, and r_k) considering the joint to be restrained out-of-plane. The displacement at any point along the structure, u_n, can then be defined as a function of each of these unknowns as follows:

$$u_n = f(x_i, y_i, r_i, x_j, y_j, r_j, x_k, y_k, r_k). \tag{2.1}$$

This number of degrees of freedom (DOFs) can be reduced with the practical assumption of inextensibility of the beam and column members, leaving a structure with 6 independent DOFs (x_i, r_i, x_j, r_j, y_k, and r_k). A structure that is being monitored will experience excitations of the ambient type for a majority of its useful life. Other more extreme excitations should be considered as occurring during the damaging event, in

which case the linearity assumption does not hold true. Because this method involves the comparison of the structural state pre- and post-event, as opposed to during the damaging event, it is reasonable to consider only ambient responses of the structure. Ambient excitations are generally considered as falling within the linear-elastic range, in which small angle theory applies. Small angles correspond to negligible rotations further reducing the number of DOFs by a count of 3 to x_i, x_j, and y_k. With 3 unknowns, 3 relationships are required to define any displacement. If four displacements are defined in terms of the boundary conditions, the relationships can be combined and the unknown boundary conditions factored out such that any one of the displacements can be defined by three other measured displacements:

$$u_4(m) = f\big(u_1(m),\, u_2(m),\, u_3(m)\big) = \sum_{n=1}^{3} \Gamma_n \cdot u_n(m) \tag{2.2}$$

Γ_n are the influence coefficients relating each of the four displacements throughout the structure.

2.2.1.2 Assumption of Negligible Mass Effect

Another important assumption for the application of this method is that the mass of the structure is negligible. This assumption allows dynamic effects to be neglected such that the structure can be considered in its linear static state. Pakzad 2008 and Chang 2010 have presented numerous simulated examples that support neglecting mass. Both found that because the stiffness of a structure is much larger in comparison to the mass when considering a local portion of the structure, the contribution of the mass term becomes negligible and the dynamic equation of motion can be reduced to a static relationship. However, it is important to note that this assumption only applies to a local joint where

nodes are close to each other. Therefore, only nodes that are within the same local joint and share a relatively stiff portion of the structure should be regressed. This may translate to small clusters of dense sensor networks within a larger-scale instrumentation network.

If the structure can be considered as a linear static system, all three displacements can be defined in terms of one, as shown in Figure 2.2. With only one unknown displacement, only one equation is needed to solve for the unknown. This in turn translates to a requirement of only one other measured displacement to define the displacement at any point along the structure, u_n, reducing the influence functions to a single influence coefficient, α_{ij}. The linear relationship between any two locations along the structure, nodes *i* and *j*, is defined by

$$u_j(t_k) = \beta_{ij} + \alpha_{ij} \cdot u_i(t_k) + \varepsilon_{ij}(t_k) \tag{2.3}$$

where,

$u_i(t_k)$, $u_j(t_k)$ = structure's response at nodes *i* and *j*, respectively,

β_{ij} = intercept value of regression line between nodes *i* and *j*,

α_{ij} = influence coefficient of regression line between nodes *i* and *j*,

and ε_{ij} = error of the regression model.

2.3 Influence coefficients as damage indicators

The algorithm employed in this thesis, which is outlined in Figure **2.2**, takes vibration responses of the structure, in the form of acceleration data in this particular case, and uses the assumed linear relationship between different nodes, or sensor locations, with one another. This pair-wise relationship between node responses is defined by utilizing regression analysis. By calculating influence coefficients, α_{ij}, between two nodes *i* and *j*,

based on vibration-induced acceleration response data, one can determine the correlation between these responses according to equation (2.3).

The comparison of the resulting influence coefficients from the initial undamaged state with that of the damaged state of the structure serves as a "*damage indicator*" when it yields a significant change in the value of the coefficients from state to state. More specifically, the influence coefficients exhibit a much more significant change when nodes i and j are located on opposing sides of the damaged segment versus when they are on the same side. As shown in Figure 2.4, when damage occurs in the beam, between nodes i and j, the beam becomes more flexible increasing u_i disproportionately to u_j. From linear regression, this translates to a smaller value of α_{ij} than that of the original undamaged case. This characteristic allows for the identification of the damage location by inspection of the pattern in which influence coefficients exhibit significant changes.

2.3.1 Data Pre-Processing

It is important to note that before the influence coefficients are estimated, the data may require pre-processing. The main forms of pre-processing used are filtering of the data and linearly detrending the data. The filtering step serves to filter out high frequency noise, such as those from unwanted environmental vibrations, so as to allow for the data to focus on the lower frequency content of the signals that correspond to the direct response of the structure to excitation. Similarly, data may exhibit a trend, a systematic increase or decrease over time, due to sensor drift. The data can be detrended by subtracting the mean from the entire dataset to set the mean at zero. This can also be resolved by including an intercept term, β_{ij}, when fitting the regression model.

2.3.2 Influence Coefficient Accuracy and Normalized Estimation Error

Once the data is pre-processed and the coefficients are estimated, the accuracy of the data must be assessed and verified before damage detection can be performed. This is done through consideration of both the accuracy of the pair-wise coefficients and the estimation error. The product of influence coefficients α_{ij} and α_{ji}, yields the evaluation accuracy, EA_{ij}, of these coefficients, indicating which node responses are linearly related to one another with the least amount of error, ε_{ij}, and thus are more accurate predictors. An evaluation accuracy of 1.0 signifies a strong accuracy of estimation, while a product of less than 1.0 corresponds to progressively higher values of noise and nonlinear behavior of the physical structure.

The second parameter that is used for data verification is normalized estimation error, which is calculated by

$$\gamma_{ij} = \frac{\sigma_{\alpha_{ij}}}{\alpha_{ij}} \tag{2.4}$$

where,

α_{ij} = influence coefficient between nodes *i* and *j*

and $\sigma_{\alpha_{ij}}$ = standard deviation of the influence coefficient estimates, α_{ij}.

Normalized estimation error allows for a direct comparison of the amount of error associated with the estimation of each influence coefficient as a damage indicator. This parameter is used to determine which influence coefficients should be used for damage detection. A low estimation error, resulting from a low standard deviation of the estimated influence coefficient, will correspond to a more accurate predictor. Once the

accuracy and error have been assessed for each coefficient, post-processing of the best influence coefficients can be performed for damage identification and localization.

2.3.3 Post-Processing Using Significant Damage Indicators

Once the influence coefficients have been assessed for accuracy and error, the most reliable of these are chosen for use in damage detection. As was previously discussed, changes in the physical properties of the structure, such as loss of material stiffness or section size due to damage, are reflected in changes in the modal properties of the structure. These changes can also be seen directly in the influence coefficients; the linear relationship between certain locations of the structure will change to differing degrees depending on the location of the damage. A high change in the coefficient indicates that the structural response is different in one or both of the locations, *i* and *j*, from that of the original healthy state. The degree to which certain coefficients change can indicate the location of the damage.

2.4 Statistical Framework

In order to determine what defines a "significant change" in the influence coefficients, a statistical framework is applied. A Bayesian statistic is used to determine the change point, the point at which the data indicates damage, at a 95% confidence level (Chen and Gupta 2000). This statistical inference method tests the hypothesis that the mean of the influence coefficients for each successive test is equal to the mean of the influence coefficients from the initial undamaged state,

$$H_0: \alpha_1 = \alpha_2 = \cdots = \alpha_N = \bar{\alpha}, \tag{2.5}$$

against the one-sided alternative hypothesis that the values of the influence coefficients beyond the change point, denoted as *r*, are greater than that of those prior to this point by a significant amount,

$$H_A: \alpha = \alpha_1 = \alpha_2 = \cdots = \alpha_r < \alpha_{r+1} = \cdots = \alpha_N \,. \tag{2.6}$$

The change point *r*, mean μ, and standard deviation σ are all unknown. N represents the number of tests. Because the standard deviation is unknown, it is estimated as the standard error, $\hat{\sigma}$. The statistic that is used to test the aforementioned hypothesis is

$$t = \frac{S_N}{\hat{\sigma}\sqrt{\frac{N(N-1)(2N-1)}{6}}} \tag{2.7}$$

where S_N is the Bayesian statistic

$$S_N = \sum_{i=1}^{N-1} i(\alpha_{i+1} - \bar{\alpha}). \tag{2.8}$$

The test statistic, t, has a t-distribution with N-2 degrees of freedom (Sen and Srivastava 1975). The hypotheses are tested at a 95% confidence level. The physical significance of this hypothesis testing is such that the alternative hypothesis, H_A, indicates that the structure has incurred damage, while the null hypothesis, H_0, means that there is not adequate evidence to establish that damage exists. These hypotheses are tested for those node pairs that have been identified as significant damage indicators in the assessment and verification stage of the method.

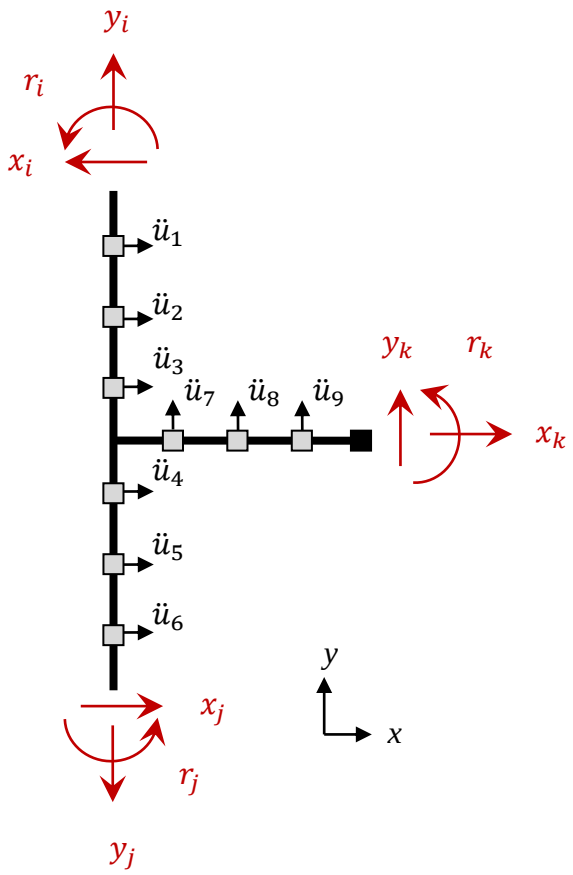

□ : location of sensor node

Figure 2.1. Free body diagram of a rigid beam-column joint

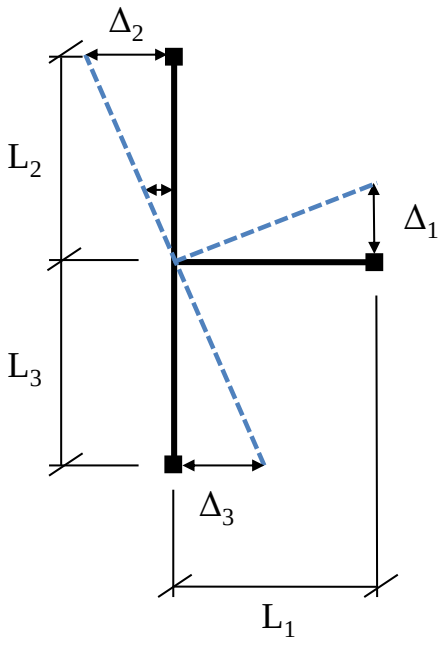

If $L_1 = L_2 = L_3 = L$,
then $\Delta_1 = \Delta_2 = \Delta_3 = \Delta$

Figure 2.2. Behavior of a linear static system

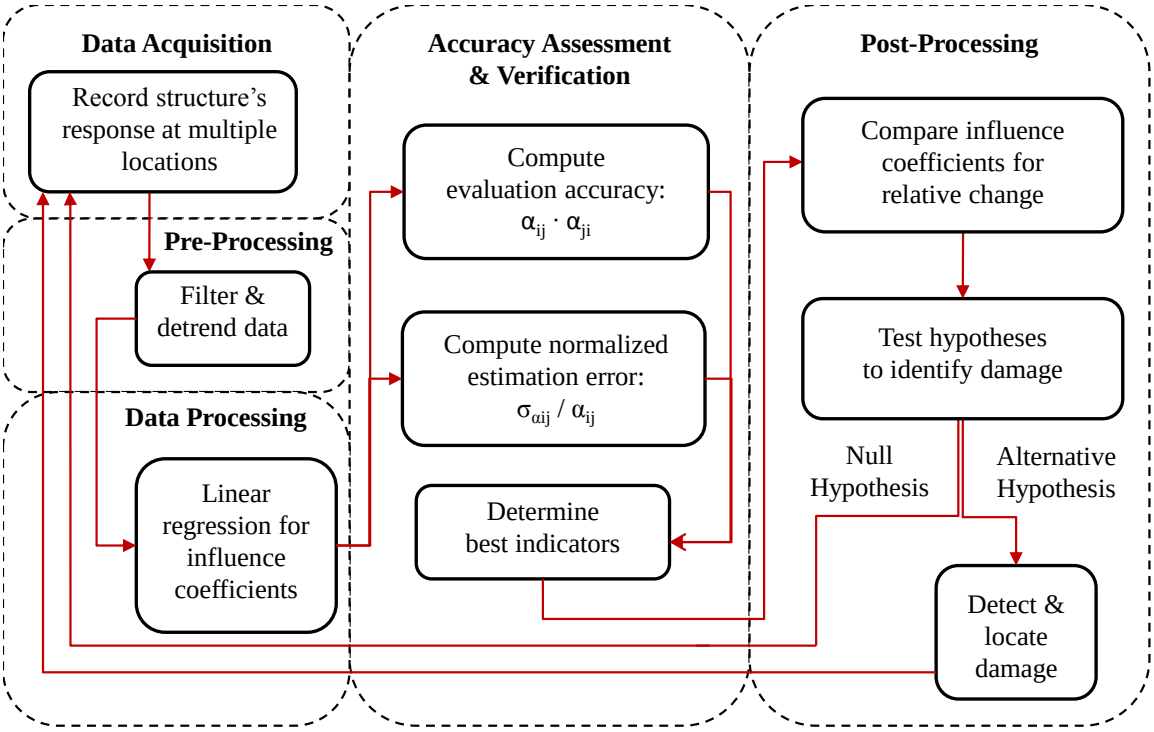

Figure 2.3: Methodology for damage detection

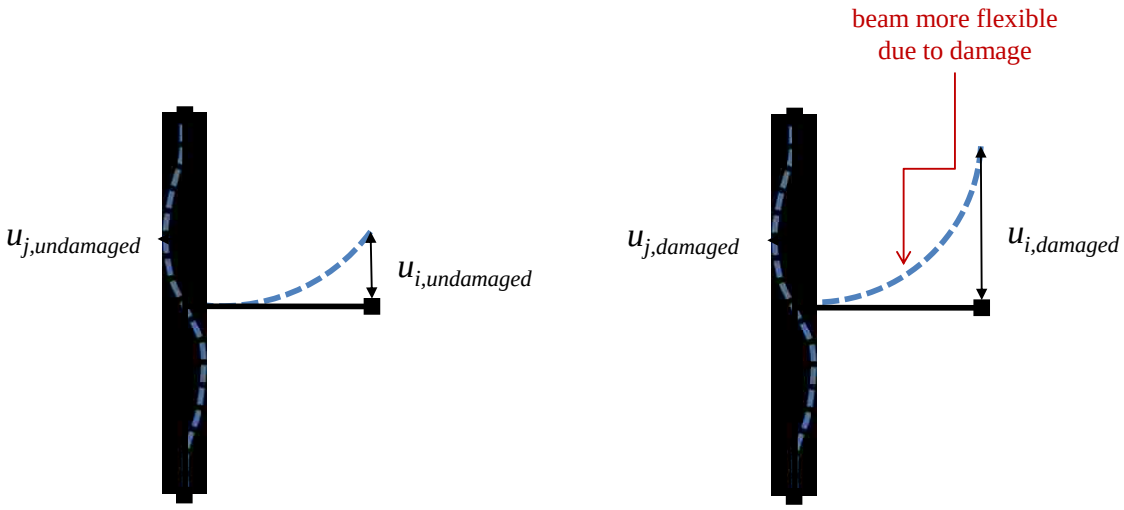

$$u_j(t_k) = \beta_{ij} + \alpha_{ij} \cdot u_i(t_k) + \varepsilon_{ij}(t_k)$$

$$\alpha_{ij,undamaged} > \alpha_{ij,damaged}$$

Figure 2.4. Damage in structure changes relationship between nodes *i* and *j*

Chapter 3 Application to Beam-Column Connection

3.1 Introduction

This chapter presents the application of the local damage detection algorithm, which was developed in Chapter 2, to both simulated and experimental data. For the purpose of this initial application, a small-scale beam-column connection was chosen. The purpose of this model is to represent the portion of a connection closest to the joint, with the beam and column member representing only a small portion of the actual beam and column. Additionally, the damage is idealized as a uniform reduction in cross-sectional area along the entire portion of the beam. Using a case of known damage severity and location serves to verify that the damage detection method performs as expected. Furthermore, this application is useful for identifying trends in the results of the method that can be used for localizing damage in unknown cases, which more closely resemble real-world scenarios.

The experimental specimen is instrumented with both a wired and a wireless sensor network to collect acceleration responses. By collecting from both networks at the same time during testing, a direct comparison of the performance of the newer WSN to that of the traditional wired network is achieved.

3.2 Simulated Model

The proposed localized damage detection algorithm was first validated using a simulated model of a beam-column connection. The simulation was created using SAP2000 software (Computer and Structures, Inc. 2009). The beam-column represents a localized

portion of a larger structure, for example a single joint in a larger building frame as demonstrated in Figure 3.1. A local joint is a location in a structure that is prone to damage due to high stress concentrations at the connections. The ability to determine not only the joint, but the location within the joint where damage has occurred can lead to more efficient and cost-effective repair solutions in a structure. The simulation was designed not only to confirm the applicability of this method for a beam-column, but also to verify the experimental prototype that was later implemented.

3.2.1 Properties of the Simulated Model

The computer model consists of 13 nodes and 12 elastic beam finite elements. Each element node has three degrees of freedom, u_x, u_y, and θ_z, which allows for translational and bending behavior. The structure is considered a "plane" structure, which disallows out-of-plane and torsional degrees of freedom. The elements are arranged to comprise two legs of a column and a beam member, all of equal length, as shown in Figure 3.2.

Each element has a uniform, hollow, square cross-section with 0.125 in wall thickness, 0.4375 in^2 area, and a moment of inertia of 0.057 in^4. The steel is assigned an elastic modulus of 29,000 ksi. Damage was simulated by reducing the beam stiffness uniformly along the member by 40%. The damaged properties of the beam include a wall thickness of 0.0625 in, a cross-sectional area of 0.2344 in^2, and a moment of inertia of 0.0345 in^4. The geometric properties for both the undamaged and damaged cases are summarized in Table 3.1. The mass of this small portion of the connection is assumed negligible, as per the assumption stated in Section 2.2.1.2. The boundary conditions of

the column are fixed on either end, while the beam cantilevers from the centerline of the column.

3.2.2 Simulation Procedure

For both the undamaged and damaged cases, a white noise excitation was simulated at the free end of the beam. The resulting displacement responses were generated at each of the nine nodes labeled u_1 through u_9 to represent sensor node locations along the beam and column members. Measurement noise was also accounted for by adding a Gaussian noise with a standard deviation equal to 5% of the root mean square of each response signal.

3.2.3 Results of Simulated Model

The damage detection algorithm was then applied to the simulated data and the parameters were extracted. The relative change in the influence coefficients between the undamaged and damaged states is shown for each pair-wise node relationship in Table 3.2. The influence coefficients α_{ij}, $1 \leq i,j \leq 6$ all experience very small (less than 1%) changes between the undamaged and damaged states. This implies that the physical properties between these nodes have not changed. However, the coefficients of nodes 1 through 6 paired with nodes 7, 8, and 9 show relative changes of between 30-40%. When nodes are on opposite sides of the damage, i.e. nodes 1 through 6 are located on the undamaged column, while nodes 7, 8 and 9 are located on the damaged beam, the physical properties between the paired nodes changes. This physical change is reflected in a more significant relative change in the value of influence coefficients. Furthermore,

the influence coefficients α_{ij}, $7 \leq i,j \leq 9$ also experience a noticeable change in coefficients (about 3-10%). This signifies that the physical properties of the structure between the nodes associated with α_{78}, α_{79}, and α_{89} have changed. Therefore, damage must exist between these nodes. This is consistent with the simulated damage: a 40% stiffness reduction of the beam.

3.3 Experimental Model

The algorithm was further verified through laboratory experiments on a specimen similar to that of the simulated model. These experiments were conducted at the Center for Advanced Technology for Large Structural Systems (ATLSS) at Lehigh University. Again, the prototype represents a portion of the beam and column members as they come to a local joint. The structure was instrumented with two sensor networks; one of 9 wired accelerometers and another of 9 wireless accelerometers. The structure's responses were collected at each node for 50 undamaged tests and 50 damaged tests, and the algorithm was employed. This experiment serves as both a validation of the method on a non-simulated structure as well as a comparison of a wireless sensor network to that of a reliable wired system.

3.3.1 Properties of the Experimental Specimen

The small-scale experimental prototype was constructed using two square steel tube members—6-ft length for the column member and 3-ft length for the beam member—attached with two bolted steel angles to create a T-shaped fixed joint of equal length members. Figure 3.3 shows that the angles are stiffened with two welded triangular plates

to ensure a moment connection. The two ends of the column have fixed supports with angles through-bolted on either side of the member, as shown in Figure 3.4, while the beam cantilevers from the centerline of the column. The column member, which remains constant throughout the entire experiment, is a one-inch square hollow tube with a wall thickness of 0.125 in. The beam portion of the joint consists of two interchangeable members. The first member exhibits the same cross-sectional properties as the column. The second member, which replaces the first to represent structural damage to the joint, is also a one-inch square hollow tube but with a 0.0625-in wall thickness. The geometric properties are the same as those for the simulated models summarized in Table 3.1. A photograph of the overall experimental test setup is shown in Figure 3.5.

3.3.2 Experimental Procedure

The free end of the cantilever was attached to an actuator and excited by harmonic force at a 15 Hz frequency and the acceleration responses were collected at each of the nine sensor nodes. The influence coefficients were then computed using linear regression. This portion of the experiment served to establish a baseline response for the undamaged structure.

For the second portion of the experiment, the beam member was replaced by the member with reduced wall thickness in order to simulate damage to the structure. The excitations were repeated, and the damaged state influence coefficients were computed. The resulting data was then compared between the damaged and undamaged states to verify the detection of damage.

3.3.2.1 Specifications of the Actuator

The actuator used to excite the structure is a MODAL 50A actuator produced by MB Dynamics shown in Figure 3.6 (1990). The actuator has a peak force capability of 25 lbs without a cooling system and can apply up to 50 lbs with cooling. Table 3.3 presents more specifications for the MODAL 50A. The applied excitation type and amplitude was controlled by a combination of the SigLab S2022D1/A signal controller, SigLab software for MATLAB, and the SL500VCF Power Amplifier shown in Figure 3.7 (Spectral Dynamics, Inc. 2001; MB Dynamics 2001). The SL500VCF Power Amplifier has an analog jog for gain, which was set to a given level prior to testing and remained constant throughout. The SigLab controller allows digital control of the force magnitude by varying the input voltage peak. In this experiment, a voltage peak of 0.2 V was used for a 15 Hz sinusoidal force, yielding a peak acceleration of about 0.3 g at node 9 (the location of the largest recorded response).

3.3.2.2 Sensing Systems

The specimen was instrumented with two sensor networks located at 9-inch intervals along the beam and column to collect the structures response to the applied excitation. The merits of the two systems were then compared via both pre-processing of the data and performance with the local damage detection method.

3.3.2.2.1 Wired Capacitive Accelerometers

The first is a network of 9 wired accelerometer sensors. The accelerometers used in this experiment are model number 3701G3FA3G manufactured by PCB Piezotronics, Inc

(2004). The 3701G3FA3G is a capacitive accelerometer, which incorporates an air-damped, opposed-plate capacitor to sense accelerations in terms of a change in capacitance (PCB Piezotronics, Inc 2004). An analog-to-digital converter (ADC) reads the change in capacitance and translates this to a voltage that corresponds to a specific acceleration. This model can detect accelerations within the range of ± 3 g with a broadband resolution of 30 μg RMS (equivalent to 2 μg/√Hz output noise). Other specifications for these sensors are summarized in Table 3.4. Figure 3.8 shows one of these sensors mounted on the test specimen.

3.3.2.2.2 Wireless MEMS Accelerometers

The second network consists of 9 wireless accelerometers. The accelerometers used consist of the Imote2 processor board produced by Intel (2005) combined with the SHM-A sensor board developed by Rice and Spencer in the Smart Structures Technology Laboratory at the University of Illinois at Urbana-Champaign (2008; 2009). One of the wireless sensors is shown mounted on the experimental structure in Figure 3.9. The processor board operates via the TinyOS operating system, a software framework developed by The Illinois Structural Health Monitoring Project (ISHMP) (Spencer and Gul 2009). The TinyOS framework allows the Imote2 to be programmed with features that can improve wireless data collection, such as time synchronization of the sensor network and reliable data transfer. The Remote Sensing application of the ISHMP package provides both of these features, and is used as the primary application for this experiment.

The sensor board incorporates a low-cost, highly-sensitive 3-axis micro-electro-mechanical systems (MEMS) accelerometer, LIS3L02AS4, manufactured by ST Microelectronics (2005). A MEMS accelerometer operates on similar principles as a capacitive sensor only on a micro scale. The accelerometer has a noise density of 50 μg/√Hz and a measurement range of ± 2 g. The sensor board also features a low-pass filter, a gain difference amplifier, and the Quickfilter QF4A512, a programmable 4-channel, 16-bit ADC (Quickfilter Technologies, Inc. 2007). Each of these features contributes to the ability to measure small increments of accelerations, appropriate for sensing ambient vibrations. Table 3.5 presents the specifications for both the Imote2 platform and the MEMS accelerometer.

3.3.2.2.3 Data Acquisition System

Acceleration responses were collected from the wired sensors using the CR9000, a modular, multiprocessor data acquisition (DAQ) system and PC9000 support software by Campbell Scientific, Inc. (2005; 2009). Figure 3.10 shows the DAQ system. The CR9000 has a 16-bit analog-to-digital converter and a peak sampling rate of 100 kHz. For this experiment, the wired data was collected at a 250 Hz sampling rate (0.004 sec sampling interval), with each test lasting 40 seconds.

The wireless data was collected at a sampling rate of 280 Hz (0.0036 sec sampling interval), with each collecting lasting approximately 36 seconds. Data collection using both systems was performed simultaneously for direct comparison.

Both the undamaged and damaged structures were tested 50 times; however, two of the datasets were unusable leaving a total of 96 tests, each containing 20,000 data points

(10,000 wired and 10,000 wireless) per sensor location. These 17.3 million data samples were then processed through the algorithm to detect the occurrence of damage.

3.3.3 Results of Experimental Model using Wired Accelerometers

The experiments were conducted with the undamaged and damaged states experiencing 15 Hz harmonic vibrations. While the application of this algorithm is not limited to a certain frequency, previous experiments involving this test specimen showed that the 15 Hz data exhibited the least amount of actuator noise, and thus was chosen for these experiments (Chang 2010).

The wired capacitive accerlerometers, with their high resolution and reliable wired data transmission, provide a reliable network. Therefore, the wired data was initially used for assessing the performance of the proposed damage detection method. This data was then used as a reference for the performance of the WSN that was simultaneously implemented on the structure.

3.3.3.1 Accuracy Assessment and Verification

Once the 72 influence coefficients have been calculated from the acceleration data, the estimates must be assessed to identify the most significant indicators, which can then be used for damage detection. Evaluation accuracy, *EA*, and normalized estimation error, γ, which are previously defined in Section 2.3.2 are integral for this accuracy assessment. By inspection of these parameters, eight different trends can be identified in the undamaged and damaged parameters, with lower estimation errors coinciding with greater evaluation accuracies and vice versa. These trends have been designated as eight

different regions, whose mean values are presented in Table 3.6. Region 1 in the table corresponds to the least estimation error and highest accuracy, and region 8 corresponds to the greatest estimation error and lowest accuracy. Therefore, parameters in region 1, consisting of $\alpha_{ij},\ 7 \leq i,j \leq 9$, are the most accurate and have the least error. This is a reasonable outcome as the actuator applies a force at the end of the beam, closest to nodes 7, 8, and 9. This proximity results in a larger amplitude of excitation at these nodes compared with that of the column nodes, thus, corresponding to a higher signal-to-noise ratio (SNR) of the data at these nodes. A higher SNR correlates to better quality data.

On the contrary, region 8, which consists of parameter α_{16}, exhibits the poorest accuracy and the greatest estimation error. This can be accounted for by the fact that each of these nodes is located at either end of the column near the fixed ends. These boundary conditions restrict the column from movement closest to the support, greatly reducing the magnitude of the acceleration signal and, thus, the SNRs of these nodes. The low SNR values contribute to the fact that α_{12} or α_{56} exhibit lower accuracy than α_{78} or α_{89} despite the similar configuration of the nodes with respect to one another. Figure 3.11 through Figure 3.12 show an example of α, and its corresponding *EA* and γ results from regions 1, 3, and 8, respectively. Figure 3.11 shows that the *EA* is almost equal to unity and the γ is almost equal to 0 for region 1. The *EA* and γ values for a region 3 pair, shown in Figure 3.12, also exhibit accurate values, although not quite as accurate as region 1. Figure 3.13, however, shows a much lower *EA* and a noticeably higher γ associated with region 8. Based on similar data for all 8 regions, it can be concluded that regions 1 through 3 contain the most useful damage indicators. On average, these influence coefficients exhibit accuracy greater than 98% and estimation error less than .0012.

3.3.3.2 Post-Processing and Damage Detection

The results of the relative changes in the average influence coefficients, α_{ij}, from the undamaged and damaged tests are shown in Table 3.7. Observing these coefficient changes is the first step in post-processing the data. The changes associated with α_{78}, α_{79}, and α_{89}, which are 9%, 13%, and 4% respectively, are indicators of a property change between nodes 7 and 9. This is consistent with the damage, or stiffness reduction, that was simulated along the full length of the beam portion of the test structure.

The coefficients of region 2, α_{23} and α_{45}, experienced 1% and 6% changes. This is less consistent with what would be expected in comparison to the very low (less than 1%) changes that were seen in the simulated results. The likely cause of this is noise, which is typically higher in an experimental setting, but even more so in a real structure.

The influence coefficients from region 3 were in line with the prediction of the simulated results, α_{ij}, $7 \leq i \leq 9$ and $1 \leq j \leq 6$, with noticeable fluctuations (12-39%) from the undamaged state to the damaged state, with the exception of α_{47} which had only a 5% change. These changes, along with the simulated results, show that nodes on opposite sides of the damage location experience the largest changes. This is because as damage occurs, the relationship of two points in the actual physical structure deviates slightly from linear behavior. Figure 3.14 shows the percent changes for select pair-wise coefficients from regions 1, 2, and 3, respectively. This further supports the theory that nodes on opposite sides of damage show the greatest change, while nodes with no damage between them show a significantly smaller change. Pairs with nodes within the damage location show some change, but not as large as that of nodes on opposite sides.

The reason for this is that when both nodes are within the damage, both nodes experience similar increases in flexibility, resulting in a less severe differential. Therefore, inspection of the pattern of changes in pair-wise coefficients points to the location of damage within the structure (i.e. damage between nodes 2 and 7, 3 and 8, and so forth).

While the results for the first three regions were mostly consistent with the expectations set out by the simulated structure, the remaining regions were not as consistent. A prime example is region 6, consisting of parameters α_{24}, α_{25}, α_{34}, and α_{35}. According to the model, these coefficients, whose nodes are all located on the same side of the damage, should experience very little fluctuation from the undamaged to damaged states. However, their experimental changes range from 7-14%. Recall that in the previous verification stage, region 6 showed the third lowest accuracy and the third highest error. Thus, this example shows the importance of using parameters *EA* and γ to identify accurate damage indicators.

3.3.3.3 Hypothesis Testing for Significant Damage

As is evident, the difference between undamaged and damaged coefficients can be indicative of the existence and location of the damage in a structure. However, in an actual structure, one will not necessarily know when damage has occurred, or if in fact damage has occurred at all. Therefore, another element must be added for complete damage detection: the statistical framework, which is presented in Section 2.4.

The hypothesis testing plot graphically shows the change point of damage, the point at which damage is identified at a certain confidence level, by plotting the test statistic against the test run number. A graph in which the data crosses the confidence

bounds, either positive or negative, corresponds to a positive hypothesis, previously defined as H_A in equation (2.6), indicating the detection of damage. If the accuracy and estimation error associated with the nodes being considered are high and low respectively, the prediction of the hypothesis test will be more exact and will cross the confidence bounds closer to the occurrence of damage. In order to demonstrate this behavior, the test statistic from the 50 damaged state tests were plotted against their run number. Because damage exists for all of the plotted data, the most accurate damage indicators will yield a plot in which the confidence bounds are crossed closest to the occurrence of damage. This can be seen in comparing Figure 3.16, Figure 3.17, and Figure 3.18 to Figure 3.19, the hypothesis test results for region 1, 2, and 3 coefficients, accurate indicators, versus that of a region 8 coefficient, a poor indicator. The first three plots show a decisive cross of the 95% confidence bound in fewer than 8 test runs, while the region 8 coefficient never actually crosses the bound. Figure 3.20 shows another region 8 coefficient, the reciprocal of that shown in Figure 3.19, in which the statistic does cross the confidence bound. This discrepancy is likely due to the high error and low accuracy associated with these coefficients. Therefore, this demonstrates the importance of using the *EA* and γ parameters for first determining which coefficients to monitor for effective damage detection.

Additionally, by comparing the first three figures, Figure 3.16, Figure 3.17, and Figure 3.18, among themselves, it can be determined that a coefficient with a larger change between the damaged and undamaged states tends to show damage earlier than a coefficient of comparable accuracy with a smaller change. It was shown previously that the region 1 and region 3 coefficients saw 13% and 22% changes, respectively. These

cross the bound after only 4 and 5 runs, respectively, whereas, the region 2 coefficient, with only a 1% changed, took until the 7^{th} run to confidently show damage. This suggests that when a statistic crosses the bound first, compared to coefficients of similar accuracy, it is most likely more integral to the damage location. Therefore, these plots demonstrate that damage is detected by hypothesis testing, making this method a reliable means of damage detection.

3.3.4 Comparison of WSN to Wired Accelerometers

In order to consider realistic application of the proposed damage detection method, there must be a reliable and affordable sensor network with which to instrument the structure. Continued advancements in wireless sensor technology strive to fulfill that role. These WSN need to be validated in experimental settings in order to be confidently applied in the field. Because the wired sensors used are considered as a reliable network, the wired results were used as a direct comparison point for the WSN that also instrumented the test specimen. Both the wired and WSN datasets were compared for noise and damage detection performance.

During data collection, an attempt was made to collect from both sensor networks simultaneously, although complete synchronization between the two systems was not realistic. By collecting the data at the same time, differences in results due to varied environmental noise between the two datasets are avoided. Therefore, any differences that appear between the two sets can be accounted to network performance and reliability. Figure 3.21 shows a comparison of the data collected at node 9, the node with the largest recorded amplitude, in both the time and frequency domains where the time

histories appear to be consistent. Both histories show the harmonic response due to the harmonic excitation clearly with no visible noise. The amplitudes differ slightly, with the wireless sensors showing a larger value. This difference is explained by a difference in sensor locations, as it was difficult to align the wired and wireless sensors exactly.

Similarly, the frequency content of each sensor type is similar. Both show a dominant peak at the forcing frequency of 15 Hz. The main difference between the two power spectra is that the wireless data contains more noise at high frequencies as well as at very low frequencies.

One anomaly in the power spectra that was observed throughout tests using the MODAL 50 actuator was the existence of recurring peaks at intervals equal to the forcing frequency, which can be seen in the power spectra of Figure 3.21. For example, for the 15 Hz forcing frequency, peaks were observed at 15 Hz, 30 Hz, 45 Hz, 60 Hz and so forth. This shows that the excitation that the actuator produces is not a pure harmonic, but rather a sum of harmonics.

3.3.4.1 Accuracy Assessment and Verification

Assessment of the accuracy of estimating the influence coefficients is another means for comparing the wired and WSN performance. Figure 3.22 shows the α, EA, and γ values for nodal pair 5-8 using the wireless data. This figure, considering a region 3 coefficient, shows that for certain datasets the WSN data experienced large errors and very low accuracy values. This points to unreliable results for these datasets. Identification of this type of unreliable data is the exact purpose of these two accuracy parameters, so the results for these outlier runs were regenerated excluding any datasets that showed erratic

accuracy values. Parallel wired and WSN datasets were removed, despite good wired accuracies, in order to maintain the benefits of the side-by-side data collection and comparison.

Figure 3.23 to 3.25 show the α, *EA*, and γ values estimated without the outlier datasets, for nodal pairs from beam-beam, beam-column, and column-column, respectively. In each case, the *EA* and γ for the wired network are better on a whole than that of the WSN. Even after the high error/low accuracy datasets removal, there are still certain datasets in which a drop in accuracy and an increase in error occur for both networks; however, the accuracy is distinctively more compromised for the WSN. Because these fluctuations in performance occur across both the wired and WSN datasets and the values are within a reasonable range, these datasets were included. It can also be reasonably assumed that there was a spike in environmental noise during these particular collections. This suggests that the accuracy of the wireless sensors, with their higher noise floor, is more greatly affected by environmental noise than the wireless sensors. Overall, the α, *EA* and γ values are comparable for the WSN and wired network, with the wired performing slightly better.

3.3.4.2 Damage Detection

Local damage detection was performed using data from each sensor network as a third comparison point. The influence coefficient plots of Figure 3.23 to Figure 3.25 show the coefficients side by side for the network. Inspection of these plots demonstrates that the WSN coefficient estimates show a smaller change in the line. However, a change is seen, which points to the occurrence of damage. Additionally, the coefficient values estimated

using WSN data are offset from that of the wired data. These differences are accounted to the slight variation in the location of the wired and wireless sensor nodes. If the sensors are not perfectly aligned, then the values would reflect slightly different node locations.

Figure 3.26 also shows the relative change for select nodal pairs of the WSN and wired datasets. The changes at α_{28}, α_{58}, and α_{25} of the WSN are comparable to the changes expected from the wired results. The change at α_{89} is a little larger than that of the wired, but still on par with other nodal pairs of its type (beam-beam within damage). On the other hand, a notable inconsistency is seen in two of the column-column nodal pairs, α_{12} and α_{56}. The WSN shows significantly larger changes, almost 10 times larger than those seen in the wired results. This drastic variation can be explained by the *EA* and γ values shown in Figure 3.27. These two coefficients have lower accuracies (less than 0.9) associated with them compared to the other four WSN values and the wired values. Lower accuracy correlates to lower reliability. Consequently, these coefficients would not be considered as trusted damage indicators.

Based on the three presented comparison points it can be seen that the WSN, while not as effective as the wired network, is useful in localizing the onset of damage.

3.3.4.3 Hypothesis Testing

The fourth and final comparison for the WSN and wired network performance was the statistical framework for damage detection. Again, the same three coefficients, α_{79}, α_{58}, and α_{52} were chosen as the comparison points for this test to consider the three types of nodal relationships. Figure 3.28 to Figure 3.30 show the test statistic for each pair with the WSN and wired plotted side by side. In the first two plots, both the wired and WSN

test statistics cross the 95% confidence bound. In both cases, the WSN statistic crossed after the wired; a difference of about 10 test runs was seen for α_{79}, while it took only about one or two more tests to detect damage in α_{58}. This variation in detection is justified by the difference in percent changes experienced by each of these coefficients. The relative change for α_{79} was only about 6.5% for the WSN (13.1% for the wired), compared to α_{58}'s change of 23.8% for the WSN (22.7% for the wired). A larger changed corresponds to more decisive damage detection.

In Figure 3.30 it can be seen that the WSN statistic for α_{52}, due to higher disturbance of noise in data, does not present qualified results for identifying the damage with 95% confidence level after 33 damaged datasets. The wired test statistic for this same coefficient indicates significant damage after approximately 5 damaged tests. However, it should be noted that this node pair is a region 6 parameter, corresponding to the third lowest average accuracy and the third highest average error. Therefore, this parameter is not considered to be a reliable damage indicator, and other more reliable parameters, such as α_{79} and α_{58}, would instead be monitored in practical application of this method.

Table 3.1. Properties of beam-column elements for undamaged and damaged states

	Column	Beam (Undamaged)	Beam (Damaged)
Total Length [ft]	6	3	3
Wall Thickness [in]	0.125	0.125	0.0625
Cross-Sectional Area [in^2]	0.4375	0.4375	0.2344
Moment of Inertia [in^4]	0.057	0.057	0.0345

Table 3.2: Relative change in influence coefficients, α_{ij}, from undamaged to damaged states for simulated structure

	1	2	3	4	5	6	7	8	9
1		0.08%	0.08%	0.08%	0.08%	0.08%	31.2%	40.8%	45.2%
2	0.08%		0.08%	0.08%	0.07%	0.09%	31.2%	40.8%	45.1%
3	0.08%	0.08%		0.07%	0.08%	0.08%	31.2%	40.8%	45.2%
4	0.08%	0.08%	0.08%		0.08%	0.08%	31.2%	40.7%	45.1%
5	0.08%	0.07%	0.08%	0.08%		0.07%	31.2%	40.8%	45.1%
6	0.08%	0.09%	0.07%	0.08%	0.07%		31.2%	40.8%	45.1%
7	23.8%	23.8%	23.8%	23.8%	23.8%	23.8%		7.29%	10.6%
8	29.0%	29.0%	29.0%	29.0%	29.0%	29.0%	6.79%		3.11%
9	31.1%	31.1%	31.1%	31.1%	31.1%	31.1%	9.60%	3.01%	

Table 3.3. Specifications of MODAL 50A actuator

Stroke	1" peak-peak (continuous), 1.1" between stops
Force Output	25 lbs (without cooling), 50 lbs (with cooling)
Stinger attachments	Chuck and assortment of collets handles wire sizes from 0.020" to 0.125"
Actuator attachments	Floor: adjustable trunnion base and screw feet
Weight	Shaker with trunnion base: 55 lbs
Dimensions	11.5" (height) x 7.5" x 9.25" (footprint)

Table 3.4. Specifications of PCB 3701G3FA3G accelerometers

Measurement Range	± 3 g
Voltage Sensitivity	1000 mV/g
Transverse Sensitivity	≤ 3%
Resonant Frequency	≥ 400 Hz
Temperature Range	-40 to +185 °F

Table 3.5. Specifications of Imote2 and LIS3L02AS4 on SHM-A sensor board

Imote2		LIS3L02AS4	
Processor	Intel PXA271	Acceleration	±2 g
SRAM Memory	256 kB	Avg. Noise Floor (X&Y)	0.3 mg
Memory	32 MB (SDRAM/FLASH)	Avg. Noise Floor (Z)	0.7 mg
Power Consumption	44 mW at 13 MHz 570 mW at 416 MHz	Resolution	0.66 v/g
		Temperature Range	-40 to 85ºC
Radio Frequency Band	2400.0 – 2483.5 MHz		
Dimensions	36 mm×48 mm×9 mm		

Table 3.6: Trend regions according to average estimation error (γ) and evaluation accuracy (EA)

Region	Influence Coefficients	γ_{ij} Average	EA_{ij} Average
1	α_{78}, α_{79}, and α_{89}	0.0001	1.000
2	α_{23} and α_{45}	0.0005	0.998
3	α_{27}, α_{28}, α_{29}, α_{37}, α_{38}, α_{39}, α_{47}, α_{48}, α_{49}, α_{57}, α_{58}, and α_{59}	0.0012	0.985
4	α_{12}, α_{13}, α_{46}, and α_{56}	0.0015	0.975
5	α_{17}, α_{18}, α_{19}, α_{67}, α_{68}, and α_{69}	0.0018	0.967
6	α_{24}, α_{25}, α_{34}, and α_{35}	0.0022	0.947
7	α_{14}, α_{15}, α_{26}, and α_{36}	0.0025	0.937
8	α_{16}	0.0161	0.889

Table 3.7. Relative change in influence coefficients, α_{ij}, for experimental structure

	1	2	3	4	5	6	7	8	9
1		4.17%	5.55%	9.58%	3.40%	4.05%	17.1%	27.5%	31.7%
2	3.12%		1.26%	13.3%	6.68%	6.65%	21.6%	32.8%	37.4%
3	4.11%	1.16%		14.0%	7.52%	7.72%	22.9%	34.2%	38.9%
4	12.1%	14.9%	16.5%		6.31%	6.83%	5.27%	14.9%	18.8%
5	5.72%	8.48%	10.0%	6.58%		0.59%	12.5%	22.9%	27.0%
6	7.78%	9.33%	10.6%	5.91%	1.72%		12.0%	21.9%	25.9%
7	15.6%	18.1%	19.2%	6.38%	12.0%	12.1%		9.28%	13.1%
8	22.8%	25.1%	26.1%	14.4%	19.6%	19.6%	8.52%		3.48%
9	25.5%	27.7%	28.6%	17.4%	22.3%	22.5%	11.6%	3.38%	

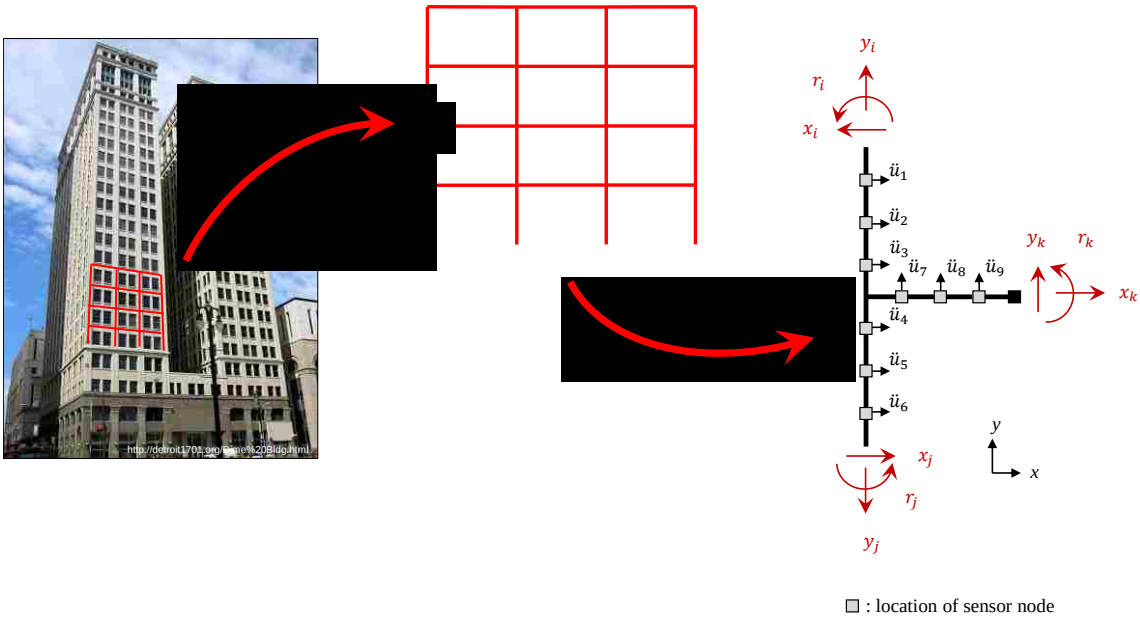

Figure 3.1. Beam-column represents a local joint within a larger structure

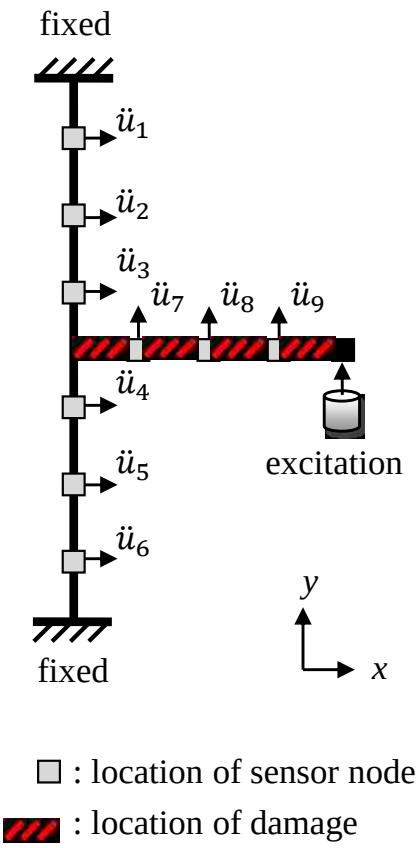

Figure 3.2. Simulated model of beam-column connection with nine node locations

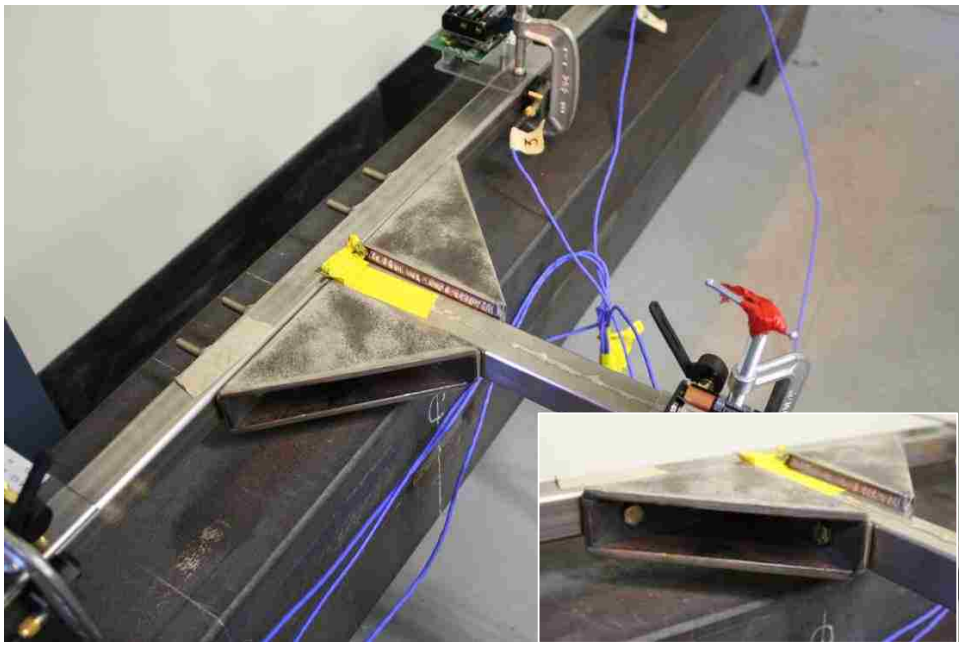

Figure 3.3. Beam and column connected by bolted angles with triangle stiffeners

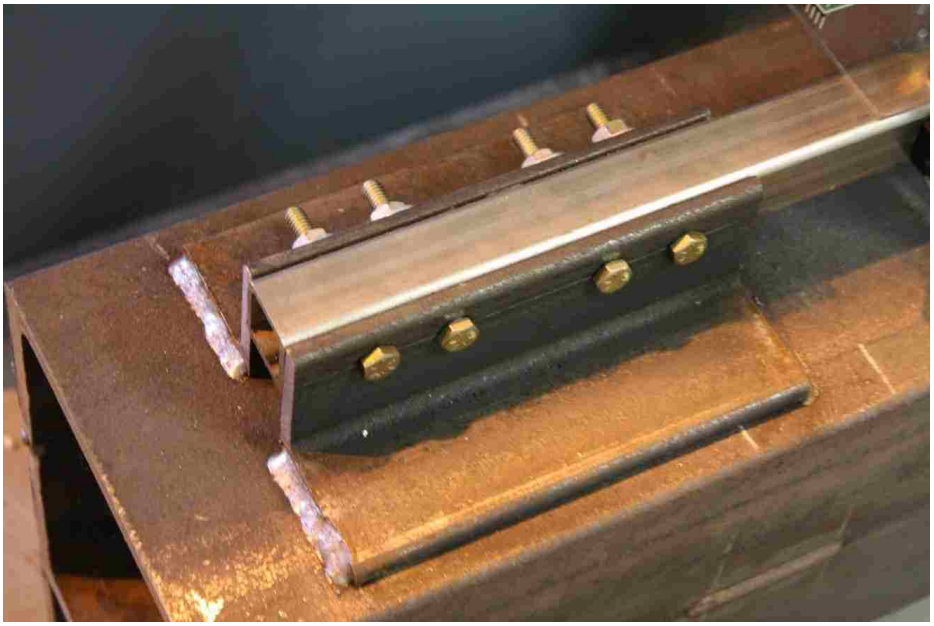

Figure 3.4. Fixed connection of column on either end using two angles and through-bolts

Figure 3.5. Experimental test bed for beam-column prototype instrumented with wired and wireless accelerometers

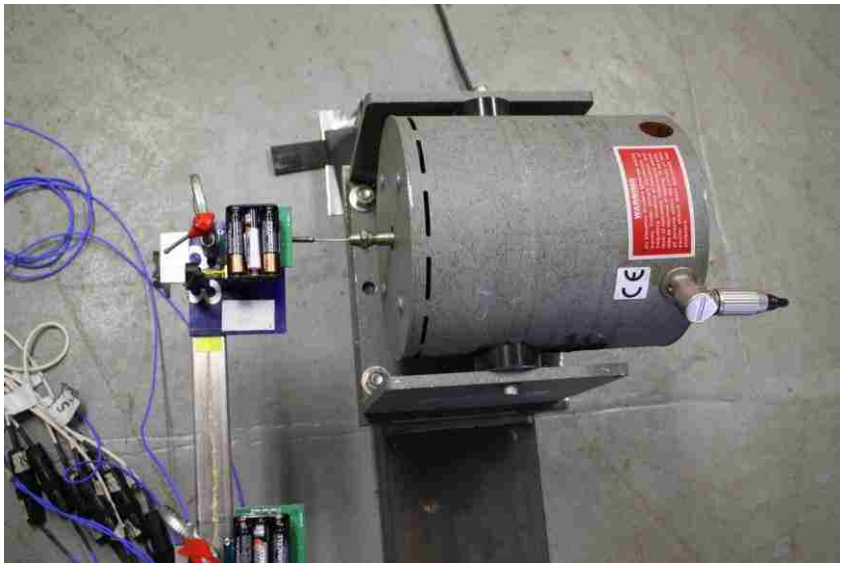

Figure 3.6. MODAL 50A by MB Dynamics actuator attached to free end of beam

Figure 3.7. Signal controller by SigLab and power amplifier by MB Dynamics

Figure 3.8. PCB 3701G3FA3G accelerometer mounted on beam at node 8

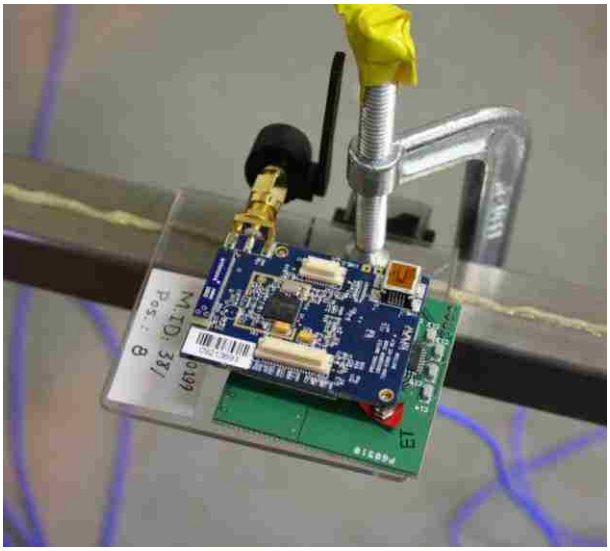

Figure 3.9. Wireless sensor consisting of the SHM-A sensor board attached the an Imote2 processor board, shown mounted on beam at node 8

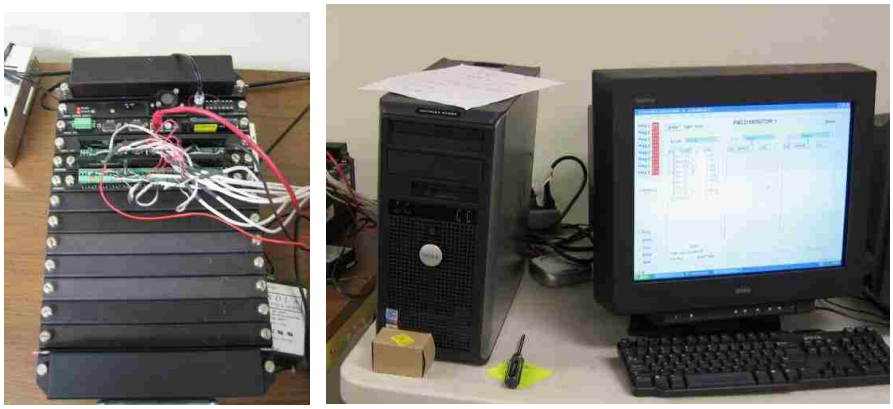

Figure 3.10. CR9000 data acquisition system

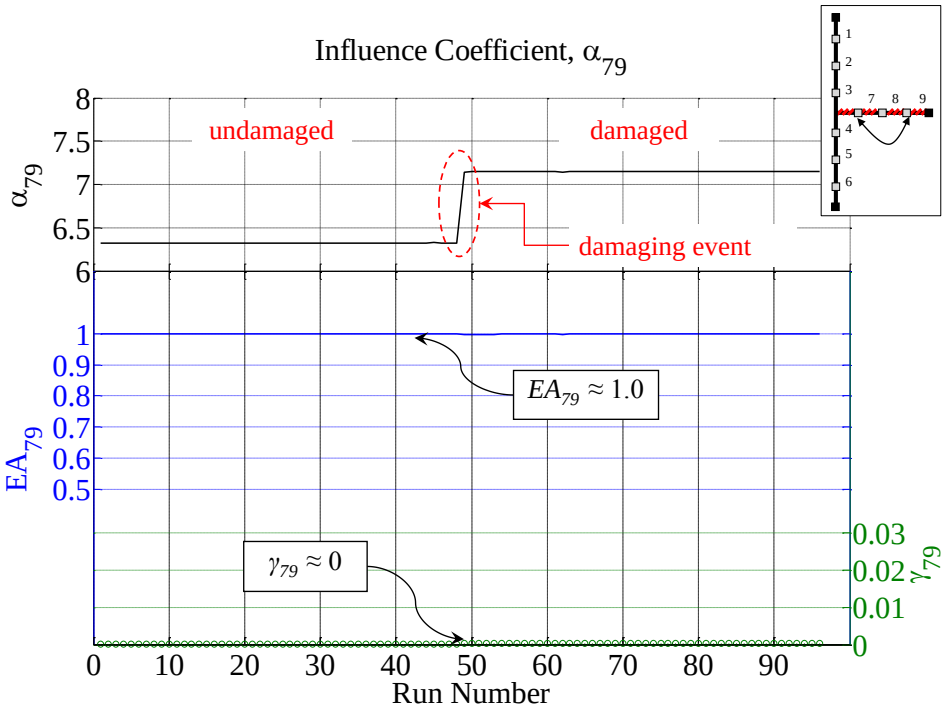

Figure 3.11. *α*, *EA*, and *γ* results for Region 1 pair

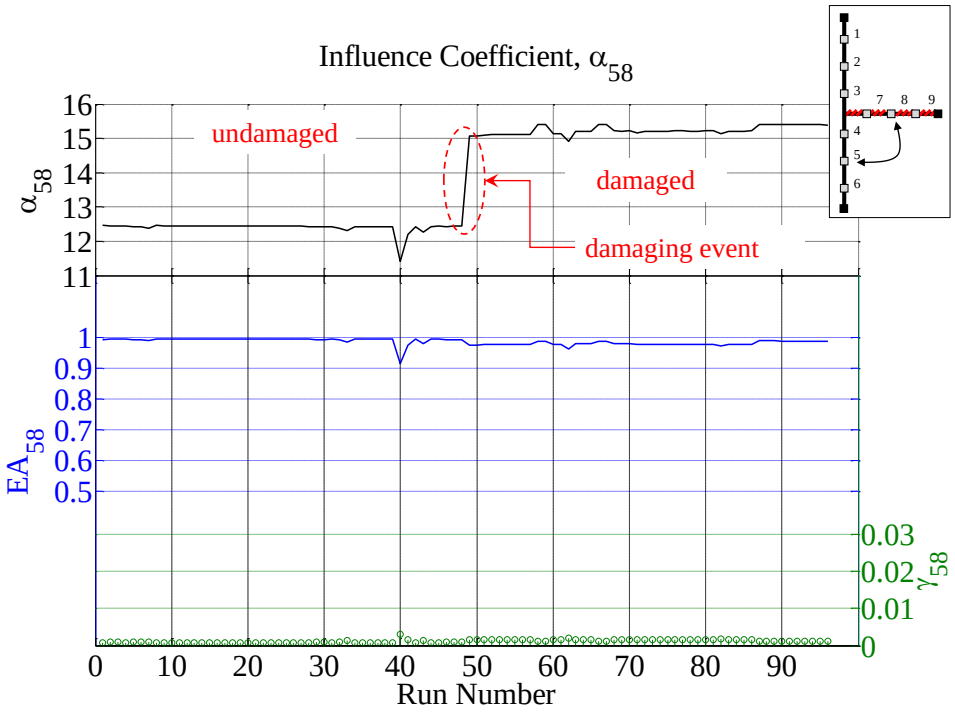

Figure 3.12. *α*, *EA*, and *γ* results for Region 3 pair

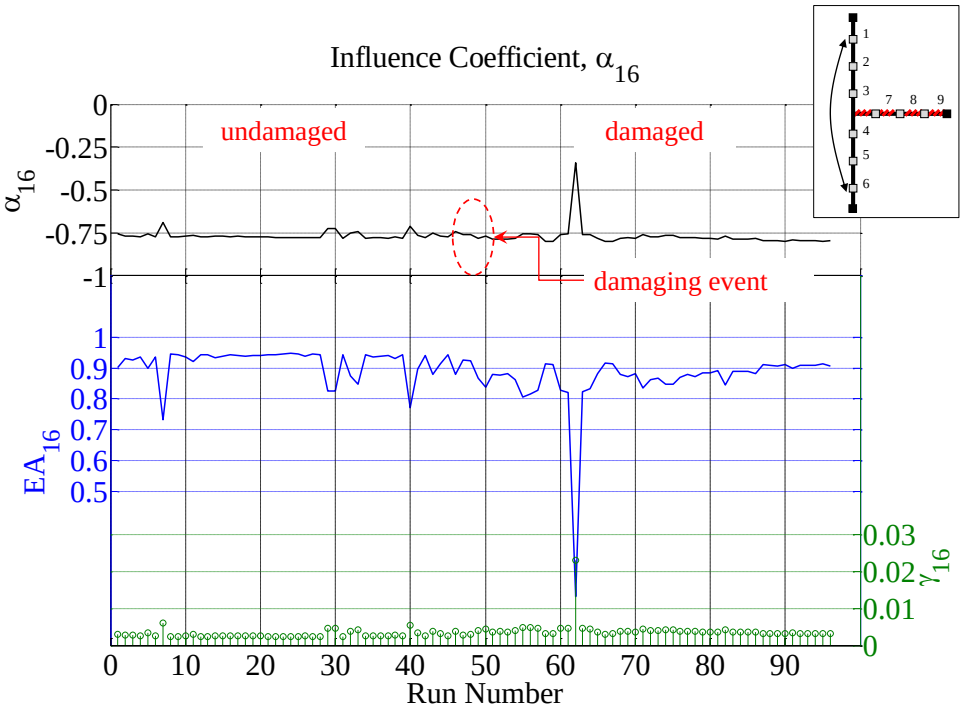

Figure 3.13. *α*, *EA*, and *γ* results for Region 8 pair

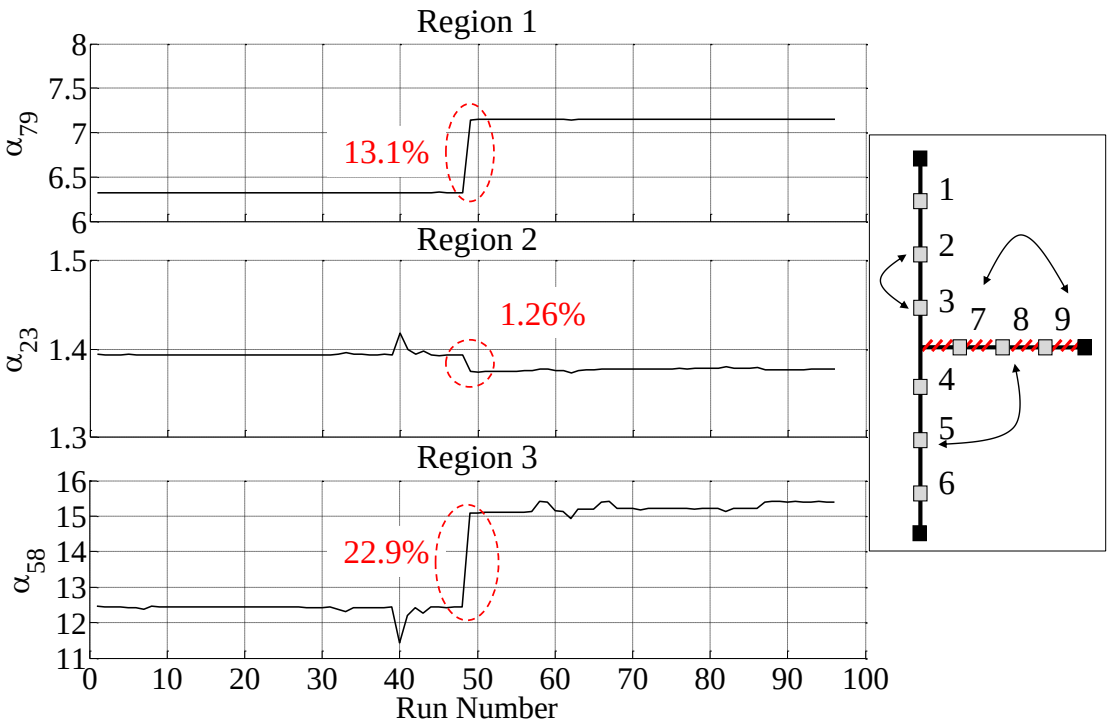

Figure 3.14. Comparison of % change for region 1, 2, and 3 pairs

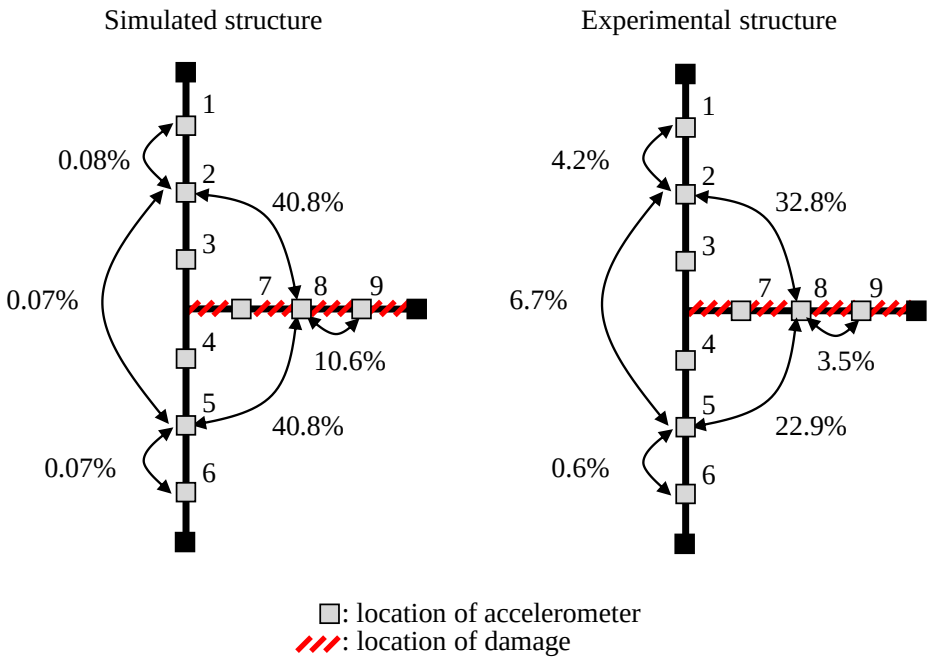

Figure 3.15. Comparison of relative change of coefficients between simulated and experimental structures

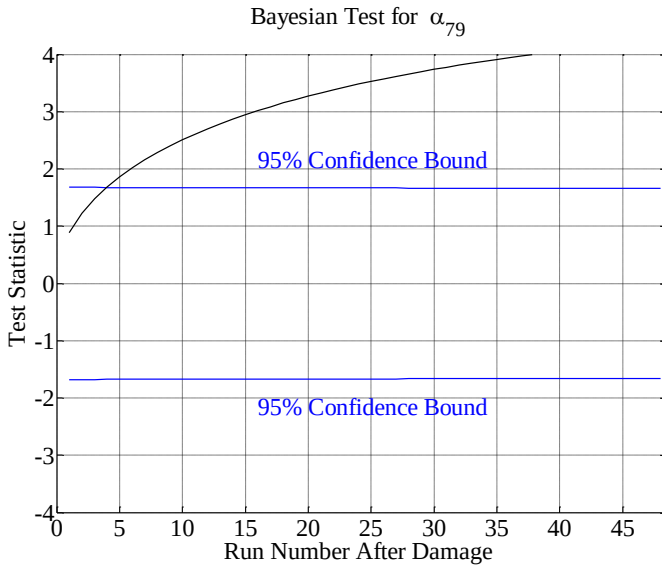

Figure 3.16. Hypothesis testing results for a region 1 coefficient

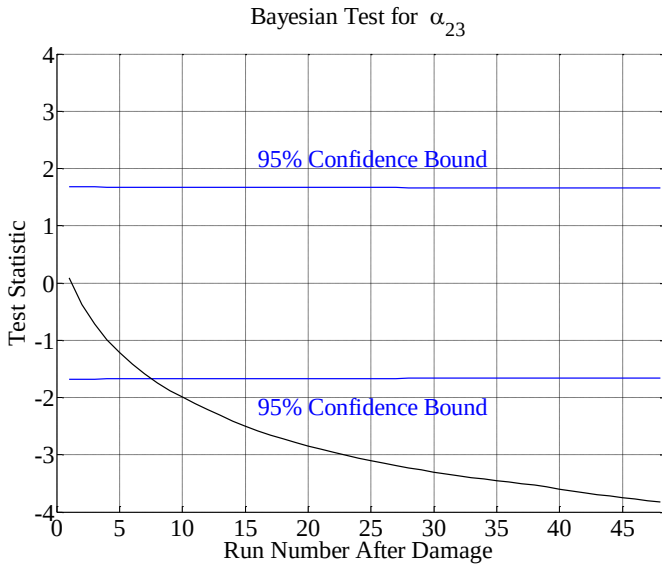

Figure 3.17. Hypothesis testing results for a region 2 coefficient

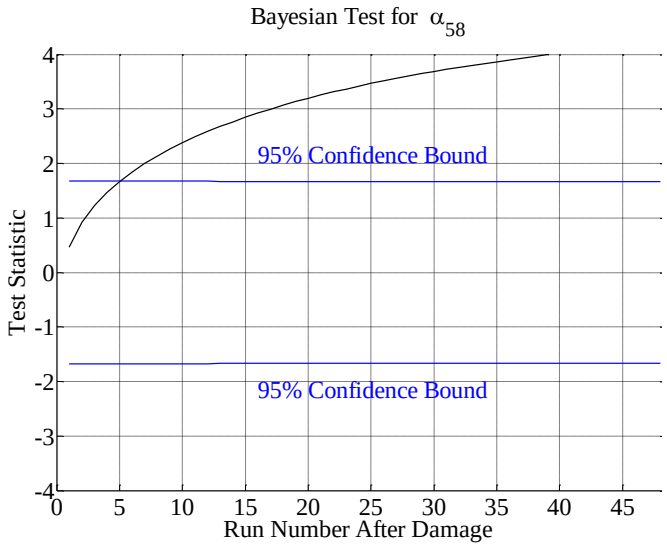

Figure 3.18. Hypothesis testing results for a region 3 coefficient

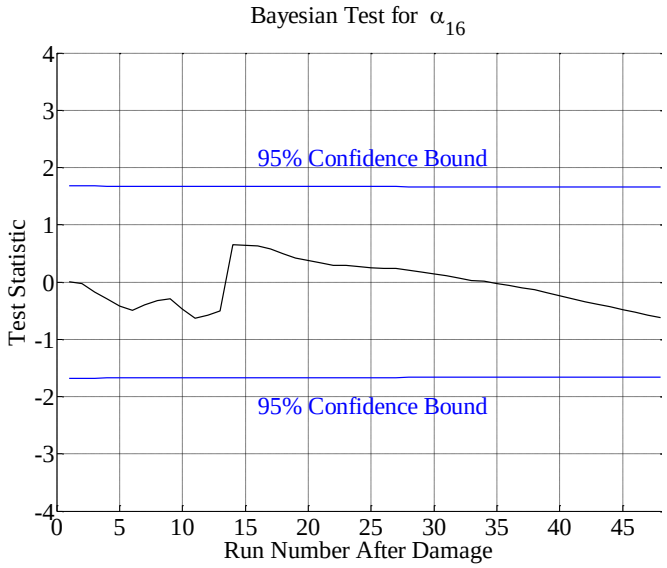

Figure 3.19. Hypothesis testing results for a region 8 coefficient

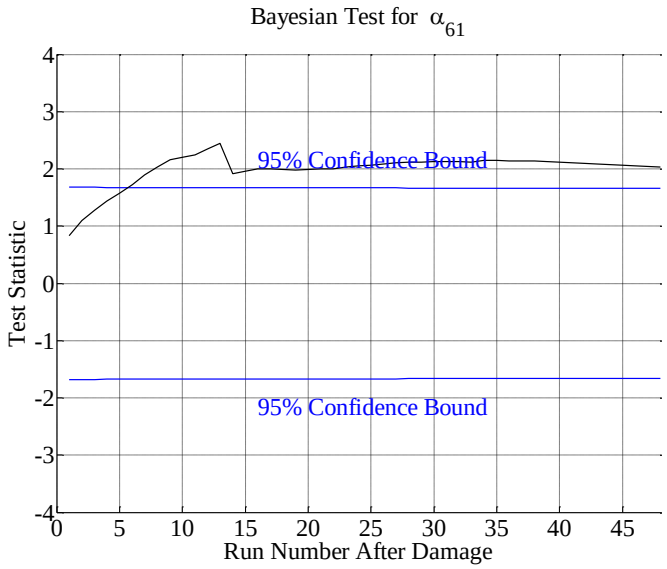

Figure 3.20. Hypothesis testing results for reciprocal of region 8 coefficient

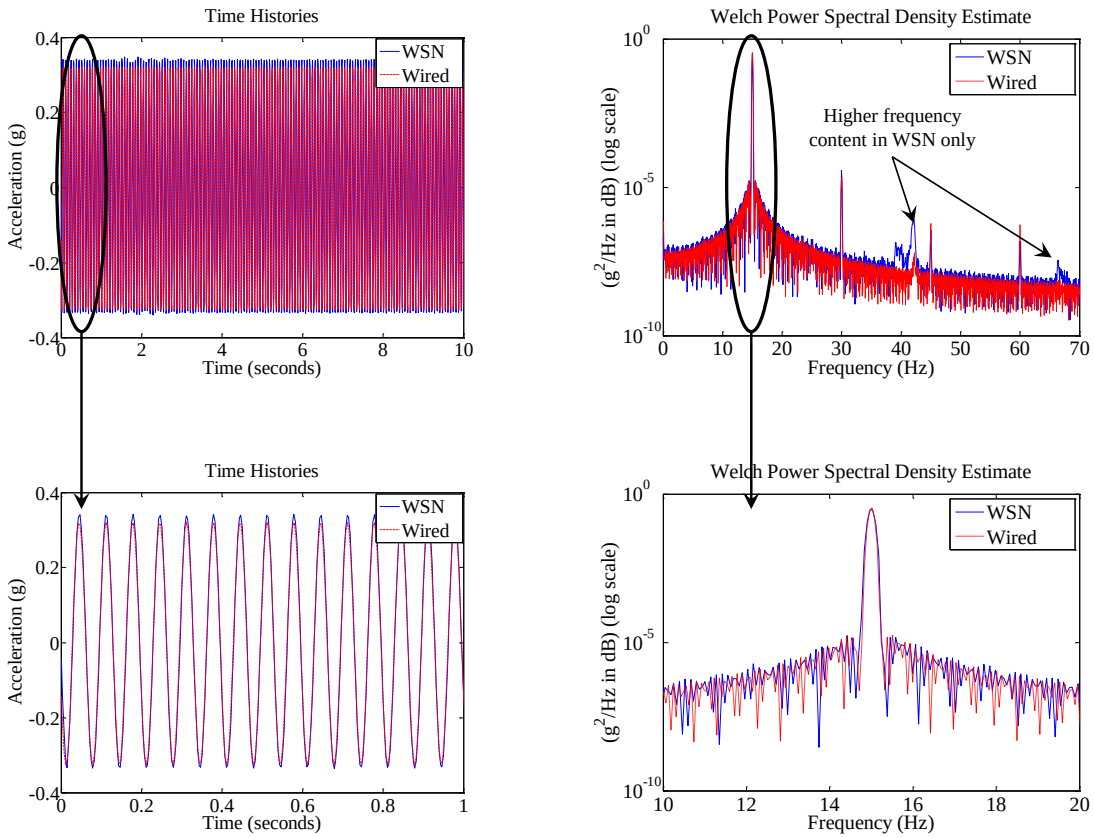

Figure 3.21. Comparison of wired versus wireless data in both the time and frequency domains for node 9

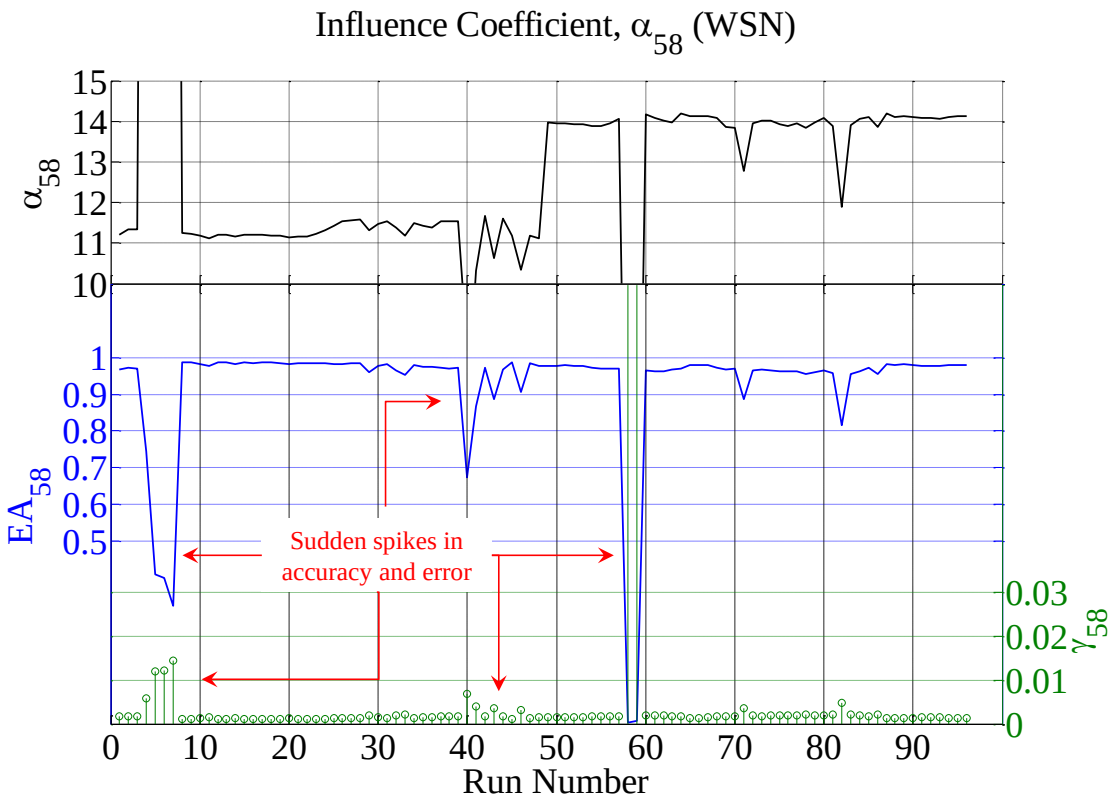

Figure 3.22. *α*, *EA*, and *γ* results for region 3 pair collected with the WSN

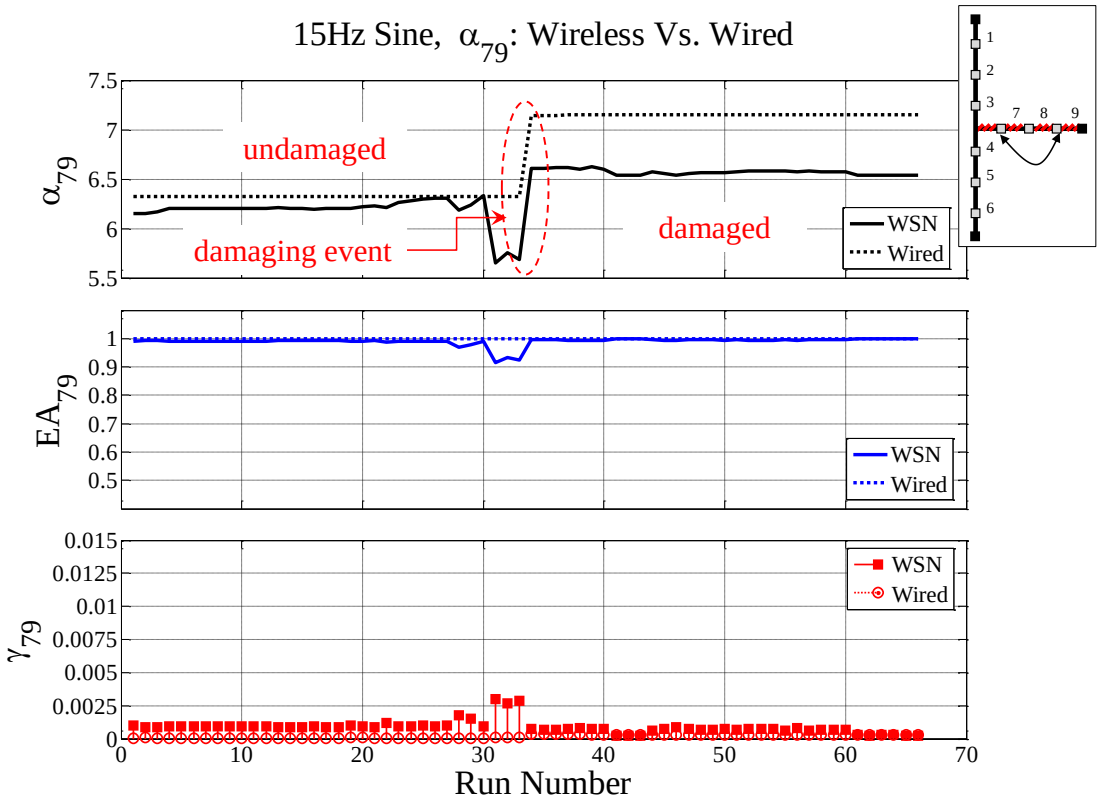

Figure 3.23. *α, EA,* and *γ* for a beam-beam node pair with inaccurate datasets removed

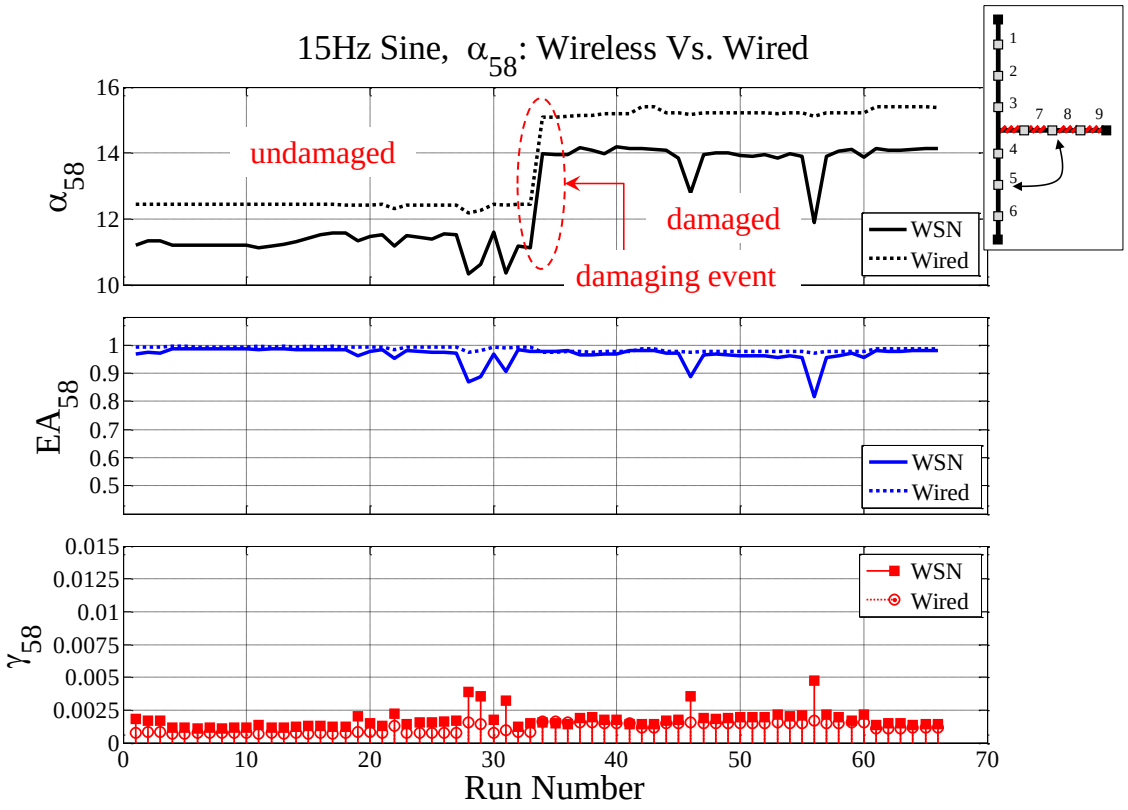

Figure 3.24. *α, EA,* and *γ* for a beam-column node pair with inaccurate datasets removed

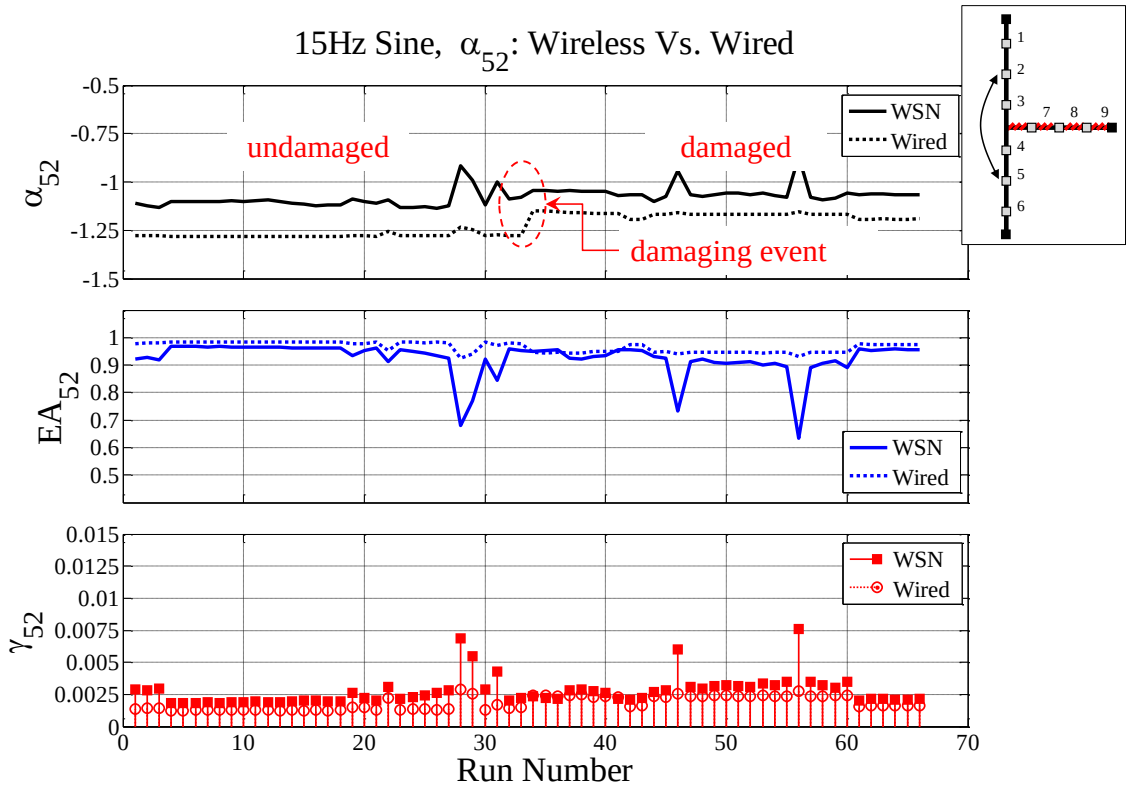

Figure 3.25. *α, EA,* and *γ* for a column-column node pair with inaccurate datasets removed

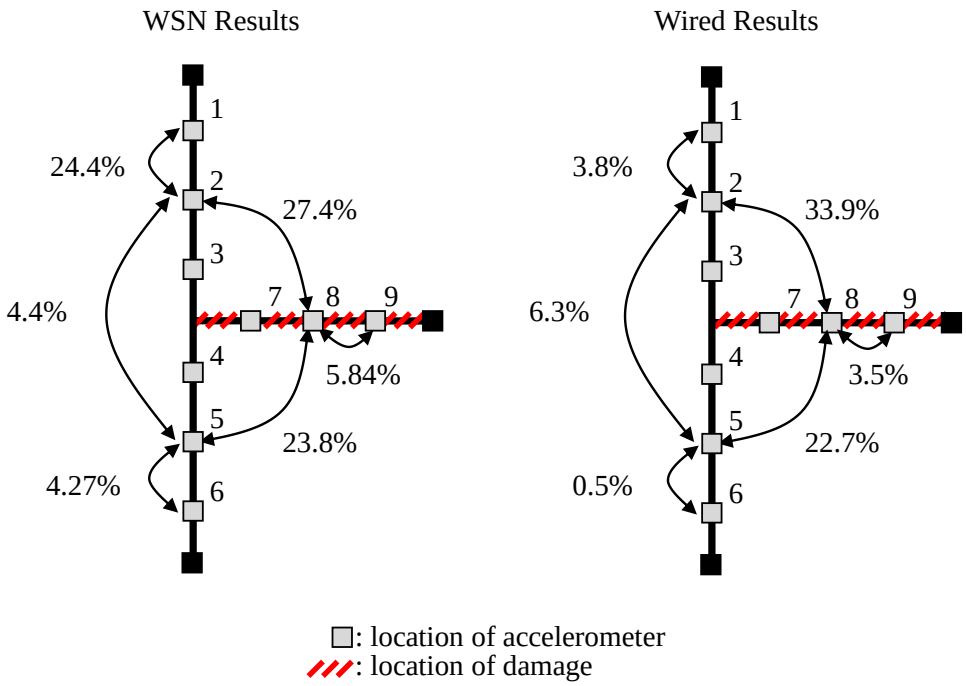

Figure 3.26. Comparison of relative change of coefficients between WSN and wired data

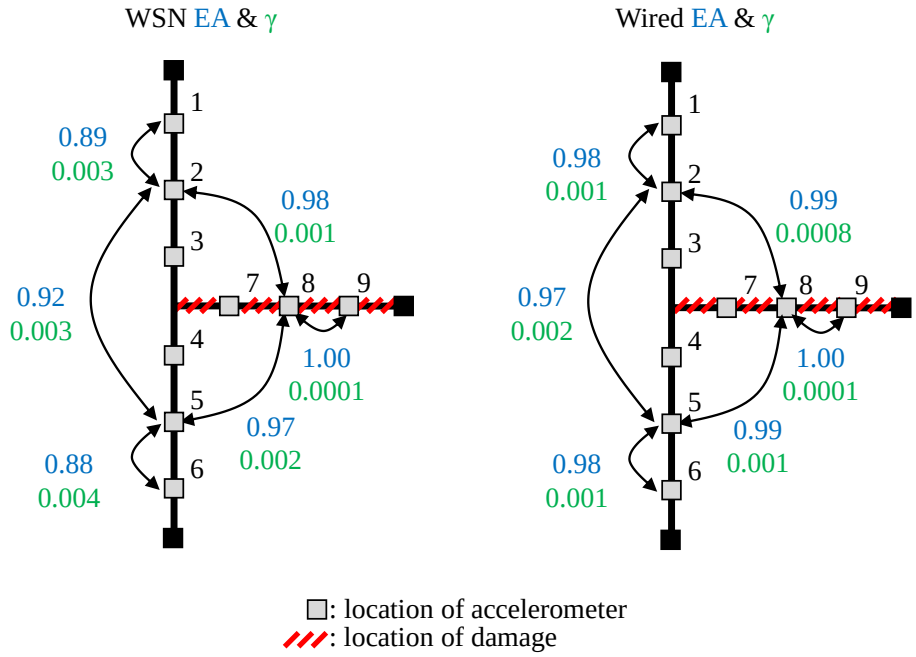

Figure 3.27. Comparison of average *EA* and γ for WSN and wired data

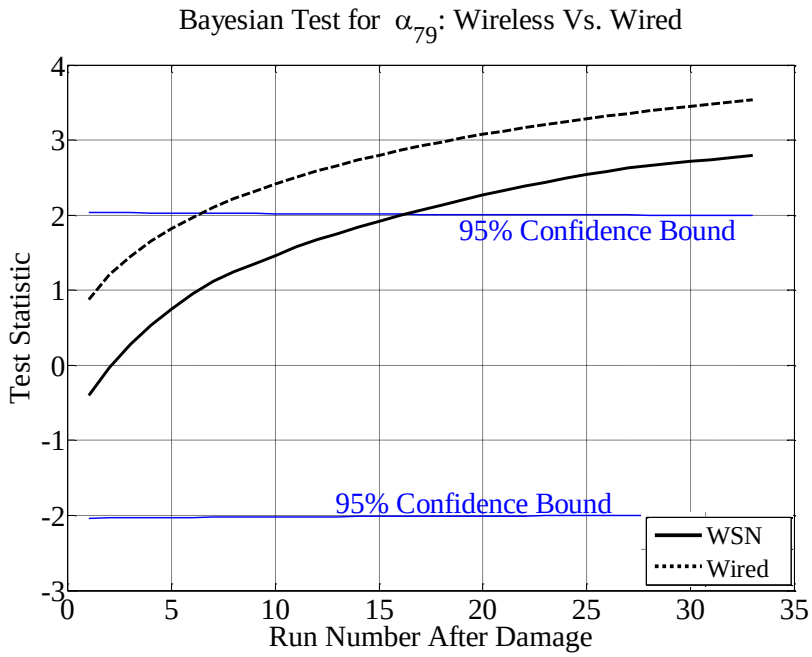

Figure 3.28. Hypothesis testing comparison of WSN and wired performance: beam-beam nodal pair

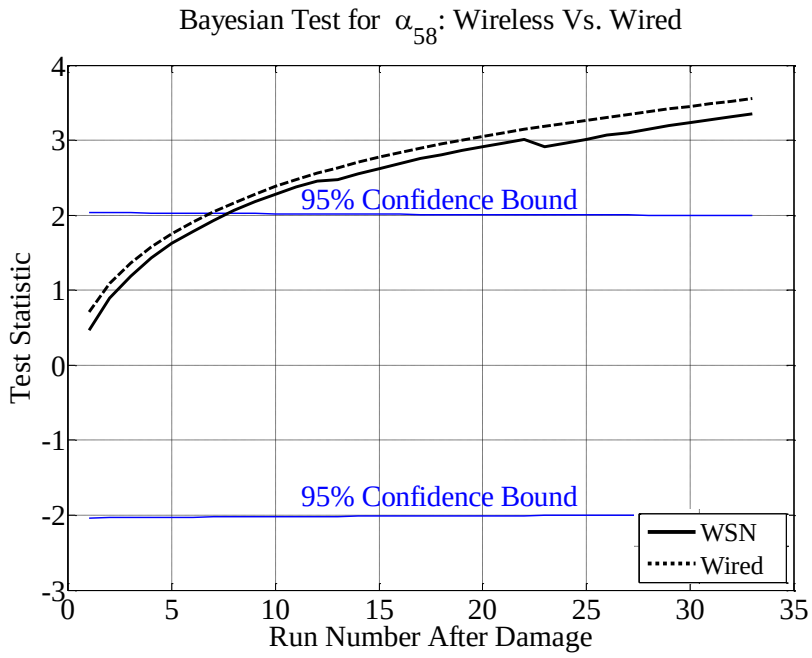

Figure 3.29. Hypothesis testing comparison of WSN and wired performance: beam-column nodal pair

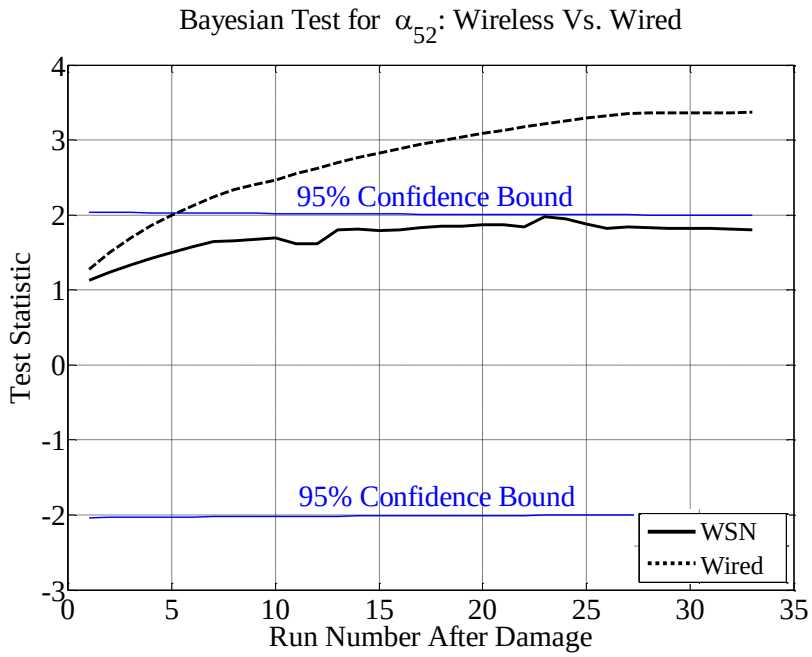

Figure 3.30. Hypothesis testing comparison of WSN and wired performance: column-column nodal pair

Chapter 4 Scaled Uneven Two-Bay Frame Testbed

4.1 Introduction

While Chapter 3 demonstrated the successful application of the proposed localized damage detection method on an experimental local beam-column joint, the model was simple and only allowed for one damage scenario. This chapter presents a more complex model, a shallow two-bay frame, that can emulate either a building frame or a bridge girder. The model allows for nine unique damage locations, to verify the robustness of the method by detecting different damage scenarios. The method is applied to both a simulated and an experimental frame. In addition to the dynamic testing implemented for collecting acceleration responses, static displacement data is used to compare the performance of the experimental prototype with that of the computer model and to update the model. The application presented further demonstrates the trends identified in Chapter 3 for effective damage detection.

4.2 Simulated Model

A simulated model was first developed to verify the performance of the damage detection method prior to constructing an experimental frame. The simulated structure is a two-bay plane frame with fixed connections, uneven spans, and short columns. The intent of this particular structure is to represent either a two-bay building frame or a two-span girder, as shown in Figure 4.1. The finite element software SAP2000 was use for creation of the model.

4.2.1 Properties of the Simulated Model

A mathematical model, consisting of 45 nodes and 44 elastic beam finite elements, has been developed and is shown in Figure 4.2. Elastic beam elements were chosen because the structure consists of beams and columns. Each element node has three degrees of freedom, u_x, u_y, and θ_z, which allows for translational and bending behavior. The frame is considered a "plane frame," which disallows out-of-plane and torsional degrees of freedom. Displacements, directly relating to accelerations, are observed at 21 nodes along the structure (labeled *L1* through *L6* at the left joint, *C1* through *C9* at the center joint, and *R1* through *R6* at the right joint) shown in Figure 4.2. Figure 4.3 shows the general location and direction of the displacement nodes along with the 9 designated damage scenarios. Each damage location was chosen to represent locations of potential damage: in the beams and columns near each joint and at the midspans of the beams.

For the baseline state, each element is a uniform hollow 2-inch tubing, with 0.083 in wall thickness, 0.6364 in^2 area, and a moment of inertia of 0.3905 in^4. The undamaged cross-section is shown in Figure 4.4(i). The steel is assigned an elastic modulus of 29,000 ksi.

Damage is simulated by switching the geometric properties of corresponding elements to that of a member with approximately a 20% stiffness reduction. For the damaged portions, the 2-inch square tube cross-section has a wall thickness of 0.065 in, a cross-sectional area of 0.5031 in^2, and a moment of inertia of 0.3143 in^4. The damaged cross-section is shown in Figure 4.4(ii). Damaged sections are 7.5 inches long, after accounting for plate connection thicknesses in the experimental structure. Sensor nodes are oriented around each damage section, with one sensor located at the midpoint of the

damage. All sensor nodes are organized 8 inches center to center measured from the centerline of the local joint. For both the baseline and damaged states, the boundary conditions are defined as fixed supports at the base of each column. Similar to the previous simulation in Chapter 3, mass of the structure is assumed negligible, as per the assumption stated in Section 2.2.1.2.

The frame elements were designed based on both the actual available sizes (McMaster-Carr 2010) and the desired acceleration values. An iterative process was used to determine the best combination of cross-sections, member lengths, and acceleration responses, preferred to be of similar order of magnitude in columns and beams. The spans were chosen to be of differing lengths to create more complexity in the structure.

4.2.2 Simulation Procedure

For both the undamaged and each of the 9 unique damaged cases, a white noise excitation was simulated at the far left joint in the x-direction. The resulting displacement responses were generated at each of the 21 nodes to represent sensor node locations along the beam and column members. Displacements of the beam members were simulated in the y-direction, while the column displacements were taken in the x-direction. Measurement noise was also accounted for by adding a Gaussian noise with a standard deviation equal to 5% of the root mean square of each response signal. Simulated results were generated for the undamaged case as well as for each of the 9 unique damage scenarios.

A tenth damage scenario was also simulated, called D_{exp}, which is a combination of cases *D8* and *D9*, involving a 20% stiffness reduction at both the right beam and the right column simultaneously. The purpose of this simulation was to check a case in which

larger damage occurs. The D_{exp} scenario is the damage scenario that was later used in experimental testing that will be discussed later. The results of all eleven simulations (undamaged and damaged) were then processed through the proposed localized damaged detection method to monitor the change between each damaged case compared to the undamaged baseline.

4.2.3 Damage Detection of Simulated Frame

Eleven simulation conditions were considered which include an undamaged baseline condition and 10 different damaged conditions, each characterized by a 20% reduction in the stiffness of a 7.5-inch portion of the structure at the locations indicated in Figure 4.3. It is important to note that this corresponds to only a 0.5% decrease in stiffness or less of the frame as a whole, as shown in Table 4.1. The rest of the structure maintains the same stiffness properties as the undamaged structure.

Damage detection was performed for each of the 10 damage simulations. As a means of inspecting the percentage changes for each node pair, the changes were averaged at each node within its respective joint. For example, all of the percent changes from each influence coefficient involving node *L1* regressed with *L2* through *L6* were averaged for the nodal percent change value at node *L1*. The values are only averaged on a joint level instead of throughout the whole structure because the nodes at the left joint are far removed from the nodes at the right joint. In a real structure, this will only become truer with longer spans. The nodal percent changes are shown for each simulated damage scenario in Figure 4.5 through Figure 4.14.

In 8 out of 10 cases (*D1, D2, D4, D5, D6, D8, D9,* and D_{exp}), the damage was accurately detected, with nodal percent changes near the damage location on the order of 2 to 10 times larger than those at the undamaged joints. The damage is not only localized to the correct joint with noticeable changes in the influence coefficients, but inspection of the changes at nodal level points even more locally to the damage. For example, in Figure 4.13, which shows the averaged percent changes for damage case *D9*, the largest changes at the right joint are in the column nodes. This is consistent with the 20% localized stiffness reduction at the right column. Therefore, the algorithm is sufficient in identifying the general location of damage within the structure as a whole, even though the overall stiffness reduction of the structure was negligible.

Furthermore, modal properties were simulated by adding a realistic level of mass for a typical structure to the simulated frame. Based on the first three modes, the modal properties of the structure change insignificantly with the occurrence of each damage scenario. This can be seen in Table 4.1, which shows the percentage change for modal frequencies of the first three modes from the undamaged to the damaged conditions. The percent changes range from approximately 0.0% to 1.4%. These minor changes would be undetectable in any modal-based global detection method with consideration of reasonable error. However, the proposed localized method detects the damage effectively despite the minimal changes in global properties.

4.3 Experimental Model

The algorithm was further verified through laboratory experiments on a specimen similar to that of the simulated model. These experiments were conducted at the Center for

Advanced Technology for Large Structural Systems (ATLSS) at Lehigh University. Again, the experimental frame, designed with short columns, can represent either a two-span bridge girder or a two-bay single-story building frame. The structure was instrumented with two sensor networks; one consisting of 21 wired accelerometers and another of 6 linear variable displacement transducers (LVDTs). The structure's responses were collected for both static tests and dynamic tests. For static testing, LVDT readings were taken for 20 undamaged and 20 damaged tests. This data was then used to compare the boundary conditions of the simulation in order to update the finite element model. For dynamic testing, acceleration and displacement responses were collected at each sensor node for 30 undamaged tests and 30 damaged tests. These tests were repeated for various excitation types. Using the acceleration data, the damage detection algorithm was employed. This experiment serves as a validation of the method on a more complex structure with more variety of damage and a larger sensor network.

4.3.1 Properties of the Experimental Specimen

Because ambient vibrations are the most common excitations experienced by a structure on a daily basis, this excitation type was the basis for the design of the experimental structure. As was mentioned in the discussion of simulated frame, the frame was iteratively designed with a specific range of desired excitations in mind. The frame was constructed using two-inch square steel tube sections, with overall span lengths of 7 feet 6 inches and 12 feet center to center, for the left and right spans, respectively. The three columns are of the same steel tube cross-sections with matching heights of 2 feet 9 inches.

An overall view of the experimental structure is shown in Figure 4.16. Identical to the simulated frame, the undamaged and damaged cross-sections were of 0.083-inch and 0.065-inch wall thicknesses, creating a 20% reduction in section stiffness for the damaged case. These damage sections were created by switching out a 7.5-inch long "member switchout" constructed with the 0.065-in tube section. End plates were welded on either end of the member switchouts as well as on the ends of the permanently undamaged portions of the structure for each through-bolt attachment. Figure 4.17 shows the member switchouts both unattached and attached to the structure. The end plate connections were designed for the moment capacity of the frame, so that these connections would not be a limiting point in the stiffness of a structure. For example, the stiffnesses can be considered as two springs in series, with the stiffness of the plate connection denoted as k_1 and the stiffness of the tube section denoted as k_2. The overall stiffness is then defined by the following equation:

$$\frac{1}{k} = \frac{1}{k_1} + \frac{1}{k_2} \tag{4.1}$$

From equation (4.1) it is obvious that as k_1 becomes large compared to k_2 the overall stiffness k depends only on k_2, the stiffness of the structural member itself. For ease of construction, these end plates were also designed with a cutout the size of the 2"x2" tube. However, in retrospect this created difficulty when welding in creating perfectly square and aligned members.

The support structure of the frame was designed as a continuous angle channel from which the columns of the specimen cantilevered out. The frame was oriented on its side in an attempt to address lateral stability concerns associated with a vertically-

oriented plane frame. Additionally, long rectangular plates stemmed orthogonally from the channel underneath each column to carry three adjustable "roller" supports at each of the beam-column joints. The support structure is shown in Figure 4.18. The adjustable supports at each joint were designed to keep the structure level. Adjustability of these supports was a major consideration as too much contact pressure could prevent the frame from deflecting as expected. Additionally, a layer of Teflon was applied to the plate between the support and the frame to reduce friction. The entire support structure was then placed on adjustable footings to allow for flexibility with leveling the structure. Figure 4.19 shows a close-up of the adjustable support on an adjustable footing.

4.3.1.1 Specifications of the Actuator and Load Cell

The actuator used for the dynamic testing in these experiments is the MODAL 50A actuator previously described in Section 3.3.2.1. Additionally, a load cell, model LC101-50, by Omega Engineering, Inc. was employed in these tests to measure the amplitude of the force applied by the actuator (2005). This load cell was also used to apply a static force for the static testing portion of these experiments. The load cell has a peak force of 50 lbs. Both the actuator and load cell are shown attached inline to the left joint of the experimental frame in Figure 4.20.

4.3.1.2 Sensing Systems

The specimen was instrumented with two sensing systems. The first is a network of 21 wired accelerometers located at 8-inch intervals around each of the three local joints (6 each at the left and right joints and 9 at the central joint). The second system is a network

of 6 LVDTs for collecting displacement responses at each of the 3 columns, at each of the 2 midspans, and the overall lateral displacement of the frame.

4.3.1.2.1 Wired MEMS Capacitive Accelerometers

The network of 21 accelerometers uses model number 2210-002 manufactured by Silicon Design, Inc (2010). The 2210-002 is a sensor that incorporates a 1210L micromachined capacitive accelerometer. This model can detect accelerations within the range of ± 2 g with an output noise of 13 μg/√Hz output noise. Other specifications for these sensors are summarized in Table 3.4. Figure 4.21 shows one of these sensors mounted on the test specimen.

4.3.1.2.2 Wired Linear Variable Displacement Transducers

In order to measure displacements, 6 LVDTs were implemented. The model of the LVDTs is GHSD 750-250 produced by Macro Sensors (2010). The measurement range of the LVDTs was ± 0.25 inch with a resolution of $7x10^{-6}$ in. These particular sensors consist of a spring-loaded shaft connected to the core of the LVDT. When the shaft position changes due to positive or negative displacement changes, the LVDT operates on a DC input and generates a precalibrated DC output. Figure 4.22 shows an LVDT attached to the test specimen.

4.3.1.2.3 Data Acquisition System

Both acceleration and displacement responses, in addition to the load cell reading, were collected using the CR9000 DAQ system and PC9000 support software presented in Section 3.3.2.2.3. For this experiment, the data was collected at a 500 Hz sampling rate

(0.002 sec sampling interval). Dynamic testing was conducted for a total of 10,000 samples per node per test, while static tests were performed for a total of 50,000 samples per node per test.

4.3.2 Static Testing

Prior to the dynamic loading, static tests were conducted to verify that the structure was behaving as expected, with displacements increasing as damage occurred. Additionally, the static responses data, collected via LVDTs, was compared to simulated displacements from two SAP models (one with fully fixed boundary conditions and one with fully pinned conditions) the restraints of which are summarized in Table 4.3. For this comparison, a simplified model with only 29 nodes and 28 finite elements was created, as seen in Figure 4.23. Instead of the 21 sensor nodes, displacements are observed at 6 different nodes, corresponding to 6 LVDT locations on the experimental structure. Figure 4.24 shows the locations of the LVDTs on the experimental structure as well as the damage locations (D8 and D9) for the damaged case.

The loading condition comprised of a 30-lb static force applied in the x-direction at the top of the left column. The load was applied at the level of the centerline of the beam. This load is less than 2% of the load required to cause yielding in the frame, which ensured linear-elastic behavior. The capacity of the experimental load cell (peak load of 50 lbs) used in the experiments limited this load value. Small loads also attempt to reflect behavior of the structure under ambient loading. For the experimental structure, a total of 40 tests were collected, 20 undamaged and 20 damaged. As previously stated, each test

contained approximately 50,000 samples at the static load, collected at a 500 Hz sampling rate.

Because it is difficult to control the exact load in the experimental setting, the displacements were normalized in terms of inch-per-pound for direct comparison. Figure 4.25 presents the normalized results for the undamaged and damaged cases for both simulated models and the experimental average. From this plot it can be seen that the experimental boundary conditions, shown in Figure 4.25, are not truly fixed, but rather fall somewhere between an idealized fixed and pinned condition. Therefore, there is a need for an updated model, in which the stiffness of the support connections is somewhere between that of a fixed and a pinned case, to be able to reflect the actual conditions of the experiment for more accurate comparisons. Additionally, the plot shows that the overall displacements did decrease, according to expectation, with the occurrence of damage as the damage increased the flexibility of a portion of the structure.

4.3.2.1 Updated Finite Element Model for Simulation

Using the results of the undamaged static tests, an update finite element model for the frame was created. The resulting updated model consists of pinned supports with a rotational spring at each support to add varying degrees of stiffness to reflect the physical behavior of the experimental structure. The updated simulated model with spring stiffnesses is shown in Figure 4.26. Simulated results were regenerated with this new model and are shown compared to the experimental results in Figure 4.27. These results show a significant improvement in the model's ability to reflect the experimental frame's true behavior. However, the updated model still shows a noticeable deviation from the

actual displacements measured at LVDT 2. Thus, future updating for this model should consider a greater number of variable parameters than the three support conditions.

4.3.3 Dynamic Testing

Because a real structure experiences dynamic loading on a continuous basis from ambient forces, dynamic testing was conducted for applying the localized damage detection method. A total of 60 tests were performed, comprised of 30 undamaged and 30 damaged runs. The simulated damage is the same as that for the static testing, with the far right beam switchout and the far right column switchout set to the damaged cross-section, each achieving a 20% localized stiffness reduction.

4.3.3.1 Forcing Frequency

For the dynamic testing it was important to first determine the optimal force type and forcing frequency for the conducting the tests. Both harmonic and random excitations were considered. While a random excitation would most closely resemble ambient vibrations of a structure, a harmonic excitation has the added benefit of easily identifying noisy data. However, for a harmonic excitation various forcing frequencies can affect the structure in different ways, thus, preliminary results at multiple frequencies were explored—5 Hz, 12 Hz, and 30 Hz. Additionally, preliminary results were produce using a white noise excitation (200 Hz bandwidth) for comparison. The times histories of the applied load, acceleration responses, and displacement responses for each loading type are shown in Figure 4.28 through Figure 4.31. The benefit of a low forcing frequency is the ability to achieve higher amplitudes of load and responses, which translates to higher

signal to noise ratios. However, the acceleration responses decrease in visual noisiness as the forcing frequency increases, with the harmonic becoming more dominant. This suggests that although a lower frequency force, such as 5 Hz, has a higher amplitude, the higher frequency noise is more dominant within the time history data.

Additionally, there is a trade-off for lower frequencies due to a phenomenon observed in data using the MODAL 50A actuator. When looking at the data in frequency domain the data shows recurring peaks at intervals equal to the forcing frequency. Figure 4.32 through Figure 4.36 show the frequency content of the acceleration responses for each forcing type plotted in a logarithmic scale. Note, these peaks cease after about 90 Hz in all four plots due to the CR9000's built-in low-pass filter. In the frequencies from 0 to 90 Hz, this phenomenon creates a large number of peaks in the 5 Hz data, which can corresponds to noisy very noisy data. While the 12 Hz data also has recurring peaks, they are not as plentiful as that of the 5 Hz forcing frequency, resulting in cleaner power spectra. The 30 Hz power spectra exhibit the least number of recurring peaks; however, there exists other higher frequency noise peaks from about 45 to 90 Hz that are independent of these peaks. This added noise could be due to possible shaking of the support from a more aggressive forcing frequency. The random force spectra shows constant peaks from 0 to 90 Hz, making it difficult to distinguish between noise in the data and frequencies associated with the force itself.

The four forcing types can also be compared using the accuracy and error parameters from the damage detection method, EA and γ. In order to consider these values from a higher level, averages were taken for each node within a local joint, similar to the averaging of percent changes in Section 4.2.3. These values are presented in Figure

4.36 through Figure 4.39 for *EA* and Figure 4.40 through Figure 4.43 for γ. Comparison of these sets of parameters shows that the 12 Hz sine data and the 30 Hz sine data are on par for the highest accuracy values. However, the 12 Hz data shows the lowest error associated with its data sets. Based on all of these comparisons, of the four forcing types, the optimal force was determined to be 12 Hz sine, the results of which are presented hereafter.

4.3.3.2 Preliminary Results

The 12 Hz sine data was processed using the proposed localized damage detection method for preliminary assessment. Because the total number of possible pairwise coefficients is 420 if considered throughout the whole structure, only local joint pairs were considered, narrowing this number down to 132 coefficients. Additionally, the *EA* and γ were used to identify the most reliable coefficients to consider, leaving 24 coefficients with accuracies above 90%. Because these coefficients contain regression reciprocals, α_{ij} and α_{ji}, only 12 are necessary for comparison. Figure 4.44 shows the relative percent changes for each of these 12 coefficients from the undamaged to damaged states. It also contains averaged values, per portion of the structure, considering only these high accuracy values. Some pairwise coefficients performed along the lines of the expectation set by the Chapter 3 results, with nodal pairs surrounding the damage showing the highest change in their influence coefficient value. For example, $\alpha_{R3\text{-}R2}$, $\alpha_{R4\text{-}R5}$, and $\alpha_{R6\text{-}R5}$ are in the vicinity of the two damage locations and show notable changes. Additionally, $\alpha_{L2\text{-}L3}$, $\alpha_{L4\text{-}L5}$, and $\alpha_{C7\text{-}C8}$ are remote from the damage locations and show

negligible changes. Plots of the α, EA, and γ for three of these pairs are shown in Figure 4.45, Figure 4.46, and Figure 4.47.

On the other hand, a few of these coefficients, for example $\alpha_{L4\text{-}L6}$ and $\alpha_{C5\text{-}C6}$, experience larger changes than expected given their vicinity with respect to damage. From these preliminary results, it is evident that some pairs perform as expected according to the results presented in Chapter 3, while others did not. These discrepancies could be due to possible experimental imperfections, such as difficulty maintaining levelness and squareness of the structure when switching the structured between the undamaged and damaged states. These potential issues should be further investigated and addressed in future research using this specimen. Another potential cause of these unexpected results, as well as for the larger number or inaccurate coefficients (only 24 of 132 coefficients exhibited high accuracy), is that linear regression between two nodes is insufficient to capture the true behavior of this more complex structure. Therefore, the application of multivariate regression should also be considered.

Table 4.1. Global effects of damage per damage case

Damage Case	Damage Location	Overall Stiffness Reduction	Mode 1 Frequency % Change	Mode 2 Frequency % Change	Mode 3 Frequency % Change
D1	Left Column	0.38%	0.00%	0.20%	0.15%
D2	Left Beam	0.51%	0.00%	0.28%	0.05%
D3	Left Midspan	0.00%	0.04%	0.00%	1.40%
D4	Center Beam (Left)	0.38%	0.04%	0.25%	0.05%
D5	Center Beam (Right)	0.25%	0.36%	0.10%	0.15%
D6	Center Column	0.51%	0.44%	0.13%	0.52%
D7	Rigth Midspan	0.00%	1.25%	0.03%	0.03%
D8	Right Beam	0.32%	0.20%	0.28%	0.00%
D9	Right Column	0.45%	0.16%	0.23%	0.00%
Dexp	Right Beam & Right Column	0.83%	0.32%	0.50%	0.02%

Table 4.2. Specifications of Silicon Designs 2210-002 accelerometers

Measurement Range	± 2 g
Voltage Sensitivity	2000 mV/g
Output Noise	13 µg/√Hz
Temperature Range	-40 to +185 °F

Table 4.3. Boundary condition restraints for static testing simulations

Node	Boundary Condition Restraints	
	Model A	Model B
1	x, y, z, θx, θy, θz	x, y, z, θx
14	x, y, z, θx, θy, θz	x, y, z, θx
26	x, y, z, θx, θy, θz	x, y, z, θx

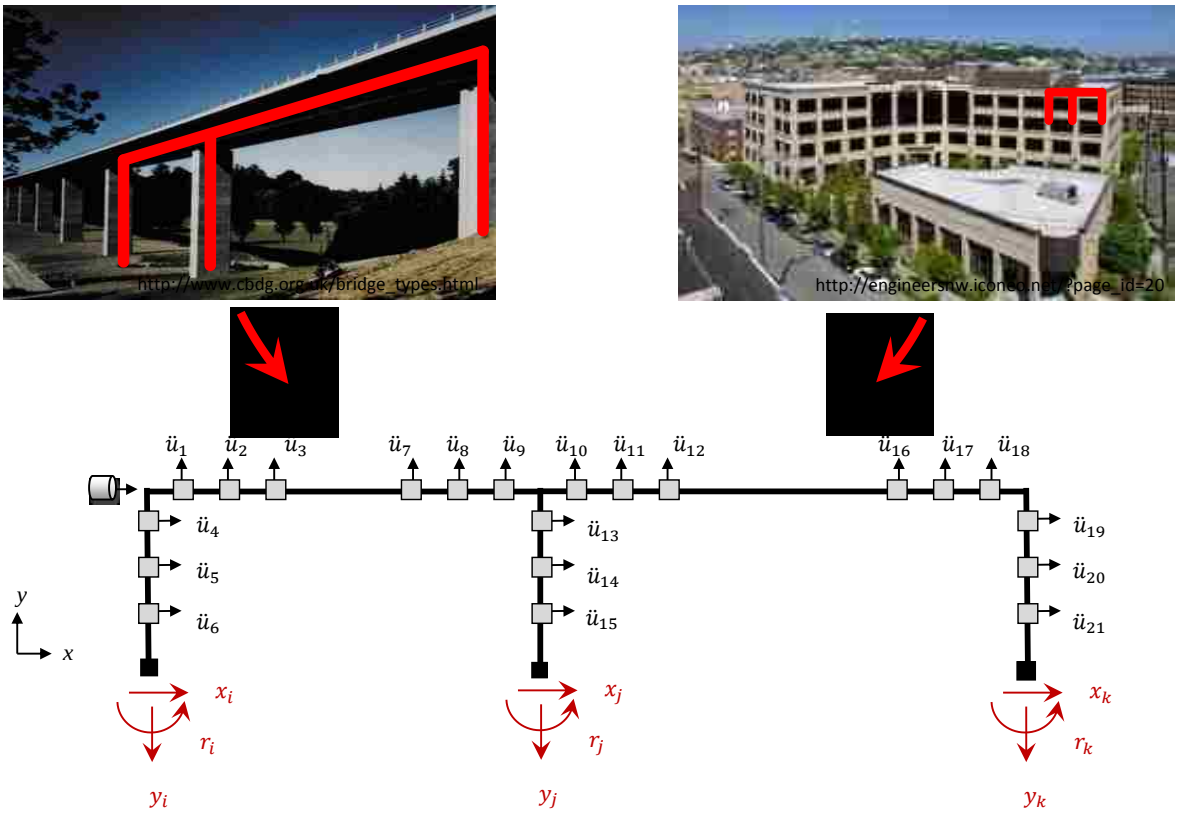

Figure 4.1. Two-bay frame can represent either a two-span bridge girder or a two-bay building frame

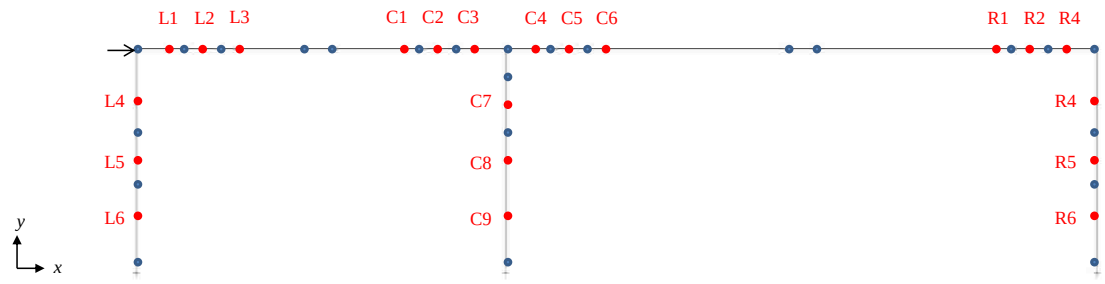

Figure 4.2. SAP2000 model with 45 nodes and 44 elements

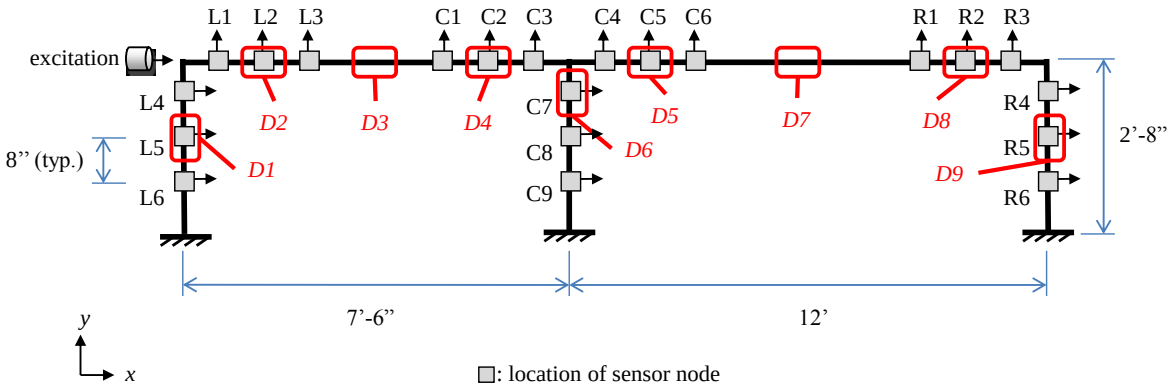

Figure 4.3. Simulated two-bay frame with 21 sensor nodes and 9 damage locations

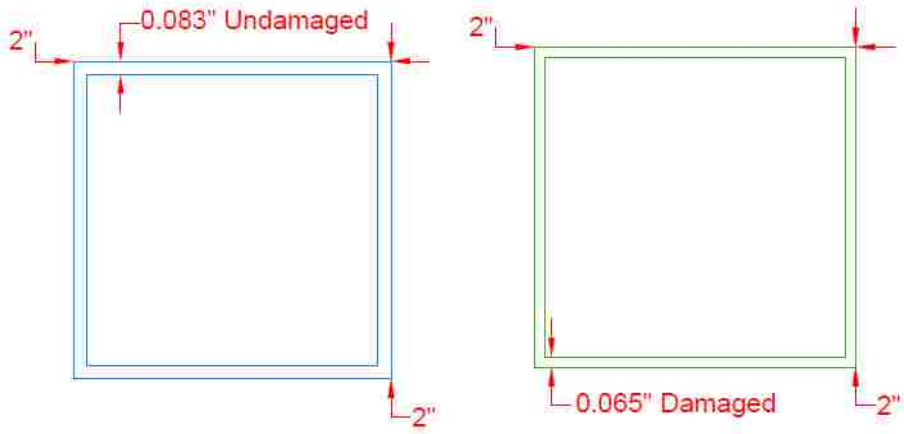

(i) (ii)

Figure 4.4. Cross-sections for (i) undamaged and (ii) damaged members

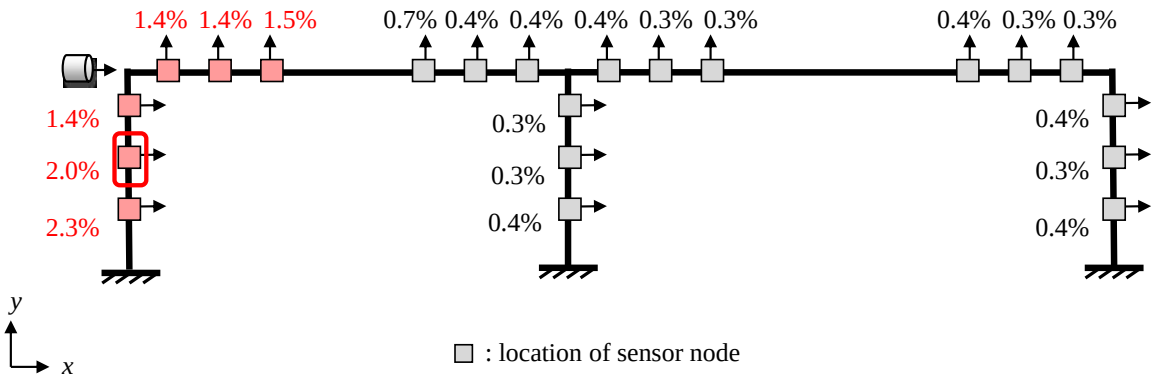

Figure 4.5. Relative % change for simulated damage case D1

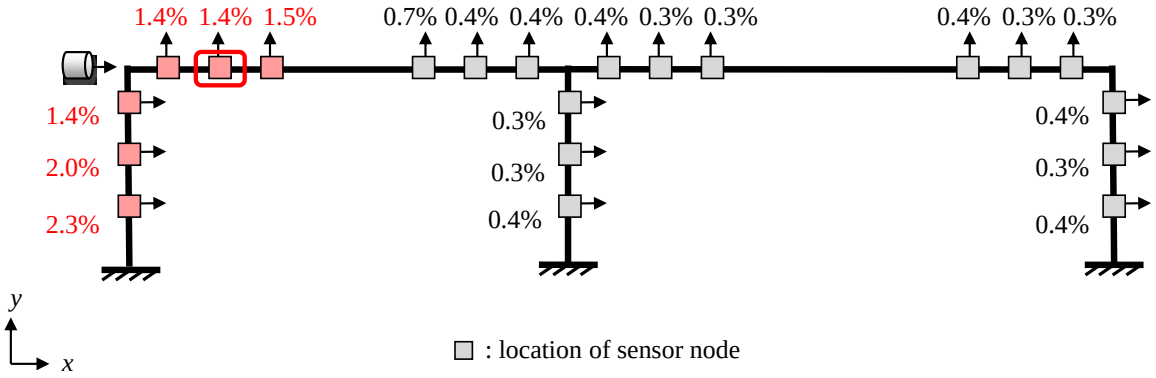

Figure 4.6. Relative % change for simulated damage case D2

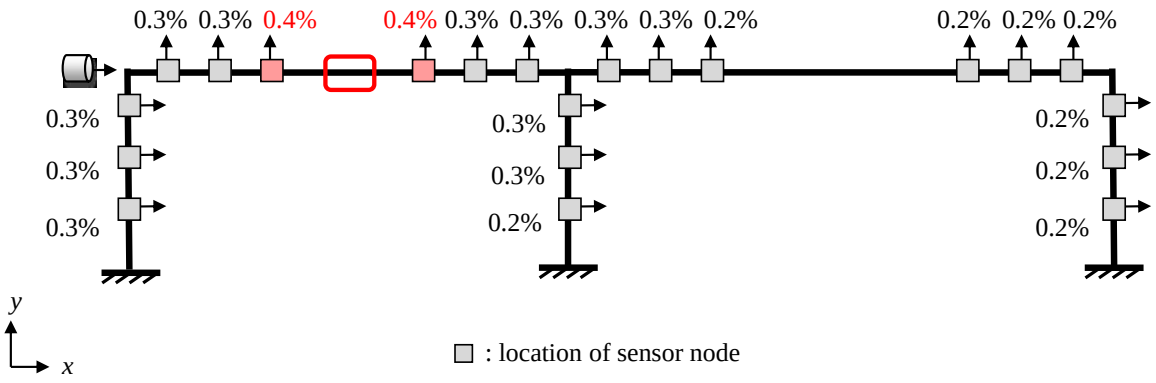

Figure 4.7. Relative % change for simulated damage case D3

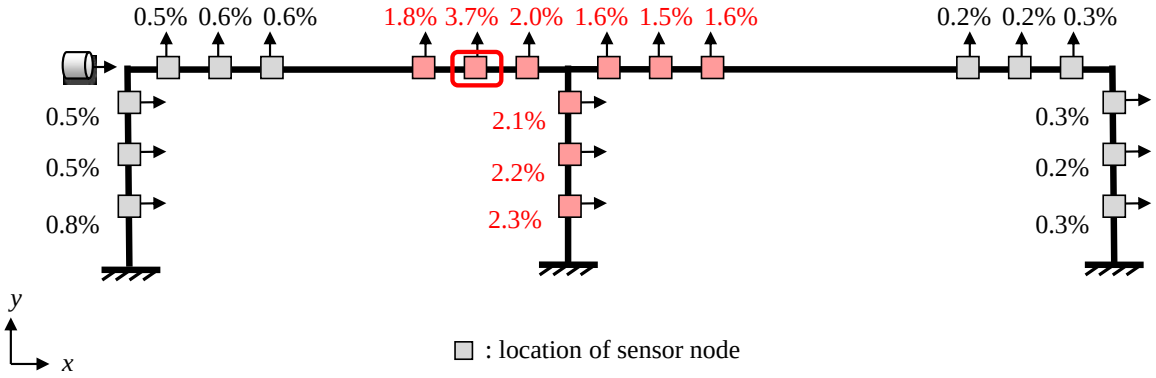

Figure 4.8. Relative % change for simulated damage case D4

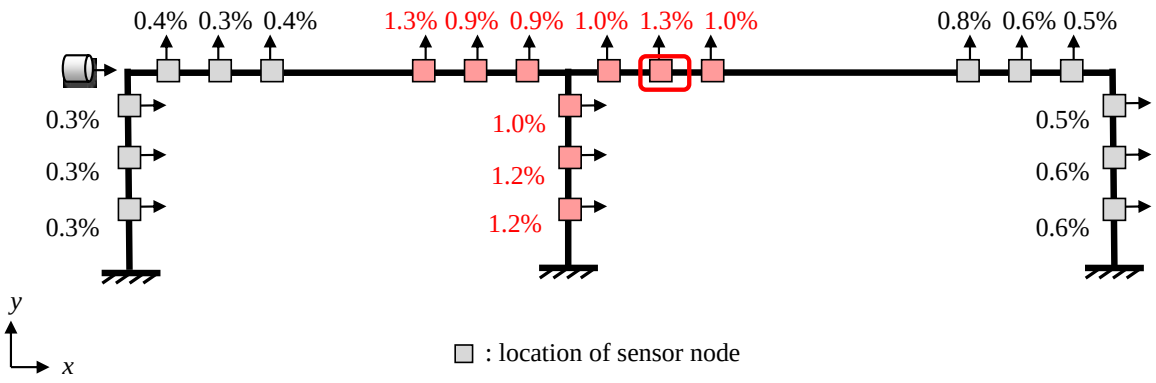

Figure 4.9. Relative % change for simulated damage case D5

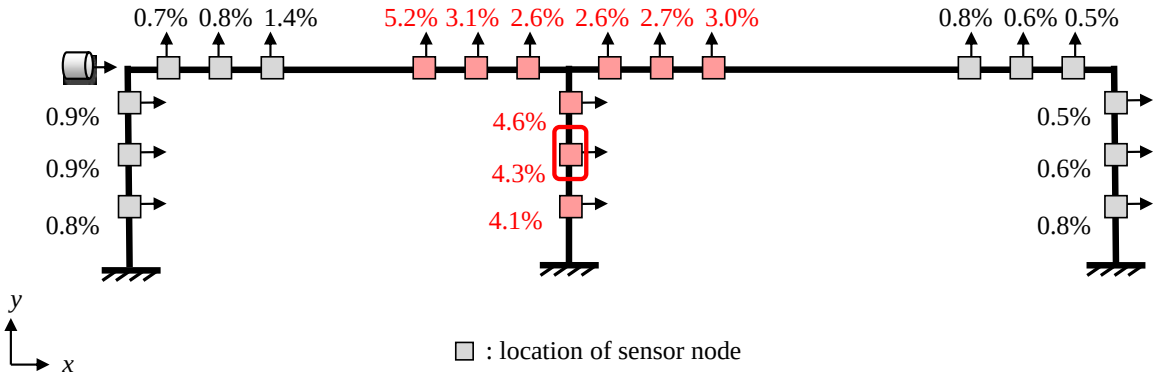

Figure 4.10. Relative % change for simulated damage case D6

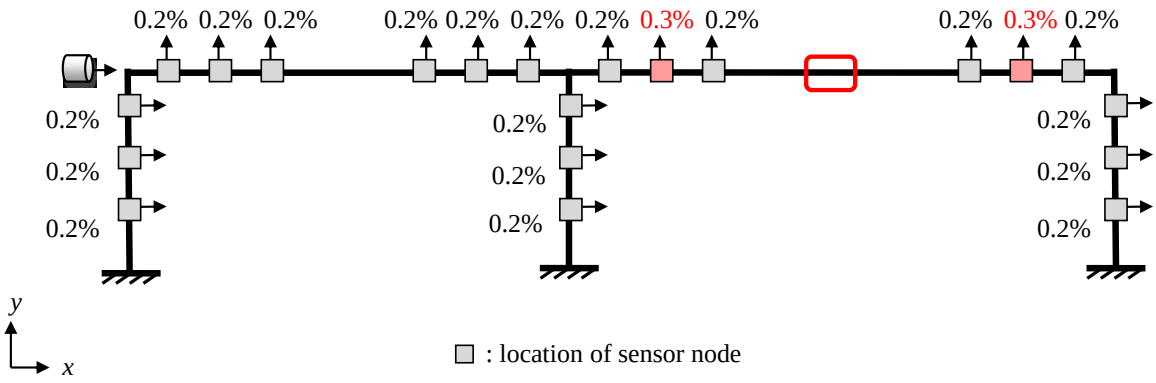

Figure 4.11. Relative % change for simulated damage case D7

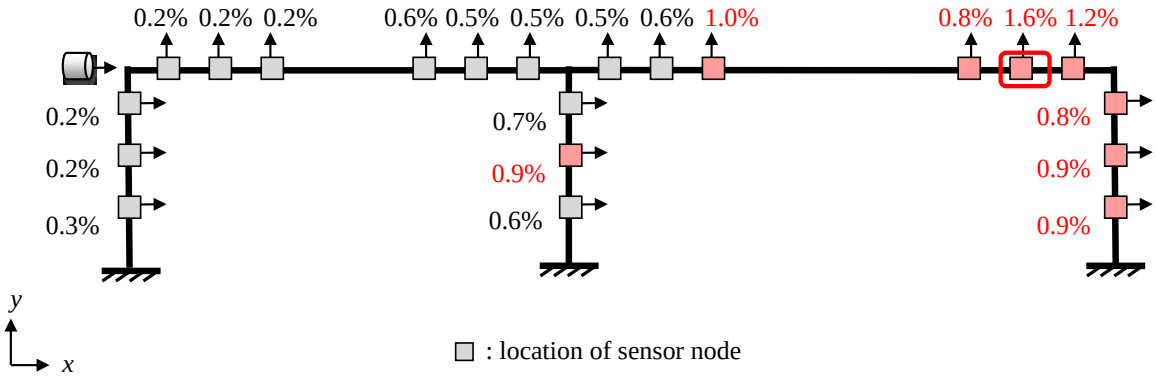

Figure 4.12. Relative % change for simulated damage case D8

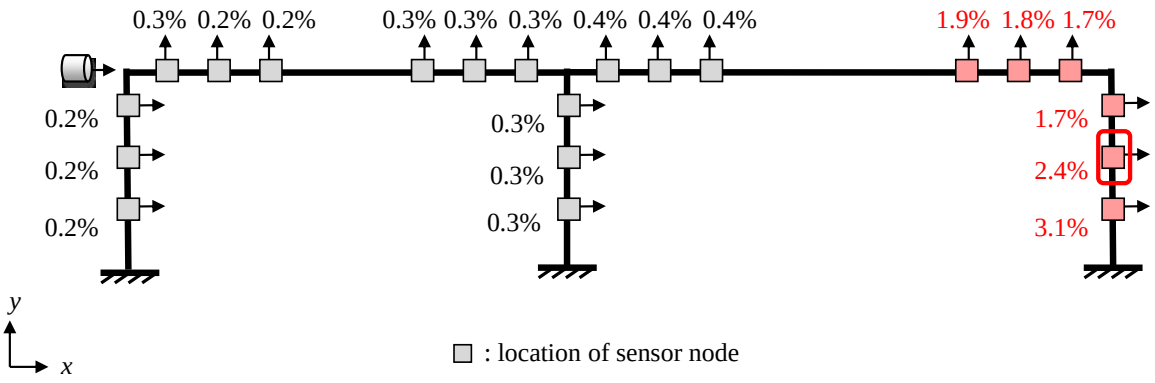

Figure 4.13. Relative % change for simulated damage case D9

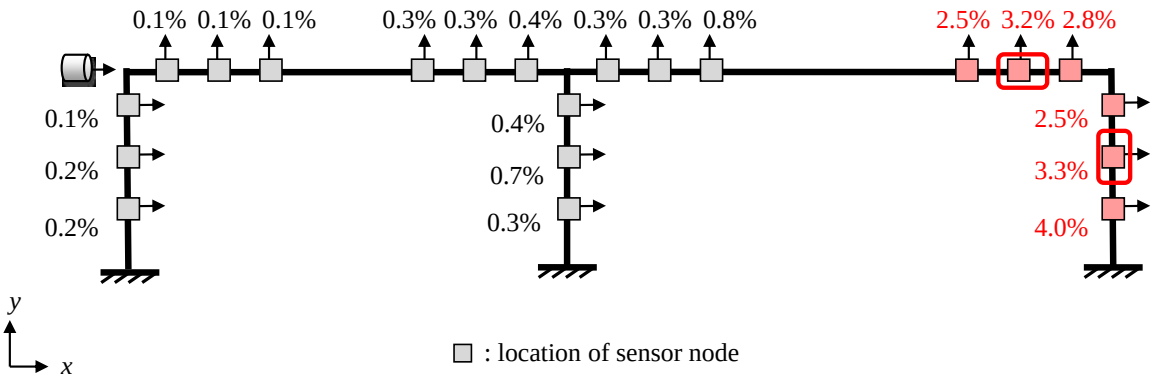

Figure 4.14. Relative % change for simulated damage case D_{exp}

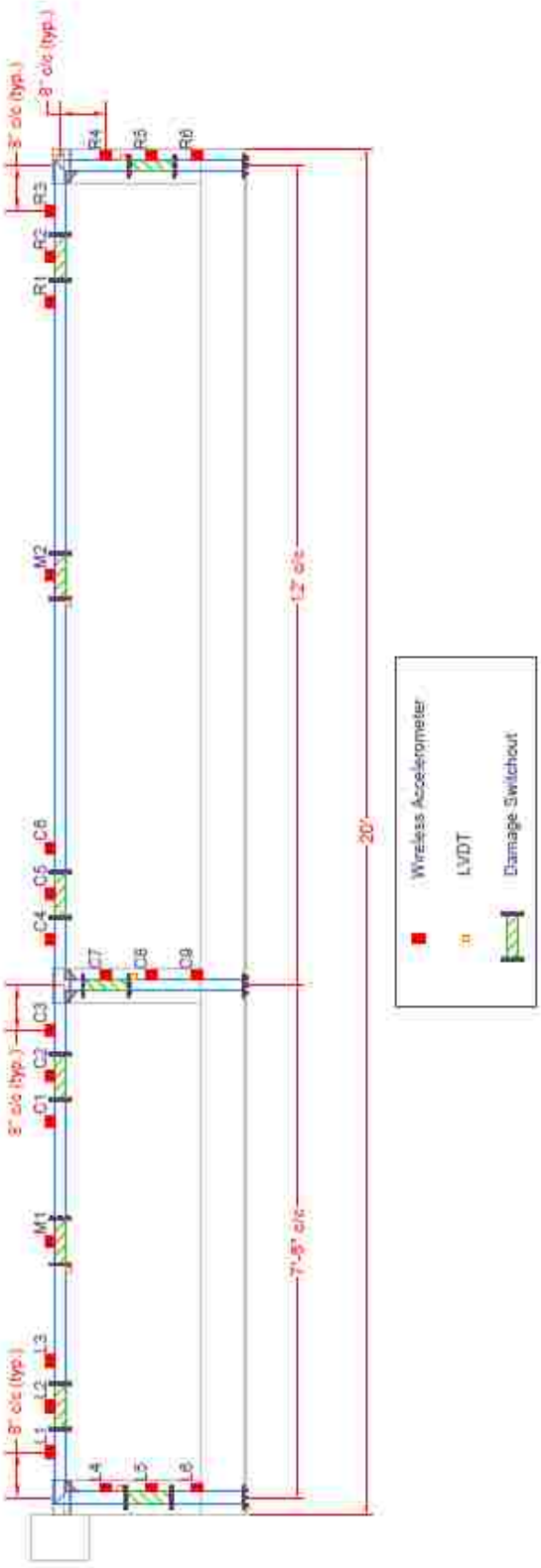

Figure 4.15. Experimental frame plans with switchout and sensor locations

Figure 4.16. Experimental frame constructed at the ATLSS Center

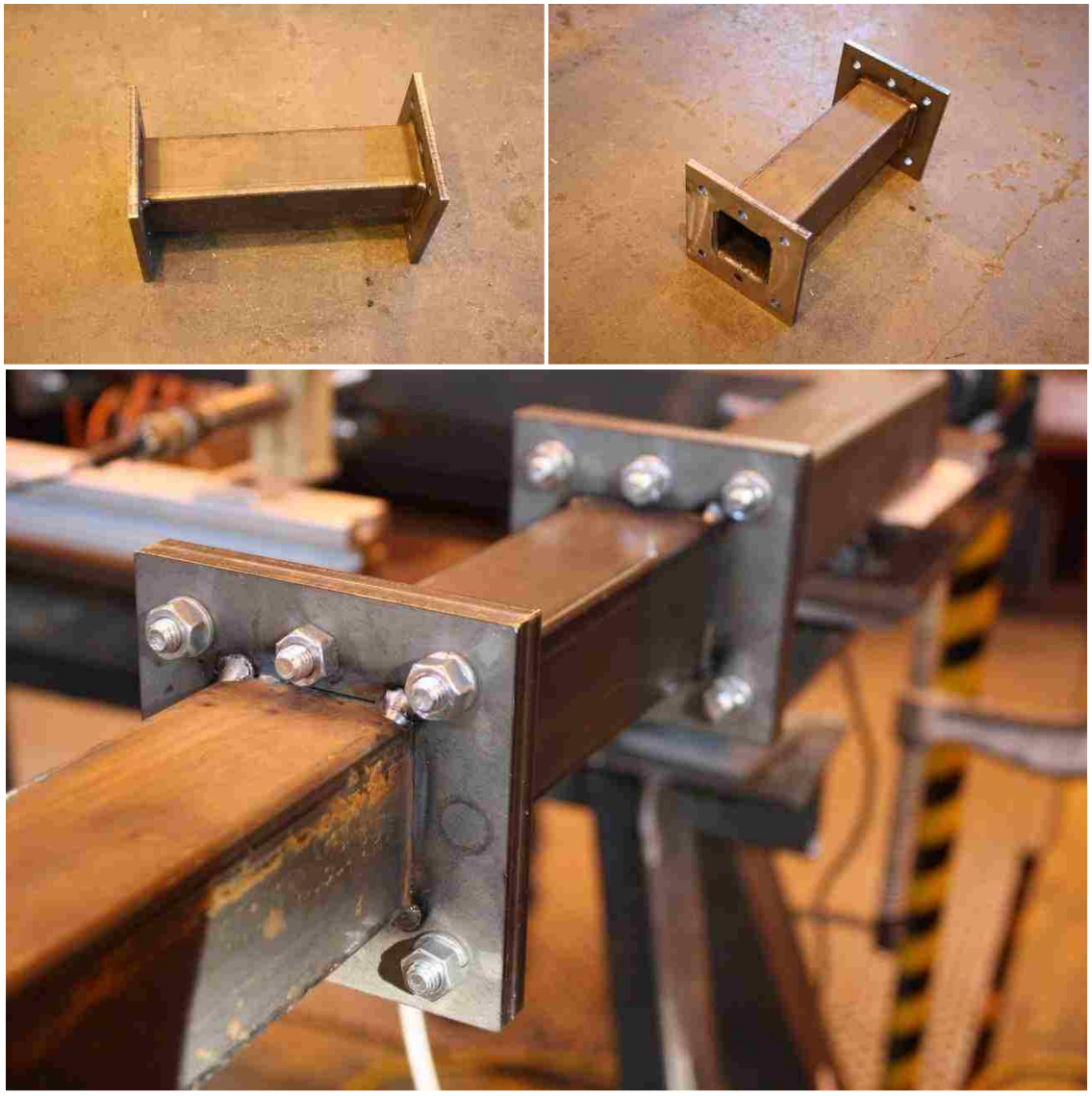

Figure 4.17. Views of member switchout for the experimental frame

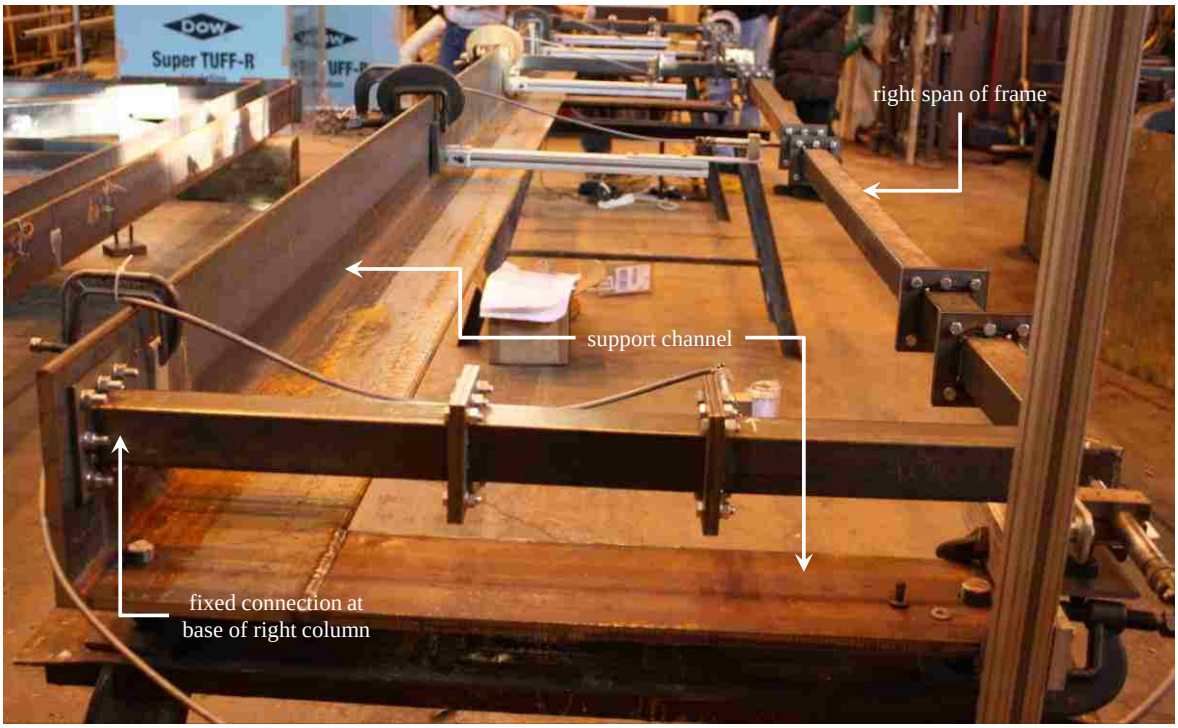

Figure 4.18. Angle support channel with frame cantilevered at base of columns

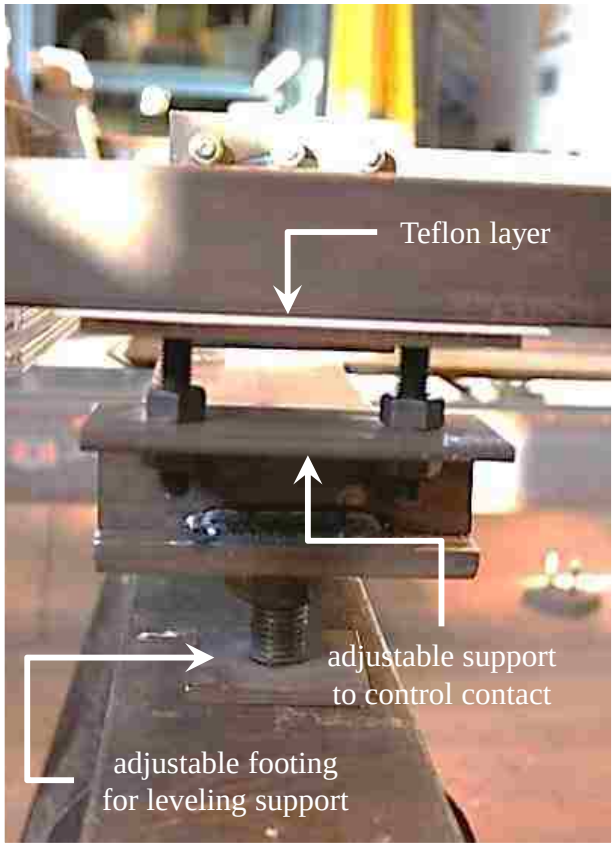

Figure 4.19. Adjustable support used to support the cantilevered end of the frame with Teflon layer facilitate roller support action

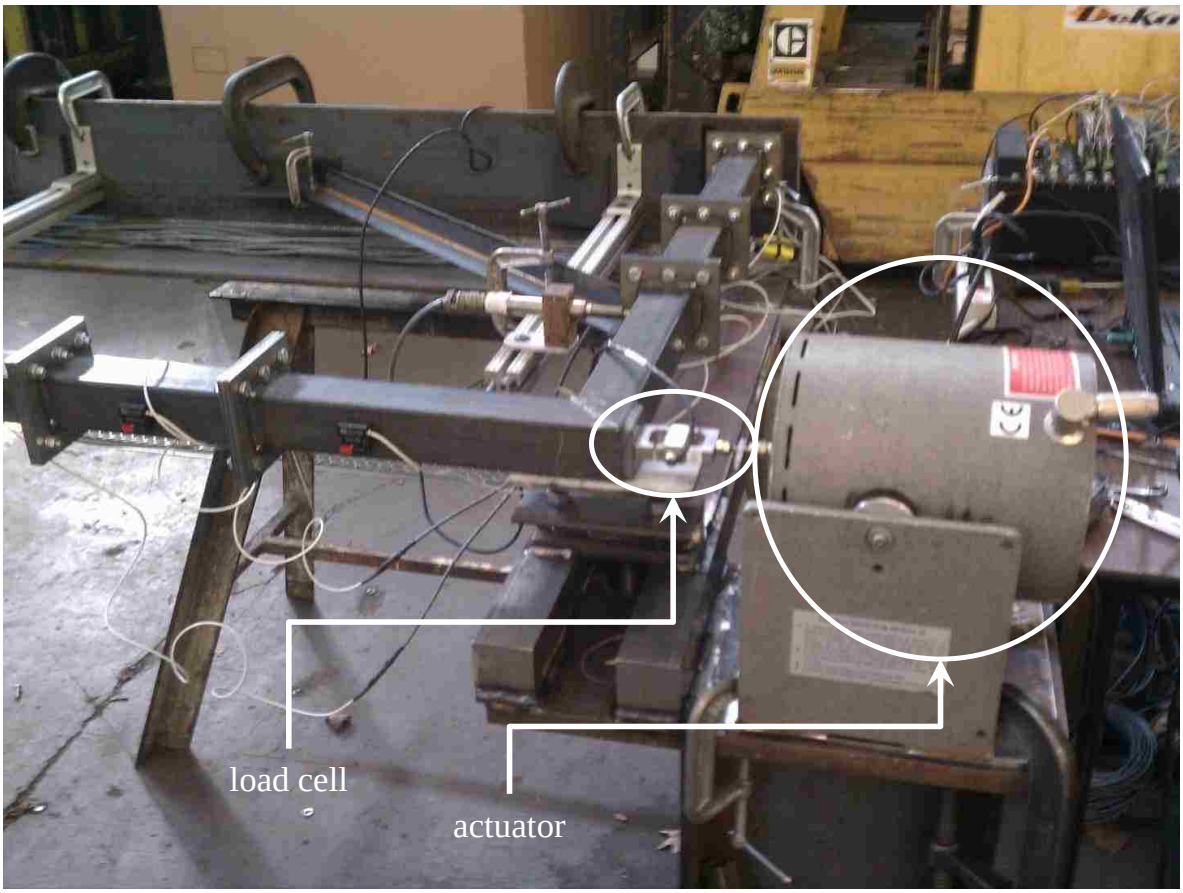

Figure 4.20. Experimental set-up with inline load cell and actuator at left joint

Figure 4.21. Silicon Designs 2210-002 wired accelerometer mounted on the frame

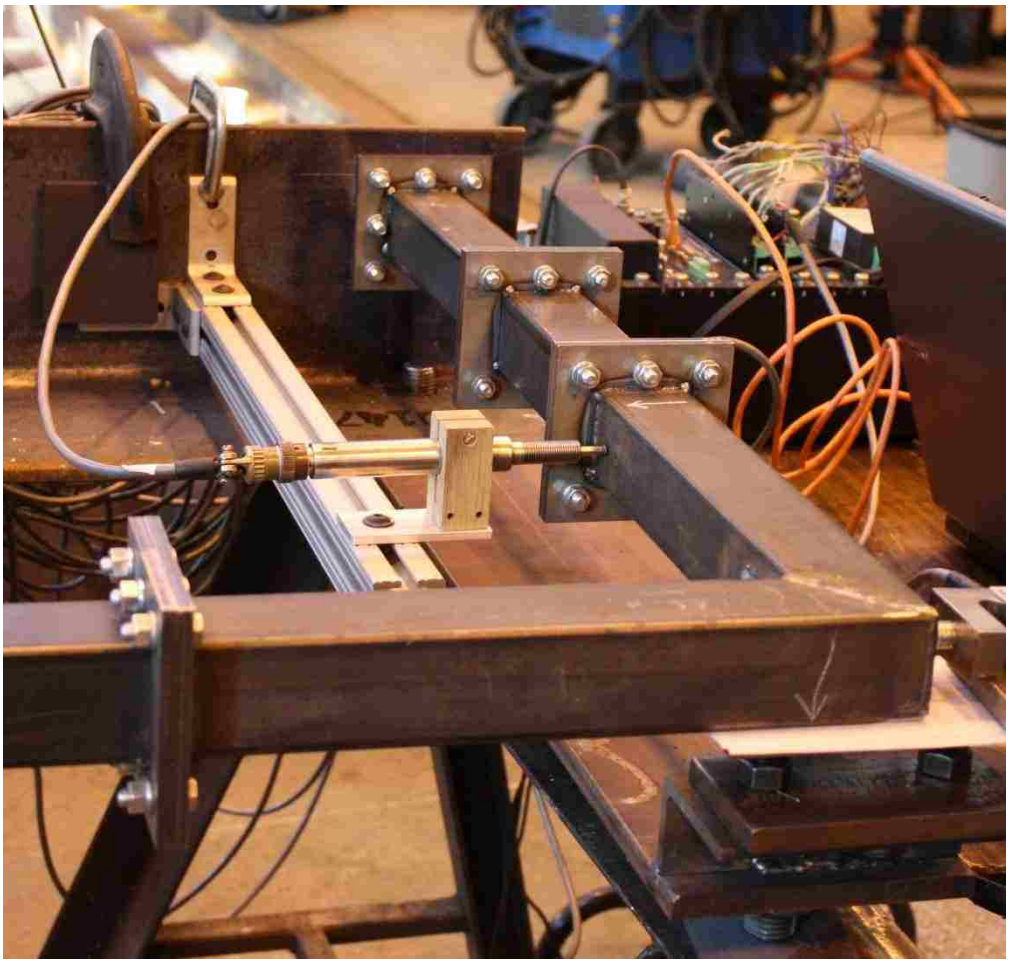

Figure 4.22. Macro Sensors GHSD 750-250 LVDT mounted at location 1 on the frame

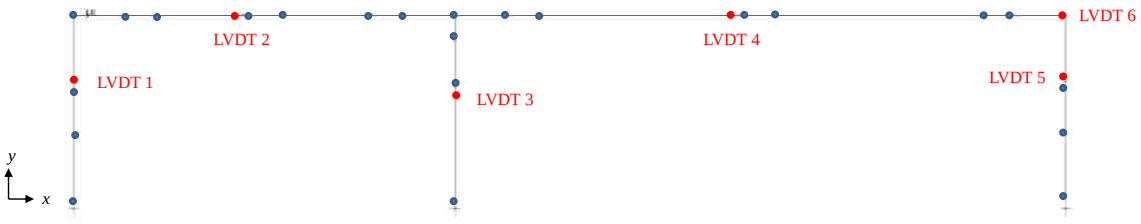

Figure 4.23. Simplified SAP2000 simulation with 29 nodes and 28 finite elements for static testing

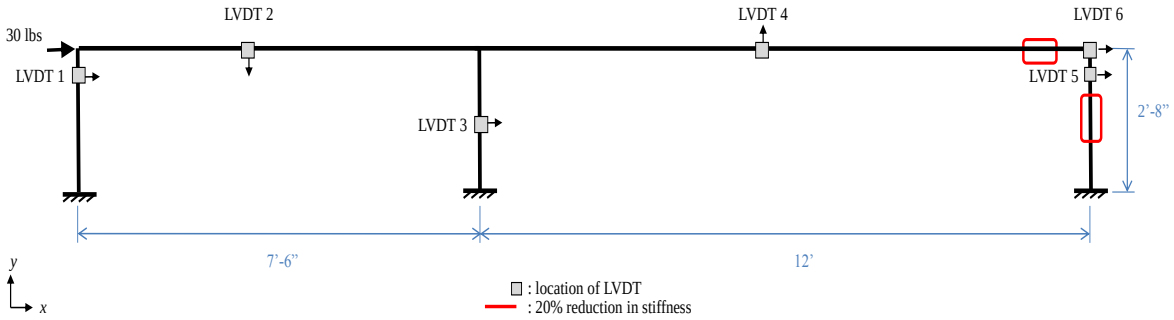

Figure 4.24. Static testing configuration with LVDT and damage locations

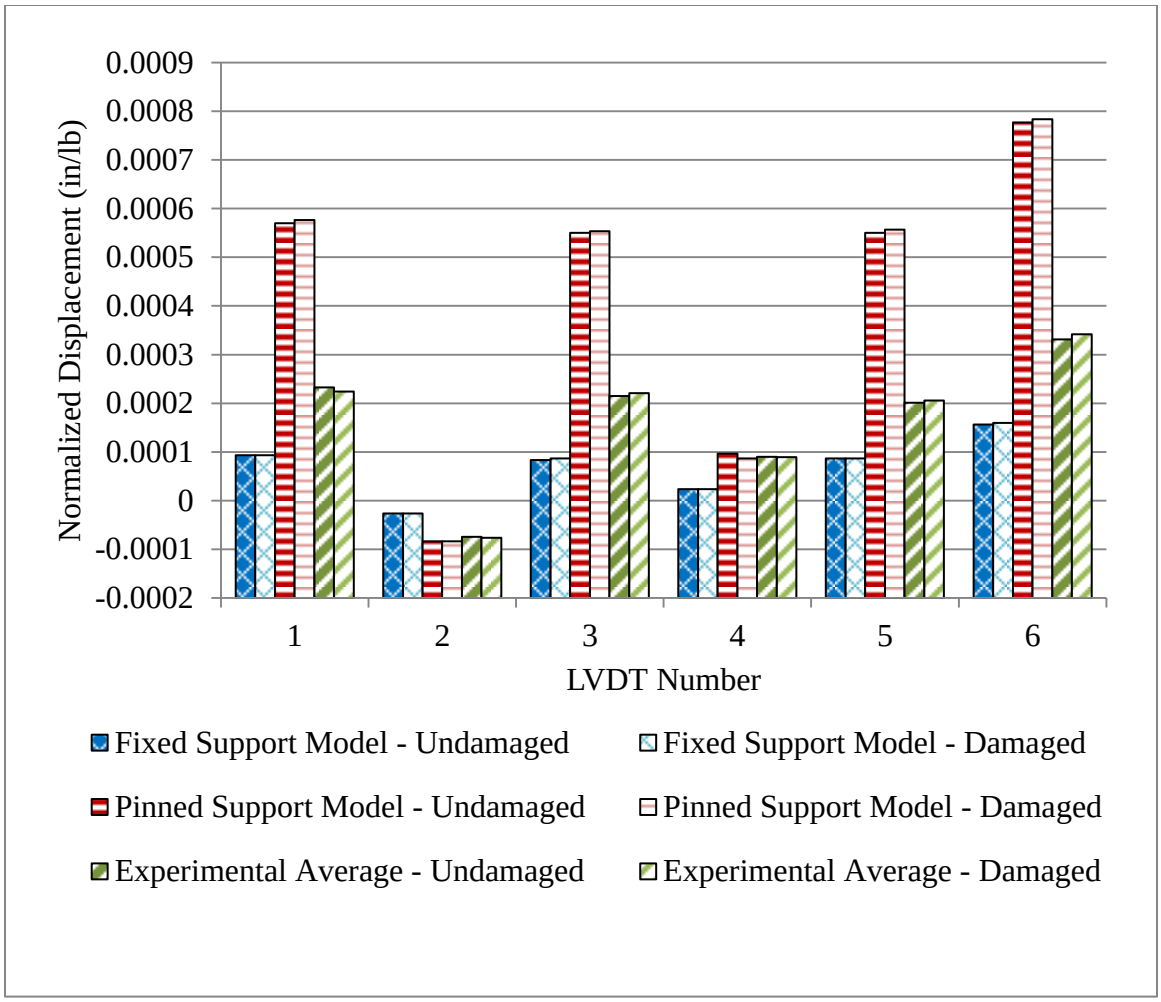

Figure 4.25. Comparison of experimental displacements to simulated displacements for undamaged and damaged cases

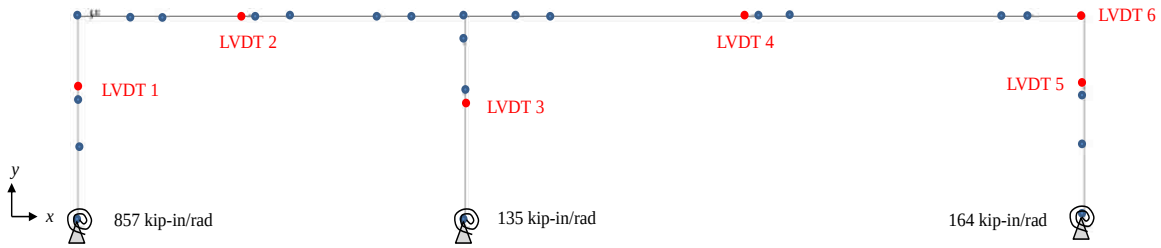

Figure 4.26. Updated SAP2000 model with rotational springs in place of fixed connections

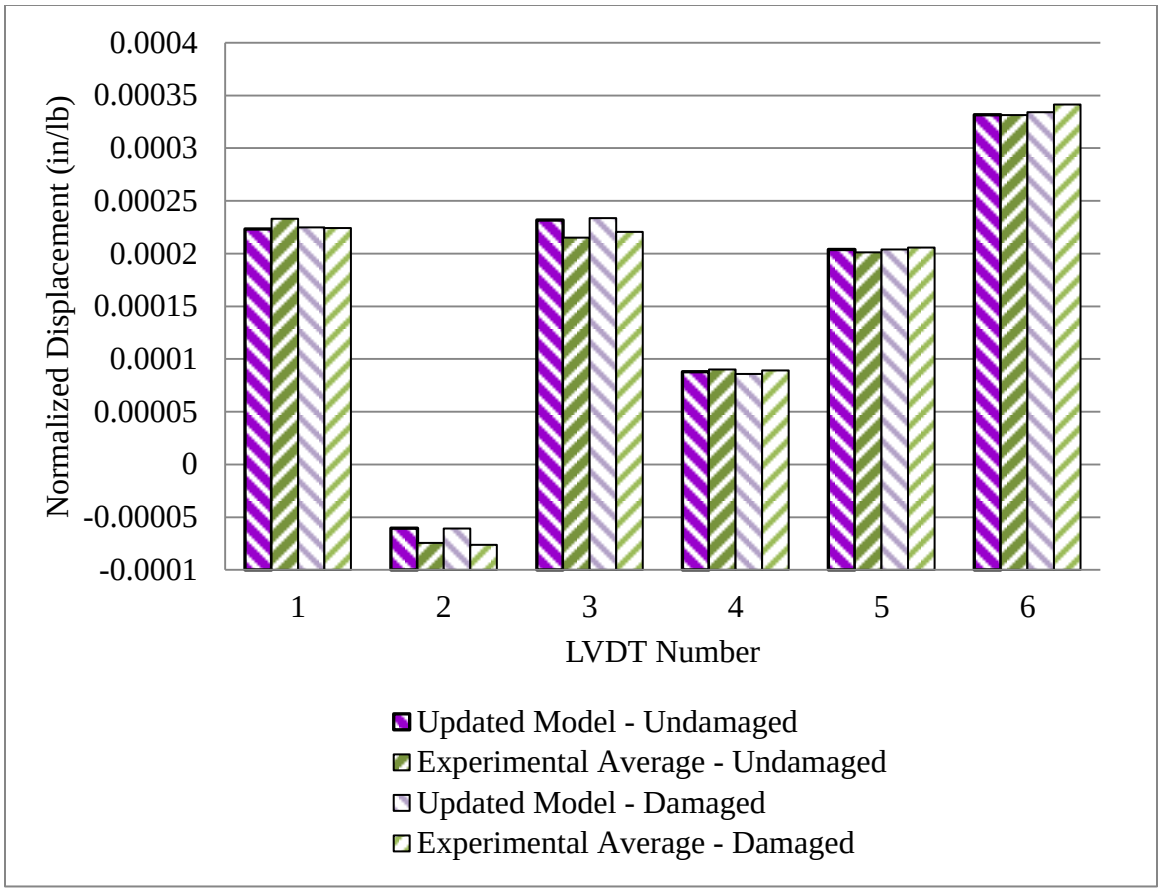

Figure 4.27. Comparison of updated simulated results to experimental displacements for the undamaged and damaged cases

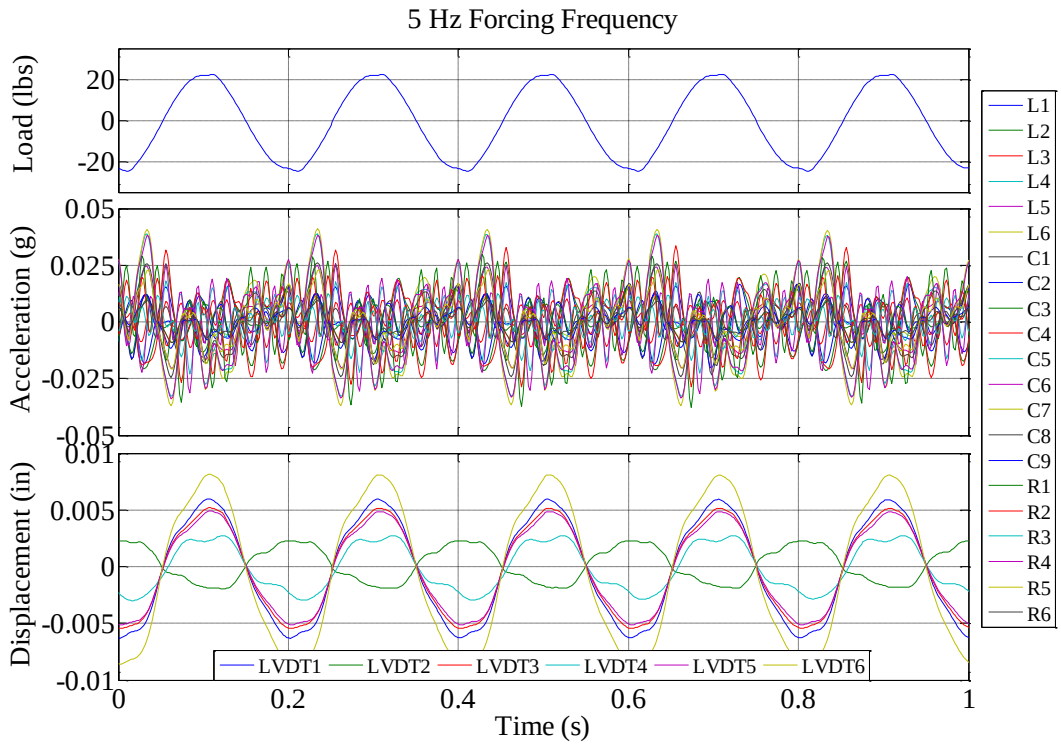

Figure 4.28. Time histories for load, accelerations, and displacements at 5 Hz sine

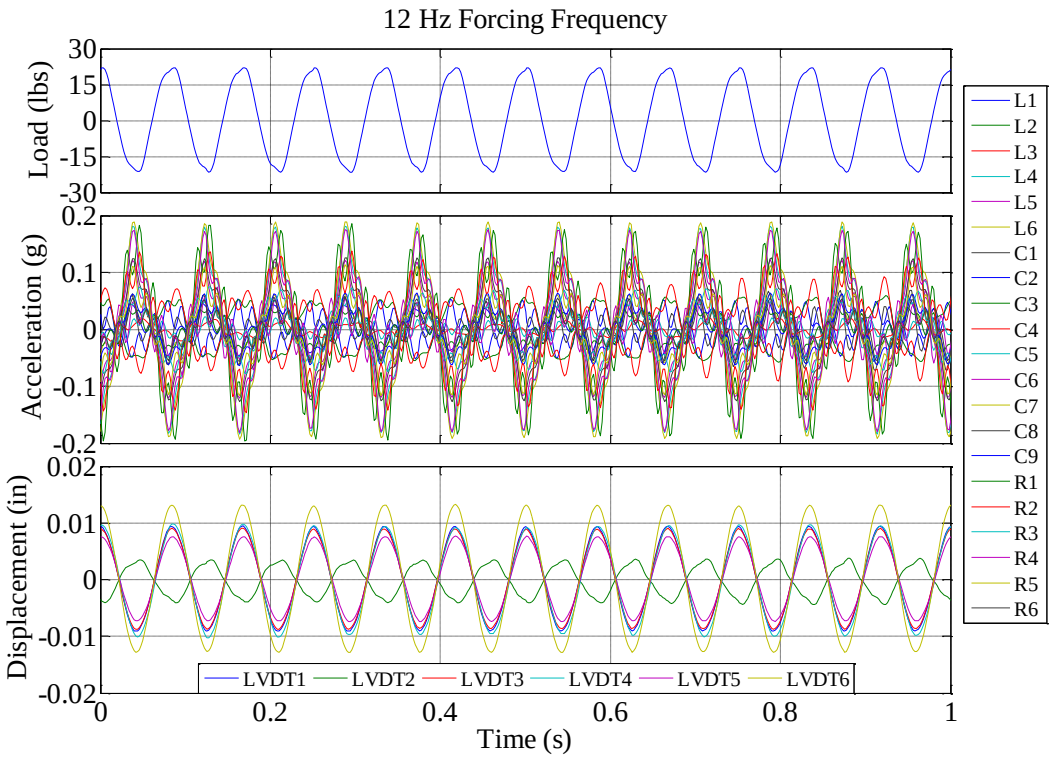

Figure 4.29. Time histories for load, accelerations, and displacements at 12 Hz sine

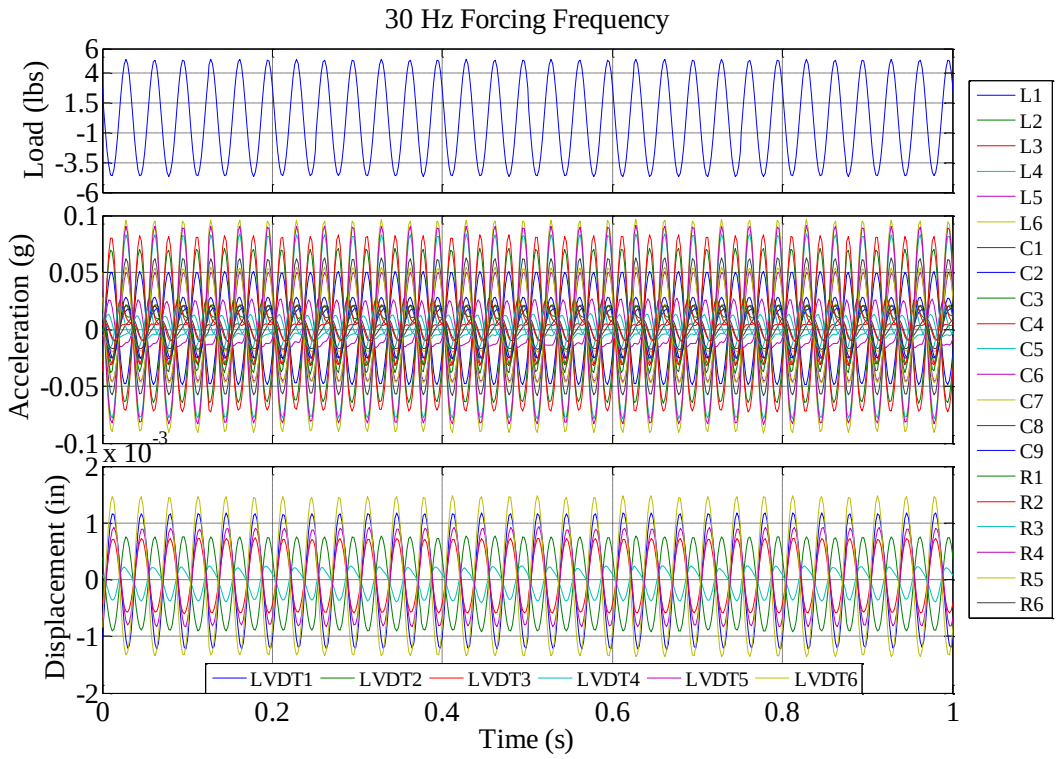

Figure 4.30. Time histories for load, accelerations, and displacements at 30 Hz sine

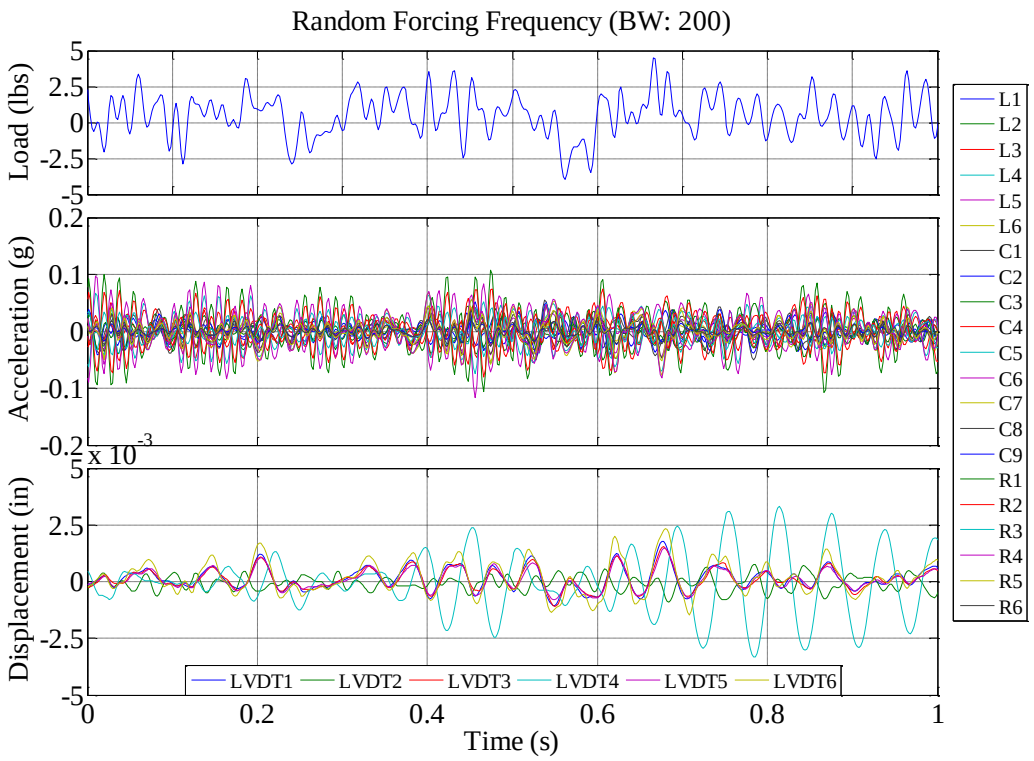

Figure 4.31. Time histories for load, accelerations, and displacements at random force

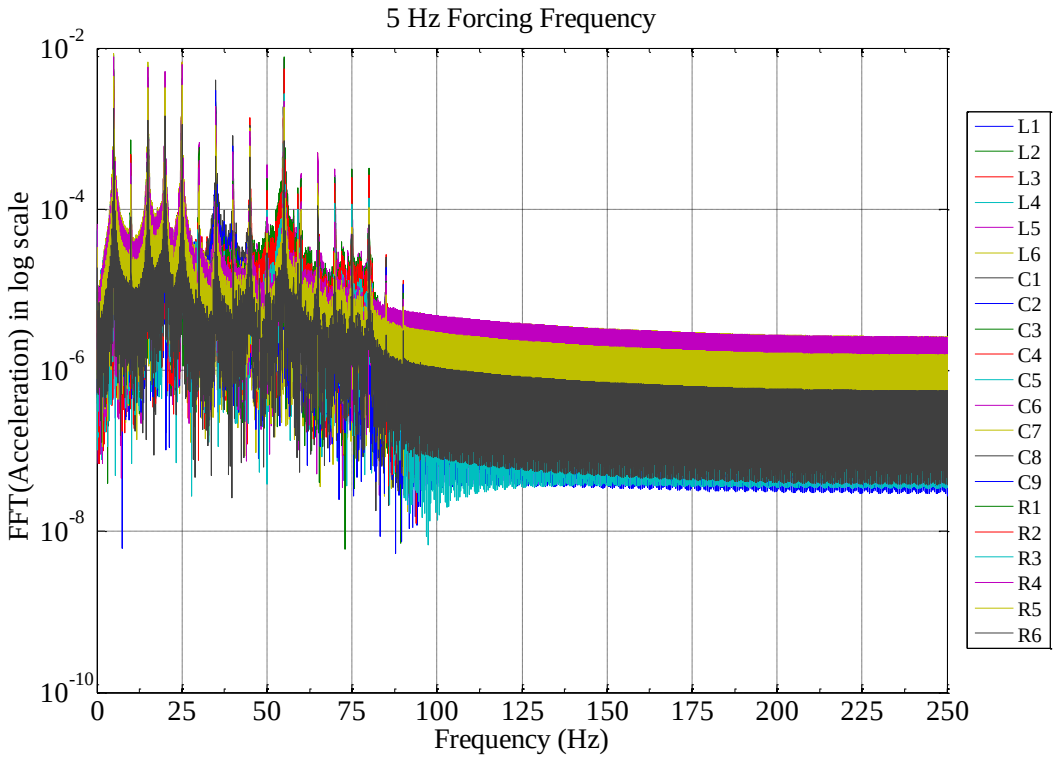

Figure 4.32. Power spectra of acceleration response for 5 Hz sine

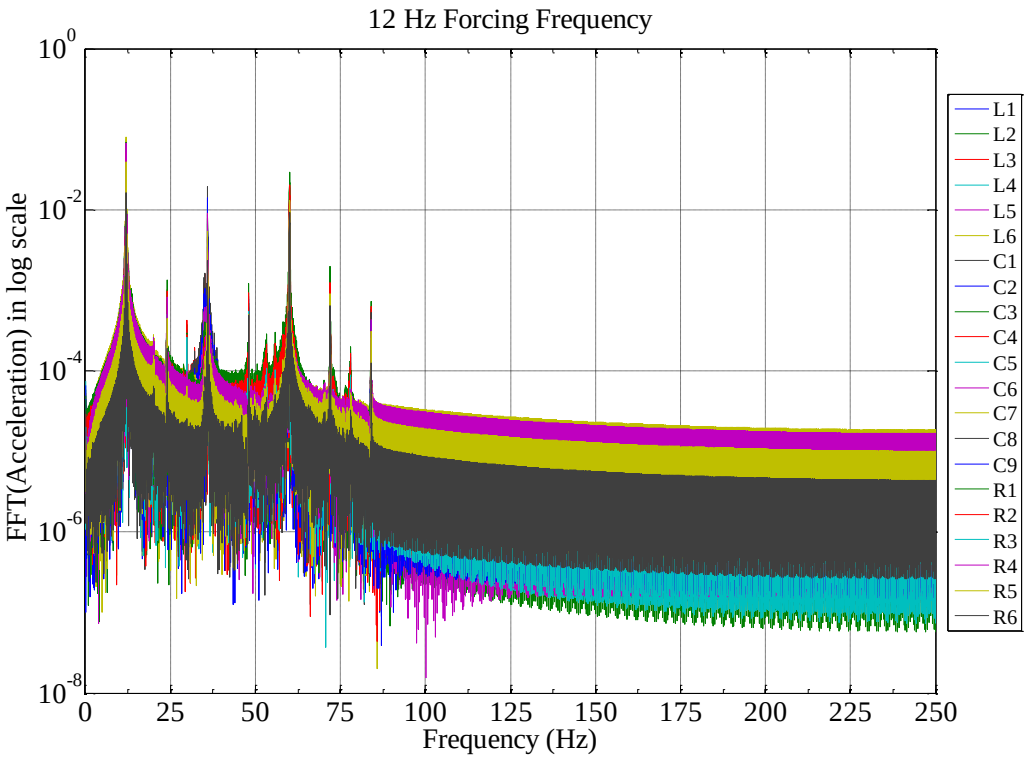

Figure 4.33. Power spectra of acceleration response for 12 Hz sine

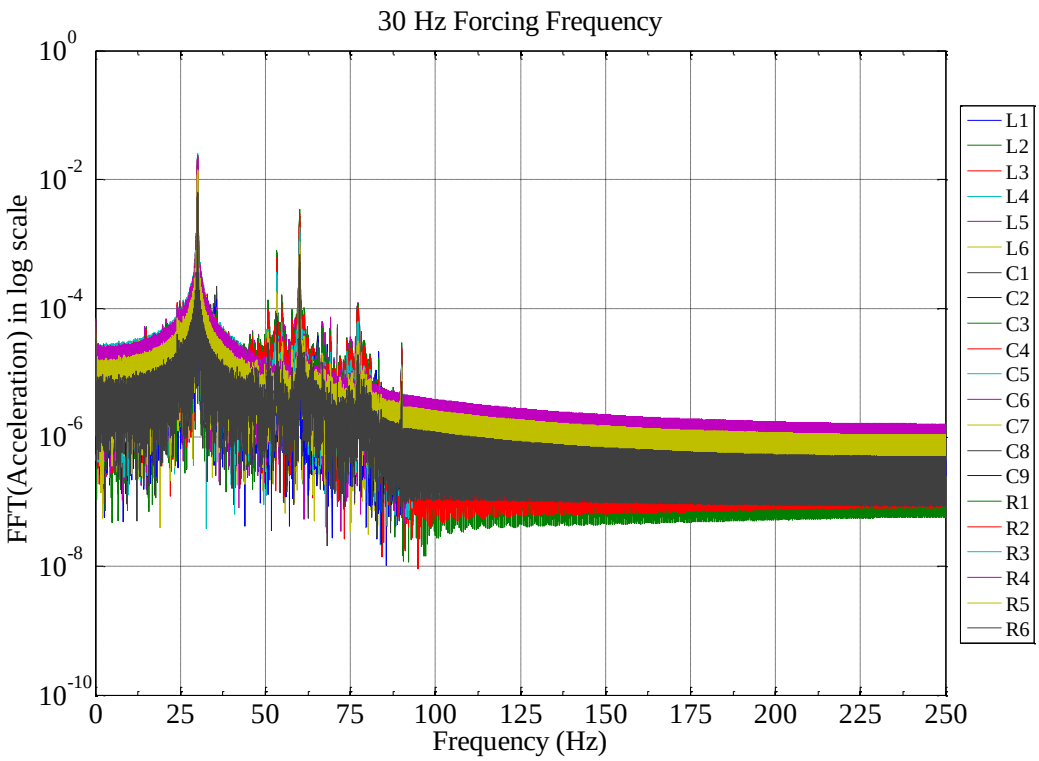

Figure 4.34. Power spectra of acceleration response for 30 Hz sine

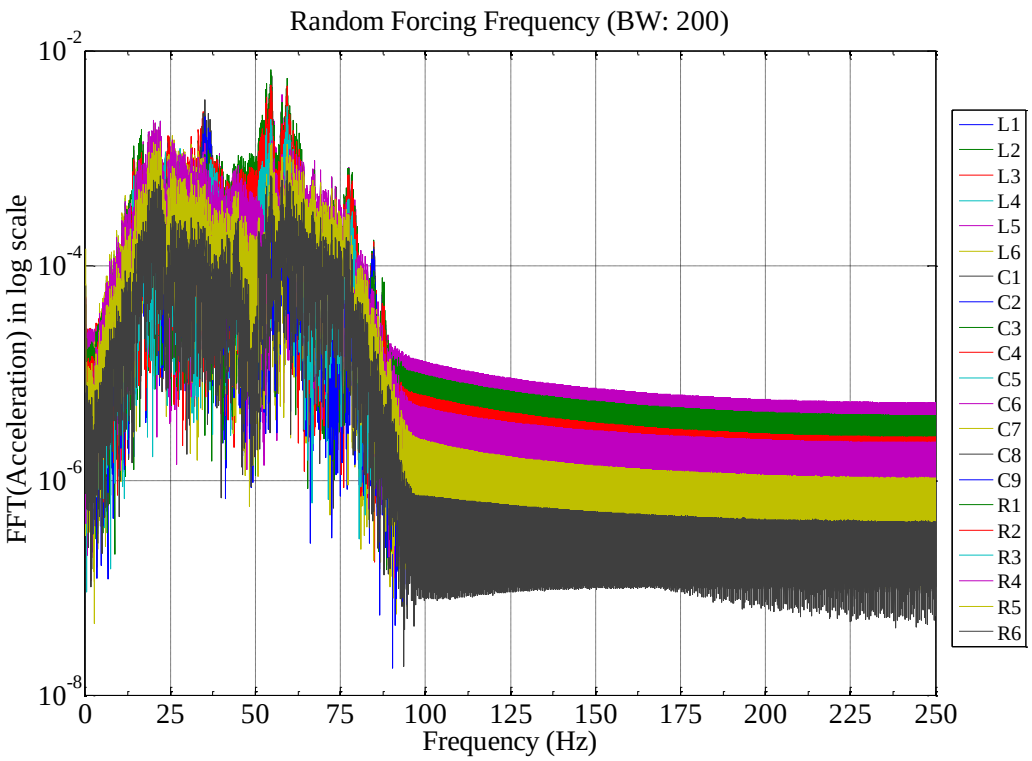

Figure 4.35. Power spectra of acceleration response for random force

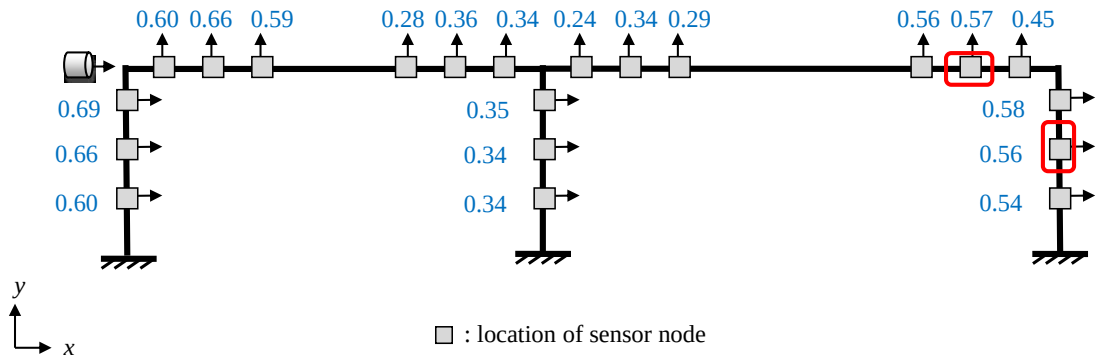

Figure 4.36. Average *EA* values for 5 Hz sine

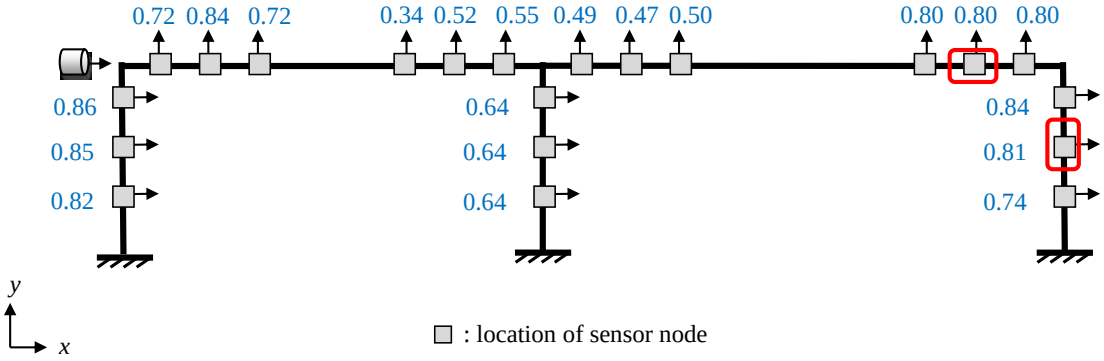

Figure 4.37. Average *EA* values for 12 Hz sine

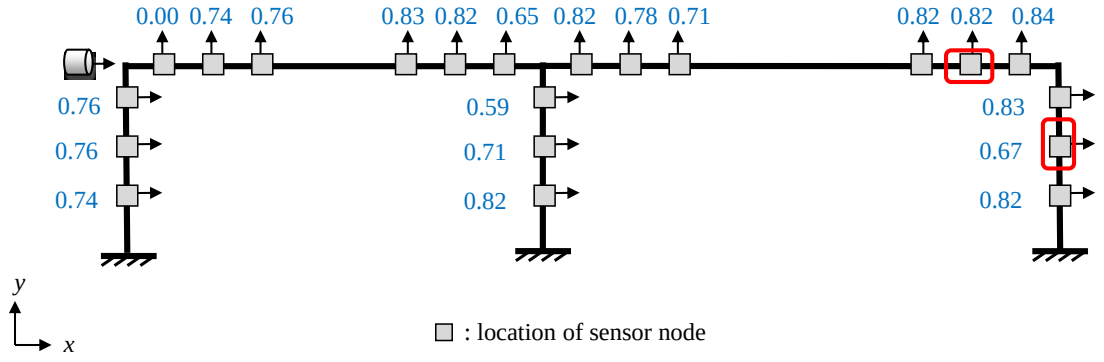

Figure 4.38. Average *EA* values for 30 Hz sine

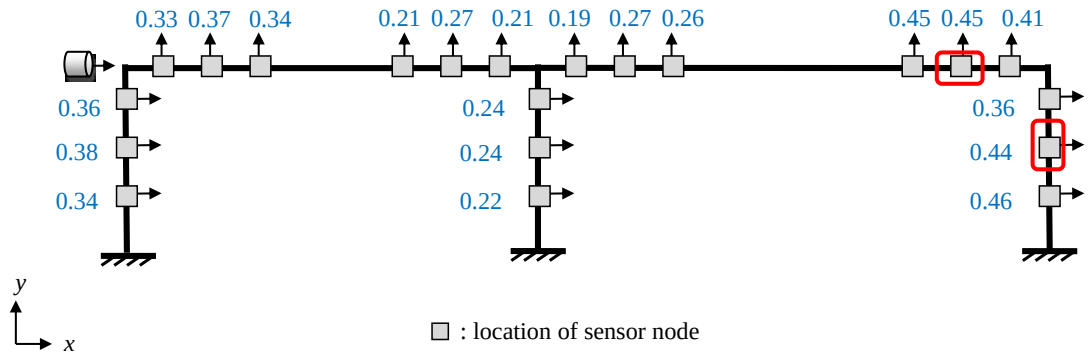

Figure 4.39. Average *EA* values for random force

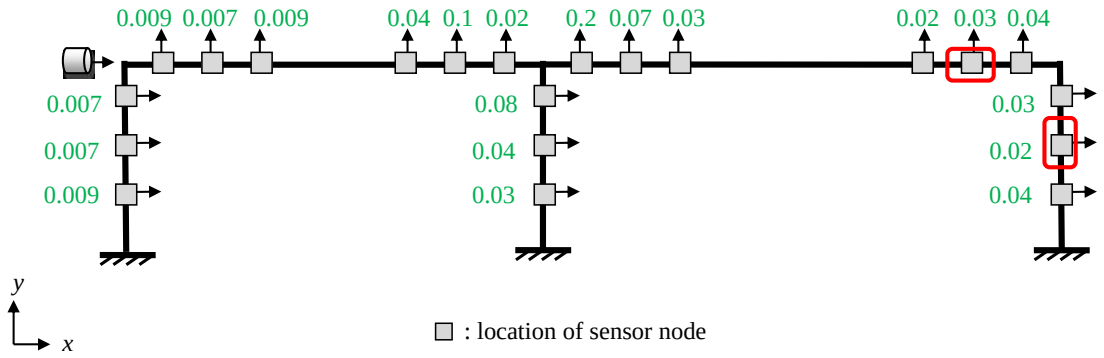

Figure 4.40. Average γ values for 5 Hz sine

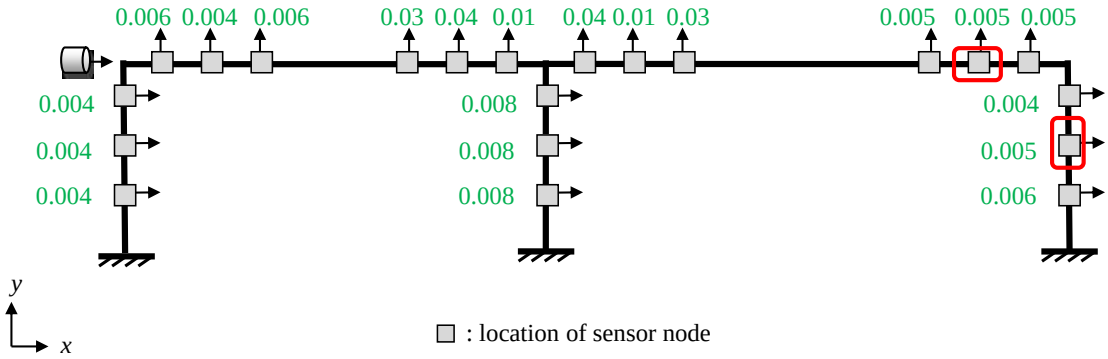

Figure 4.41. Average γ values for 12 Hz sine

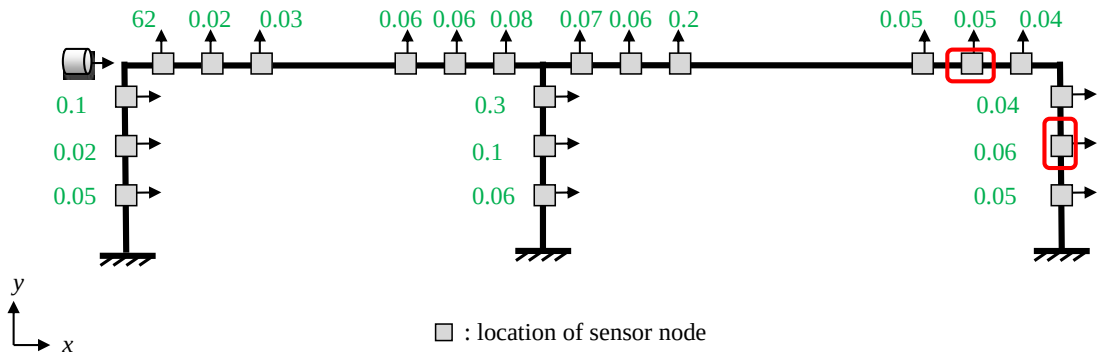

Figure 4.42. Average γ values for 30 Hz sine

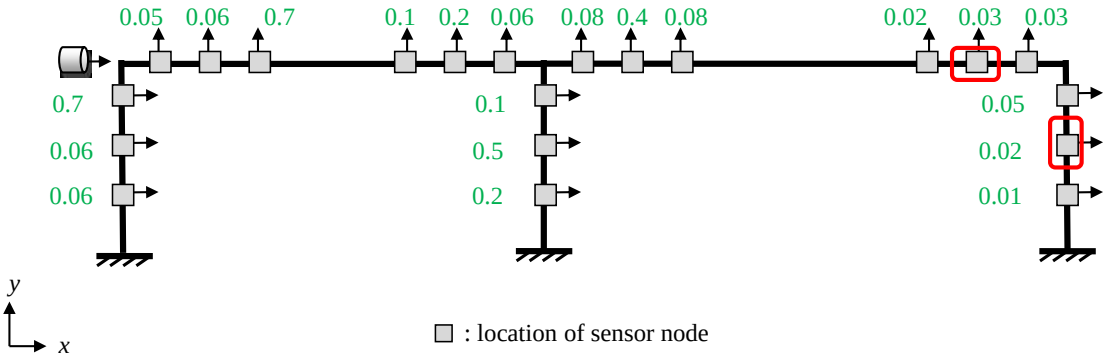

Figure 4.43. Average γ values for random force

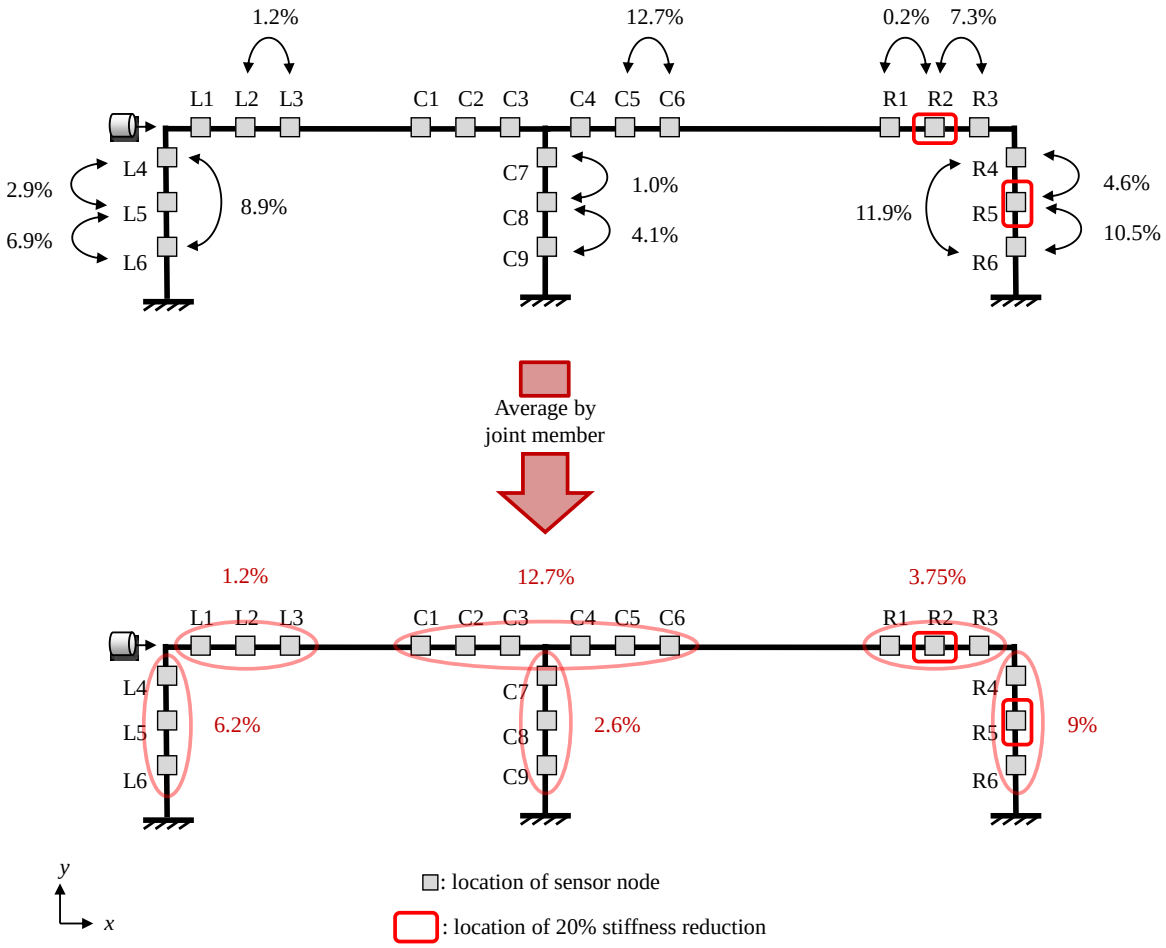

Figure 4.44. Relative changes observed for coefficients with high accuracies in 12 Hz data

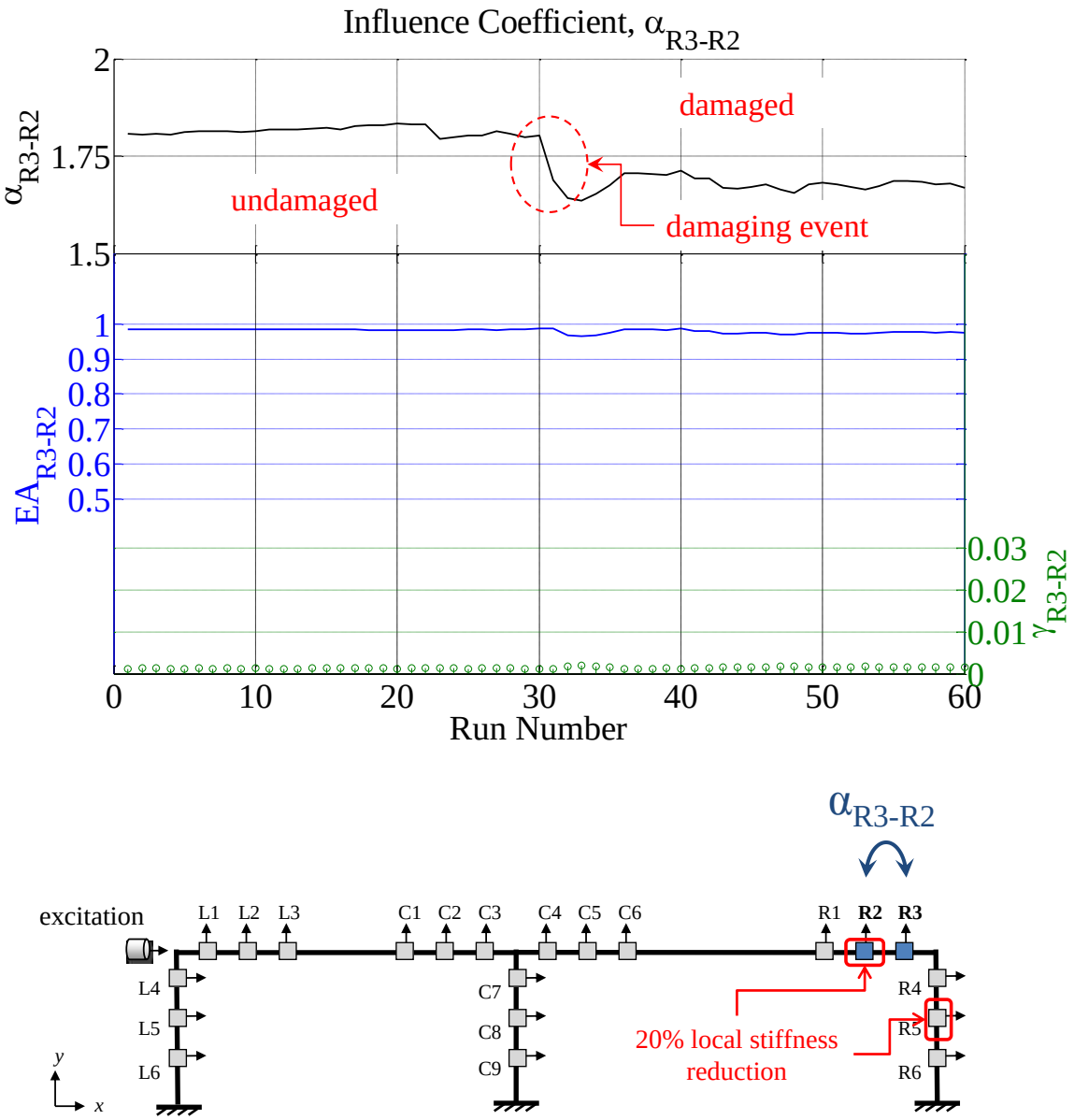

Figure 4.45. *α*, *EA*, and *γ* results for $\alpha_{R3\text{-}R2}$

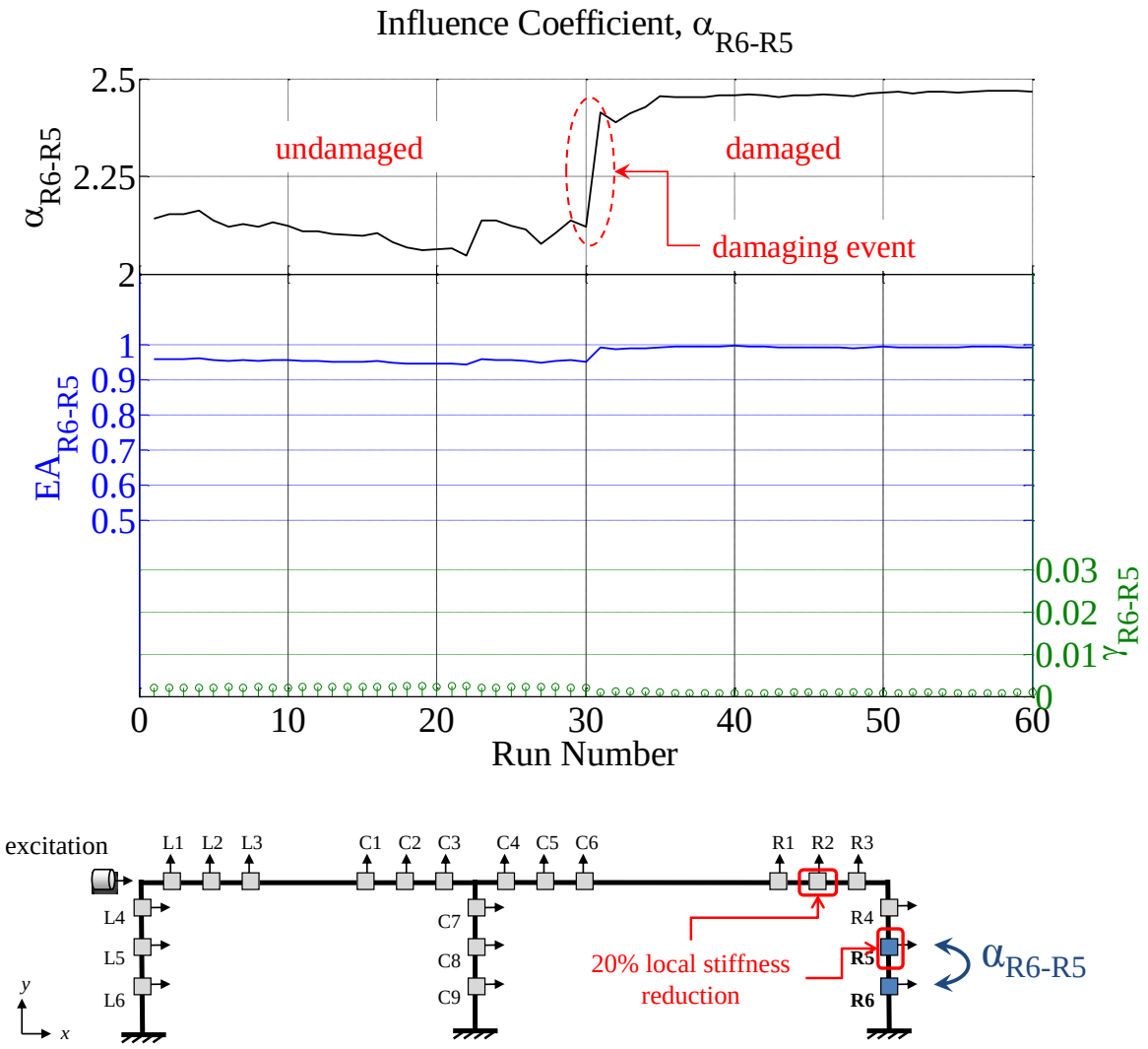

Figure 4.46. *α*, *EA*, and *γ* results for $\alpha_{R6\text{-}R5}$

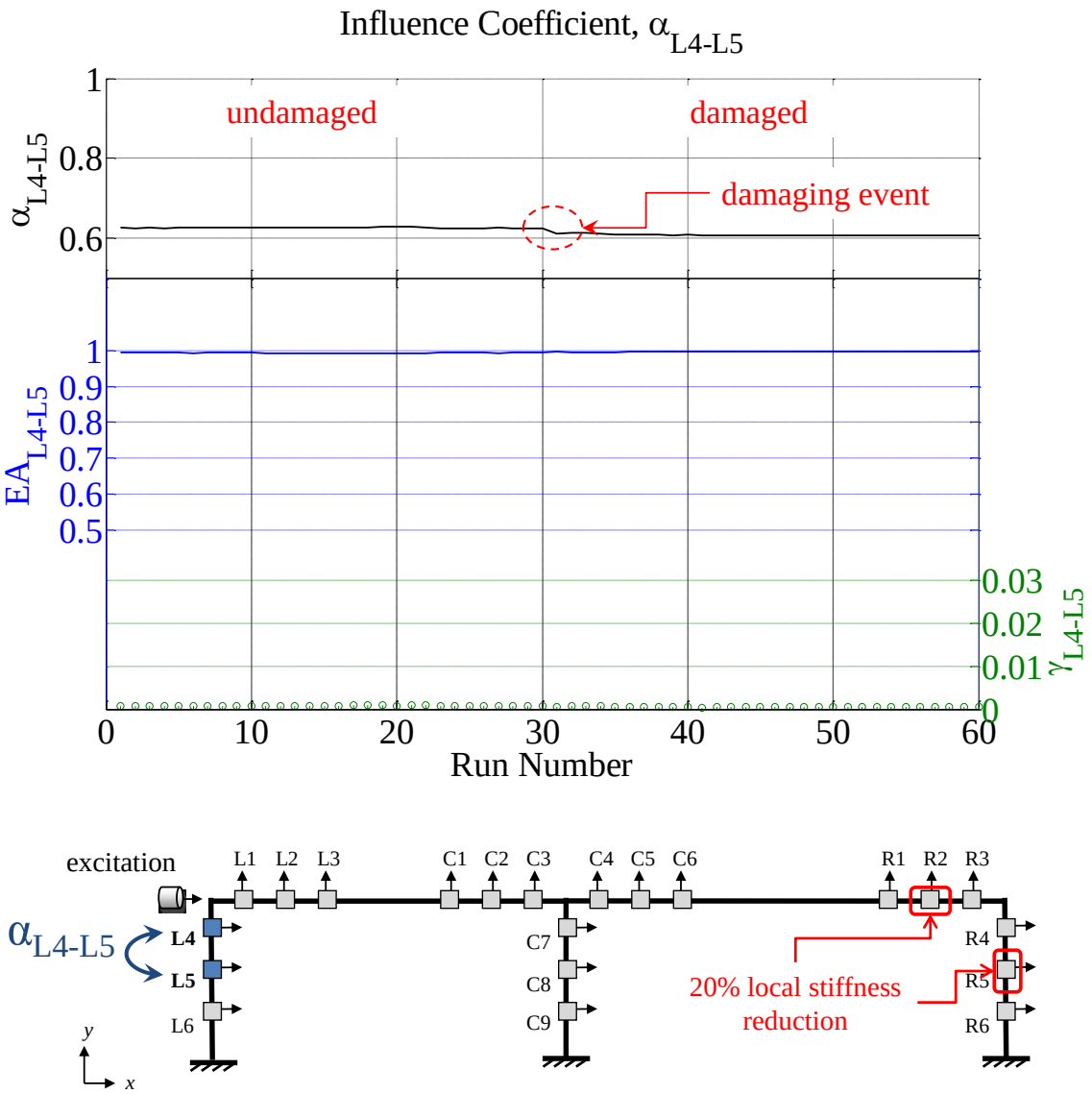

Figure 4.47. *α*, *EA*, and *γ* results for $\alpha_{L4\text{-}L5}$

Chapter 5 Damage Detection of a Large-Scale Moment Connection with Strain Gauges

5.1 Introduction

While Chapters 3 and 4 present examples of applications validating the performance of the proposed localized damage detection method, these models have idealized the damage; a portion of the beam is replaced with a member of known characteristics. Therefore, there is a need to verify this method for full-scale structures exhibiting damage scenarios that are more varied in location and severity. Moreover, it is important to substantiate the use of other commonly used and affordable sensor types. In this case strain gauges are used, which also represent a different set of response parameters. In this chapter, the performance of the damage detection algorithm is evaluated for a large-scale steel moment connection constructed at the ATLSS Center at Lehigh University, which was being tested for use in an earthquake-prone structure. The test specimen was instrumented with strain gauges and cyclically loaded to failure. The strain responses were analyzed using the localized damage detection algorithm to identify the progression of damage.

5.2 Theory for Application to Strain Data

The local damage detection algorithm applied in this research was previously developed using the acceleration output of simulated and experimental structures in Chapters 3 and 4. However, this method is theoretically applicable for a structure's strain response as well.

Based on the principles of statics, the forces and moments at any point along a structure are linearly related to the applied load. Forces and moments directly translate to stress through the linear-elastic relations $\sigma = P/A$ and $\sigma = My/I_{zz}$, respectively. Furthermore, the constitutive stress-strain relation yields the strain at any point along the structure in terms of the applied load. If the strain at any two points, nodes *i* and *j*, can be defined in terms of the applied load, then these definitions can be reconfigured to yield the strain at node *i*, ϵ_i, in terms of the strain at node *j*, ϵ_j, as follows:

$$\epsilon_i(t) = \beta_{ij} + \alpha_{ij} \cdot \epsilon_j(t) + \varepsilon_{ij} \tag{5.1}$$

While a beam-column free body contains 9 possible DOFs, this number can be reduced similarly to the justifications presented for acceleration responses of a beam-column in Section 2.2. Under the assumption that there is one dominant load applied with all other loads negligible, only one other strain response is required to define the strain at any point along the structure. From each pair-wise linear regression relationship, an influence coefficient can be extracted. When damage occurs at a local point in the structure, the change in structural properties occurs as demonstrated by the progressively reduced stiffness, or slope, in the force-displacement plot of Figure 5.10.

These stiffness reductions reflect a change in the constitutive stress-strain relationship, which in turn will give different strain values for the same applied load. Ultimately, the pair-wise influence coefficient will also change from this damage, if the strain at node *i* changes differentially compared to the strain at node *j*. By observing the pattern of changes in a network of pair-wise influence coefficients, these parameters effectively serve as a "damage indicator."

5.3 Experimental Prototype

A large-scale steel earthquake moment connection design was cyclically tested to failure for performance verification at the ATLSS Center at Lehigh University. While multiple variations of the design were tested for the client, four of the test specimens were instrumented with additional strain gauges. One of these datasets, referred to here as Test A, was use for application of the localized damage detection algorithm.

5.3.1 Experimental Test Setup

Because the design is to be implemented in a California hospital, it is subject to the seismic qualification requirements as set forth by the Office of Statewide Planning and Development (OSHPD) (Hodgson and Ricles 2010). According to these requirements, the specimen must sustain at least two full cycles of an inelastic drift angle of 0.03 radians and at least two full cycles of an interstory drift angle of 0.04 or more radians without failure (Hodgson and Ricles 2010). Progressive drift sequences were applied using parallel hydraulic actuators at the free end of the beam, with the columns fixed to the strong wall and the strong floor, shown in Figure 5.1. The drift sequence is summarized in Table 5.1.

Figure 5.2 shows the general configuration of the test specimen, as well as the instrumentation plan used for the application of the damage detection algorithm. The specimen was instrumented with five strain gauges, with gauges 1 and 2 at third points on the top flange of the beam, gauge 3 directly below gauge 1 on the bottom flange if the beam, and gauges 4 and 5 on the outside flange at the midpoint of each column.

5.3.2 Damage Results of Experiments

The progression and location of damage was documented throughout testing for the subassembly. Notes were taken after the completion of each stage in the drift sequence. The proposed localized damage detection method was then applied to the data, and the results were compared to the observed behavior to assess the method.

5.3.2.1 Test A Damage Observations

The Test A damage notes are summarized in Table 5.2. Each set of drift cycles was designated with a respective damage classification starting with Damage Class 0 for the undamaged cycles through Damage Class 9 when failure occurred. Additionally, photos were taken during the test to further document the damage. Figure 5.3 through Figure 5.9 demonstrate the damage incurred in each damage class from Damage Class 3 to failure as described in the damage notes.

5.4 Application of Localized Damage Detection Algorithm

The algorithm was applied using data from the Test A specimen. This data was used to determine the best approach for implementing the algorithm with this particular type of data. The resulting approaches can later be used for processing other similar datasets.

5.4.1.1 Pre-processing of Strain Data

Prior to processing the data through the algorithm, the strain responses were considered in comparison to one another as well as versus time. Figure 5.11 presents an example of a strain versus strain plot for the two gauges on the column, while Figure 5.12 shows a

strain versus strain plot for two of the gauges on the beam. Figure 5.11 shows a case in which the relationship between the two responses remains mostly linear throughout all cycles with small changes in slope over time. Figure 5.12, however, shows the result of excessive yielding. A structure exhibits linear-elastic behavior prior to a damaging event, experiences nonlinear behavior during an extreme event, and then returns to an altered linear-elastic state following the damaging event. Portions of the data which best exhibited a linear relationship were used in implementation of the algorithm in order to minimize the error term in the regression model, thus, increasing the accuracy of the parameters.

Figure 5.13 shows the time histories of the strain responses and the applied load. It should be noted that, at the beginning of this plot, the cycles within the data are relatively uniform, but become less uniform as the testing continues, along with the increase of damage. Also, it can be seen that there are intermittent flat portions of the strain data, corresponding to a constantly held load at both the peaks and valleys of each load cycle. Initially, the influence coefficients were calculated for the entire data set. This was achieved by calculating influence coefficients for an overlapping, moving window of 50 samples. The resulting coefficients are shown in Figure 5.14 for a selection of influence coefficients. Based on these preliminary results, it is clear that using the entirety of the data set produces results with high noise and error. This is evidenced by the large variations in the coefficient value, even prior to damage when the coefficient value should be the most consistent. Therefore, only certain portions of the data should be used for the algorithm. In order to determine which sections of the data were best for use in the algorithm, two types of sections were considered: (1) the loading and unloading

portions of strain data only and (2) the holding (or constant load) portions of the strain data only.

For these scenarios, each loading or holding section was considered as a separate test, with one influence coefficient value calculated for each. The resulting values are shown for $\alpha_{1\text{-}2}$ in Figure 5.15 and Figure 5.16, respectively. By inspection of these plots, the holding data shows significantly more noise, which makes it difficult to distinguish between the undamaged and damaged coefficients. However, the loading/unloading data shows a relatively constant value for the influence coefficient, until later sections in which damage is occurring. This distinct change allows for damage detection; therefore, the loading and unloading sections were used for the remainder of the analysis.

An explanation for the larger amount of noise in the holding data is that the hydraulic actuators vary as they hold a constant load, which can be seen in the data at the beginning of the test before the first load was applied, shown in Figure 5.17. However, with an increasing or decreasing load the data appears much smoother and more consistent.

Furthermore, the loading and unloading portions of the data were trimmed according to the corresponding applied load, so as to only include strains due to loads within the ± 200 kip range, as demonstrated in Figure 5.18. This cutoff was chosen because 200 kips is the maximum load for the first drift in which the structure remained undamaged and purely linear-elastic. Considering strains within this range attempts to eliminate nonlinear behavior, which occurs with extreme loading. Therefore, this ensures that only strains from before and after the damaging events are used.

While the results in loading/unloading plot were less noisy, there were still large variations above and below the baseline value. This is inconsistent with the results found in the previous two applications, in which the coefficient drifts monotonically to a larger or smaller value with the onset of damage. There are two likely reasons for this discrepancy. Firstly, the damage in the previous applications was identical throughout all tests, whereas the damage in the current structure is varied and unknown. Therefore, the coefficient relationship may be different depending on what portion of the structure is damaged, say the top of the beam versus the bottom of the beam. The second reason relates to the first; there are four types of loading: downward loading (DL), downward unloading (DU), upward loading (UL), and upward unloading (UU). For example, if there is a crack in the top of the beam, when the beam is loaded downward, this crack will open further showing more damage. However, when the beam is loaded upward, this same crack will likely close and the structure will see less asymmetry. Therefore, the loading and unloading sections were further isolated to their loading types, resulting in four separate sets of influence coefficients for each pair. Figure 5.19 presents a plot of one of the coefficients after data was separated according to loading type. From this plot it can be seen that the coefficients follow a more consistent pattern of deviation from the baseline value as damage progresses.

5.4.1.2 Damage Detecting Influence Coefficients

After preliminary processing of the data was complete, holding and loading sections were sorted into the four separate loading conditions and processed through the algorithm. The damage detection algorithm could then be assessed by comparing each of the resulting

four sets of data to the observed structural deterioration over time. Figure 5.20 contains α, EA, and γ for all four loading conditions. From this plot, it can be seen that all four loading conditions show accuracy values of 1.0 and error terms close to null. These values were consistent for all estimated nodal pairs, meaning that all pairs should be reliable indicators. These values are much better than those observed in Chapters 3 and 4 for the acceleration response data. This is reasonable because strain is the double integration of acceleration, causing a smoothing effect; thus, reducing error.

For all four sets, the baseline is set by the coefficient values estimated in Damage Class 0, containing cycles from the first two drift angles. Figure 5.21 shows one of the coefficients, $\alpha_{2\text{-}4}$ plotted for the upward unloading sections according to progressive damage class. This plot demonstrates how the coefficients progressively deviate from the initial baseline value with each increasing damage state. However, the values do not begin decisively diverging from the baseline values until Damage Class 6. Inspection of the load-displacement plot separated by damage classes lends an explanation. In this plot, shown in Figure 5.22, it can be seen that, while yielding occurs as early as Damage Class 1, an actual loss of strength does not appear until Damage Class 6. Moreover, according to the damage notes presented in

Table 5.2 this also corresponds to the formation of a plastic hinge in the beam. In order to quantify these deviations from damage class to damage class, relative changes are considered. Each damaged class is referenced back to the baseline values. These values are presented and assessed hereafter.

5.4.1.2.1 Downward Loading

The first loading condition to be considered is the downward loading (DL) in which the free end of the beam is being pushed downward. The percent change values for each DL damage class compared to the baseline DL values are shown for select node pairs in Figure 5.23 through Figure 5.31. It can be seen in Damage Classes 1 and 2 that all of the percent change values are less than 3%, at times as low as 0%. In fact, only one coefficient, α_{1-4} in Damage Class 2, exceeds 2%. Considering the damage described in Table 5.2, these negligible changes are consistent with the mild yielding observed on the bottom cover plate and the beam flange.

Damage Classes 3 and 4 see slight increases in change, however, all values still remain 5%. In Damage Class 3, when yielding was seen in the bottom cover plate, in the top and botton beam flanges, and at $1/5^{th}$ locations of the web, more notable changes (2.4% - 3.3% compared to 0.3% - 0.9%) were seen in α_{1-4}, α_{2-4}, and α_{4-5}, all of which have nodes located on either sides of the damage. However, not all of the pairs with nodes on opposing sides of damage showed a change. This assymmetry in coefficients is likely due to the assymetry seen in the damage, with more yielding on the bottom portion of the beam. Damage Class 4 changes became more symmetric, consistent with the addition of damage to the top cover plate as well as increases in preexisting yielding.

Damage Class 5 saw drastic jumps in percent change with up to 53%. During this drift significant damage was incurred with considerable beam flange and web yielding, extreme yielding of the bottom cover plate, and separation of the top cover plate from the beam. The largest changes are that of α_{2-4}, α_{2-5}, and α_{1-2}. The first two of these coefficients correspond to beam-column pairs with nodes on either side of damage due to

the heavily concentrated beam damage. Additionally, the third coefficient is between nodes on the same side of the beam, making these strains more sensitive to the same damage. On the other hand, coefficient $\alpha_{4\text{-}5}$, a column-column nodal pair, showed a negligible change of 1.2%. This small change can be accounted to the fact that all notable damage is isolated to the beam, with neither column node seeing the effects.

During Damage Class 6 severe damage was incurred, including beam web buckling, top and bottom beam flange buckling, bottom cover plate separation from the beam, and the complete formation of a plastic hinge in the beam. However, from Damage Class 5 to Damage Class, there was a decrease in the percent changes from a range of 9% - 53% to a range of 1% - 37%. The likely cause of this is the formation of the plastic hinge, which resulted in out-of-plane bending of the beam. Out-of-plane bending changes the relationship between nodes and could make it appear closer to the original relationship than the relationship seen in Damage Class 5. Additionally, a small crack in the side plate-to-column weld was reflected in $\alpha_{4\text{-}5}$ with an almost tripled 3.4% change.

Damage Class 7 shows a continued decrease in percent changes to less than 10%; however, the noticeable percent changes are concentrated at nodal pairs surrounding the observed beam damage. The damage observed consists of severe buckling of the beam flanges and web as well as increased out-of-plane beam bending. Again, increased out of plane bending is the most likely cause for the decrease in change.

In the final two damage classes, 8 and 9, the top cover plate-to-beam weld crack, which developed in Damage Class 5, propagated into the beam flange and eventually halfway down the web. Both sets of relative changes show increases in the beam-beam and beam-column coefficients. Despite continued out-of-plane bending, this increase is

seen because the severe cracking in the beam becomes the more dominant damage in these two cases reverting the nodal relationships back to behavior more similar to Damage Class 5.

Based on the DL data, the coefficients show a decisive jump during Damage Class 5. Although an argument could be made that the coefficient percent changes decrease after this and are not as effective in more severe damage detection,a counter-argument can be made. The damage ideally will have been significantly detected from earlier damage indicating coefficients and repaired prior to reaching this severe damage state.

5.4.1.2.2 Downward Unloading

The second loading condition is the downward unloading (DU) in which the beam is unloaded back to its original position. Figure 5.32 through Figure 5.40 show the relative changes for each progressive DU damage class as compared to the baseline state. The performance of the first four DU damage classes were similar to that of the DL case, with no coefficients changing more than 3.5%.

Damage Class 5, however, differs considerably, showing changes an order of magnitude lower than those from DL. A feasible explanation for this large difference is due to the crack opening at the top plate-to-beam weld. In the case of downward loading, the beam is pushed downward, causing the opening to enlarge and become more pronounced, resulting in large deviations from the baseline behavior. However, in downward unloading, as the beam is returned to neutral, the opening at the top is likewise

returned to a neutral, unopened position, causing the structure to reflect behavior more analogous to the undamaged state.

The relative changes shown for damage classes 6 and 7 both show more notable values, with those of Damage Class 7 higher than that of 6. This is also different from the DL observations as the DL values decreased from Damage Class 6 to 7. It is possible that as the beam returned to neutral in downward unloading, the out-of-plane beam bending became less pronounced. In both damage classes, the highest percent changes correspond to beam-column nodal pairs, on opposite sides of the damage.

From Damage Class 7 to Damage Class 8 the percent changes decrease asymmetrically. Though, as a whole the changes remain larger than those exhibited in Damage Class 6. This asymmetry could be due to the amplified prominence of the plastic hinge and out-of-plane bending. However, the percent changes remain dominant in the beam-beam and beam-column pairs, pointing to the damage in the beam. Damage Class 9, during which total failure occurred, shows a variety of results ranging from a 2% change to a 250% change. Again, the large changes point to damage within the beam, consistent with the observed deterioration.

5.4.1.2.3 Upward Loading

Upward loading is the third loading condition for the specimen. Because failure occurred in the downward unloading portion of the first cycle of Damage Class 9, upward loading and unloading each only have 8 damage classes. The changes for each UL class relative to the baseline state are presented for select nodal pairs in Figure 5.41 through Figure

5.48. Damage classes 1 through 3 a showed comparably low changes to that of the downward loading and unloading cases, corresponding to mild yielding.

However, unlike the previous two cases, UL Damage Class 4 saw large changes in the influence coefficients, up to 30%. These changes are likely more apparent in this case because as the beam is pushed upward the damage at the bottom of the beam becomes more prominent in the structure's behavior.

Damage Class 5 shows a decrease in changes from Damage Class 4, but the values are still notable. The column-column coefficient, $\alpha_{4\text{-}5}$, reduces to 0.5% likely due to the more severe beam yielding, isolating most of the movement to the beam. Damage Class 6 resulted in a much more significant decline in change values, with all below 10%. Again, the likely culprit for this unexpected reduction is the formation of the plastic hinge.

For Damage Class 7, the values return to the range observed in Damage Class 5, up to 18% for a beam-column coefficient. The final Damage Class 8 saw the highest percent changes for UL. These results are almost completely symmetric. For both classes, the changes unanimously point to damage surrounding the connection, specifically the beam portion.

5.4.1.2.4 Upward Unloading

Upward unloading, the fourth and final loading condition, corresponds to the beam's descent to the zero position from being displaced up. Figure 5.49 through Figure 5.56 show the relative changes for these UU damage classes as they compare to the undamaged baseline coefficients. As can be seen, the results for damage classes 1

through 5 are similar to that of the DU case, in which all values remained at or below 5%. Because for UU the beam is still in an upward position, the effects of the top cover plate damage are negligible.

Damage Class 6, when the plastic hinge fully forms, is marked by increases in percent change up to 10 times that of Damage Class 5. Coefficient, $\alpha_{4\text{-}5}$, also returns to its lowest values since Damage Class 1. Damage Class 7 shows a combination of increases and decreases in values, with all values pointing to damage between node 2 and the beam-column connnection. Finally, Damage Class 8, again not corresponding to total failure, also shows a combination of increases and decreases with all values indicating damage in the beam element.

Table 5.1. Drift sequence applied to test structure

Number of Cycles	Angle of Drift (radian)
6	0.00375
6	0.005
6	0.0075
4	0.01
2	0.015
2	0.02
2	0.03
2	0.045
1	0.05
1	0.06

Table 5.2. Test A damage notes by damage class and drift angle

Damage Class	Angle of Drift (radians)	Damage Observations
0	0.00375 & 0.005	No visible damage
1	0.0075	Onset of yielding under bottom of cover plate
2	0.01	Some slight yielding on the beam flange (extreme fiber) More yielding on the bottom cover plate
3	0.015	Yielding in the web about 1/5 of beam depth More yielding on the bottom cover plate Yielding in the through-thickness of beam flange Yielding in the top and bottom of beam flange
4	0.02	Web yielding of beam increased to 1/3 beam depth More yielding on the bottom cover plate More yielding on the beam flanges (top and bottom of both) Small crack (1/2 in) in top cover plate to beam weld (bottom side) 2 small crack (1 in) in top cover plate-to-beam weld No crack in base metal
5	0.03	Extreme yielding in the bottom cover plate Considerable yielding in beam bottom flange Web yielding more than 1/3 beam depth Top cover plate separated from beam Crack of top cover plate-to-beam weld (bottom side) opened up to 2 in Cracks of top and bottom cover plate-to-beam weld (top side at cut-out) opened more than 2.5 in
6	0.045	Web start to buckle Top flange start to buckle Bottom cover plate separated from the beam Plastic hinge completely formed Bottom cover plate-to-beam weld crack propagated Bottom flange started to buckle (at the end of cycle) Web buckled at lower depth of beam Small crack in side plate-to-column weld (left side)
7	0.05	Top flange buckling increased Web buckling increased Bottom flange buckling increased Bottom web buckling increased Crack in cover plate-to-beam weld stopped where the beam-to-side plate weld starts
8	0.06	Top cover plate-to-beam weld crack propagated to the base metal (beam flange) about ¼ in
9	0.07	Fracture from the bottom flange propagated into the web more than half the depth of beam

Figure 5.1. Typical experimental test setup at Lehigh's ATLSS Center

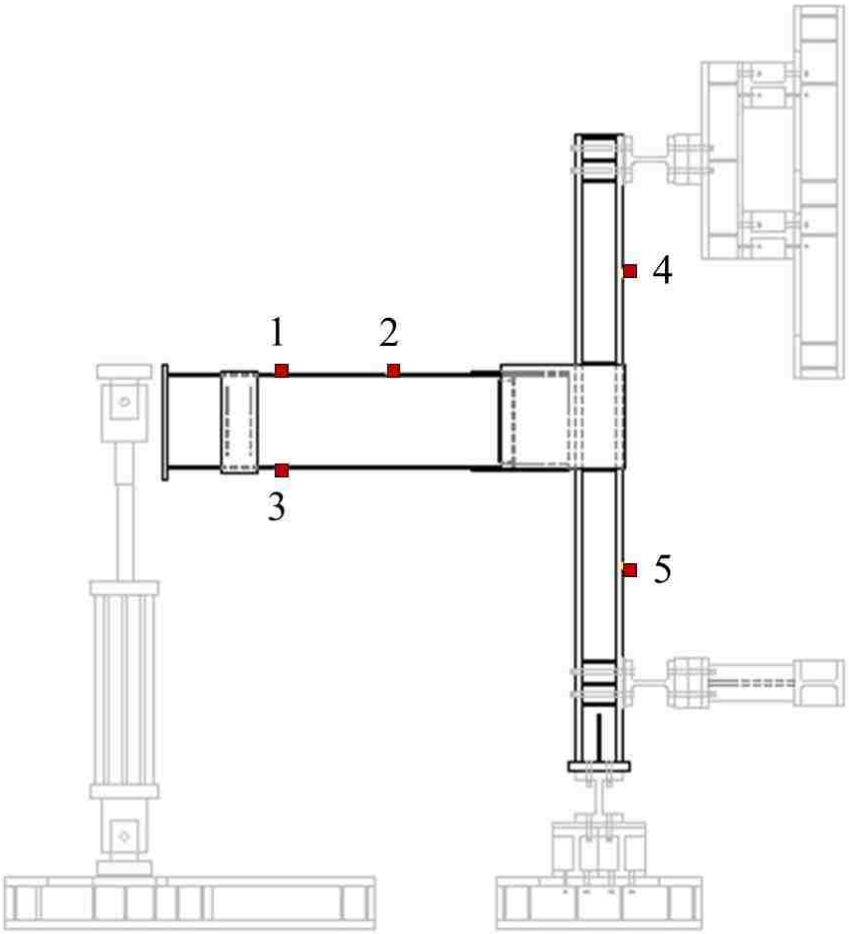

Figure 5.2. Test setup with strain gauge instrumentation plan

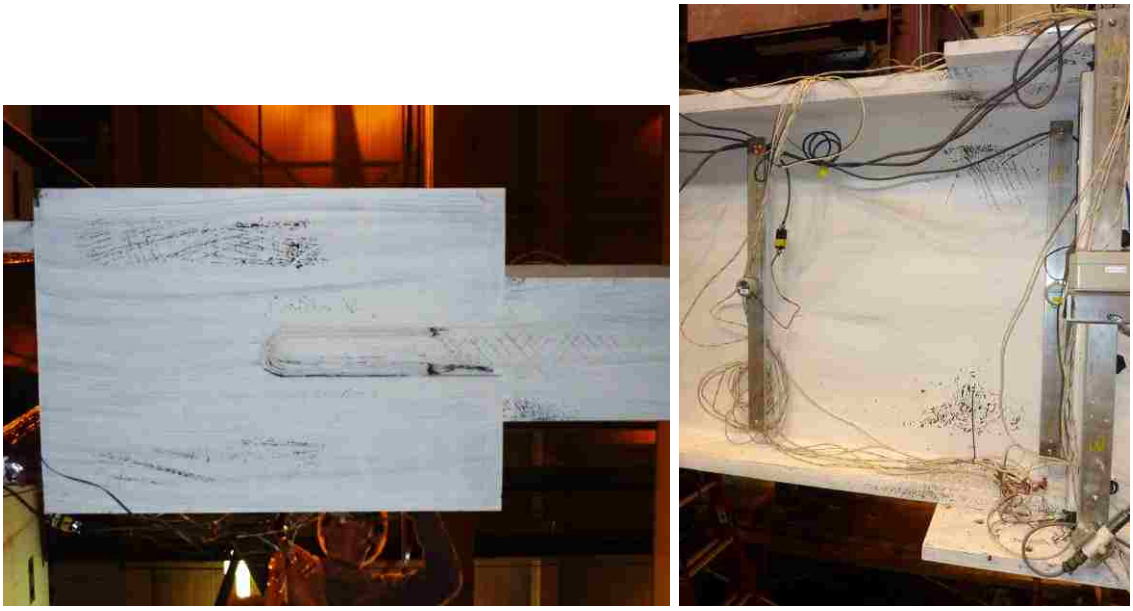

Figure 5.3. Photos from Test A Damage Class 3

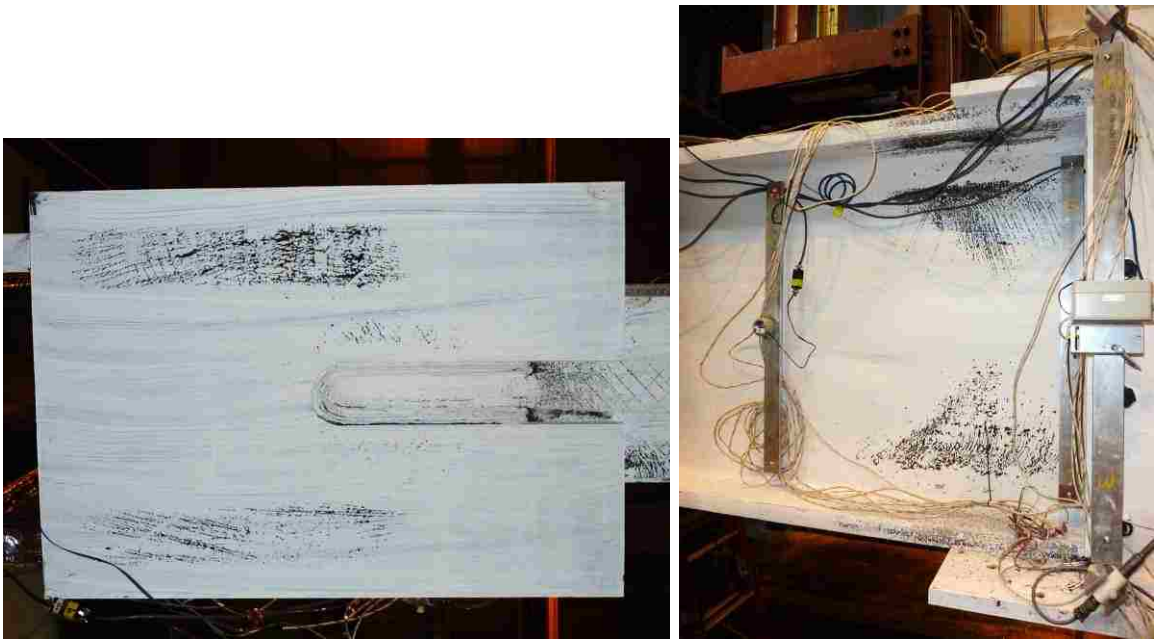

Figure 5.4. Photos from Test A Damage Class 4

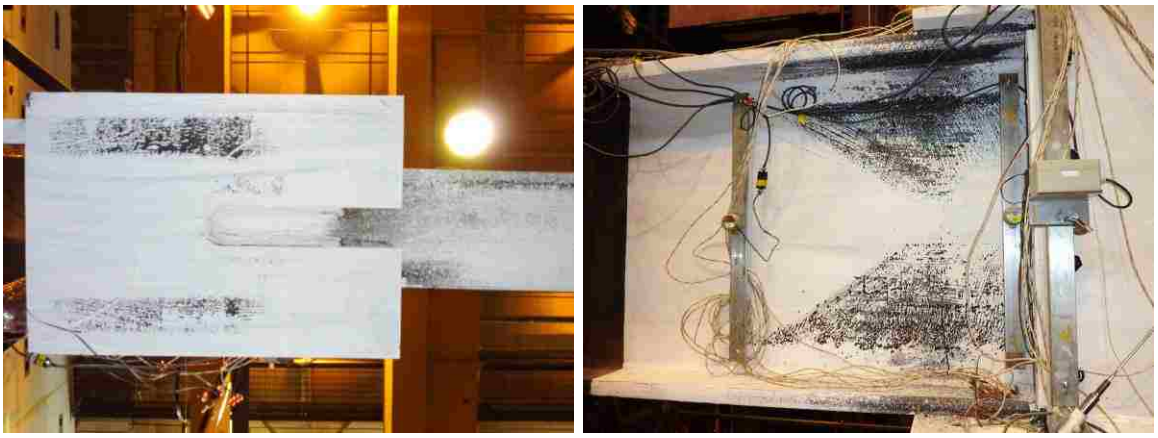

Figure 5.5. Photos from Test A Damage Class 5

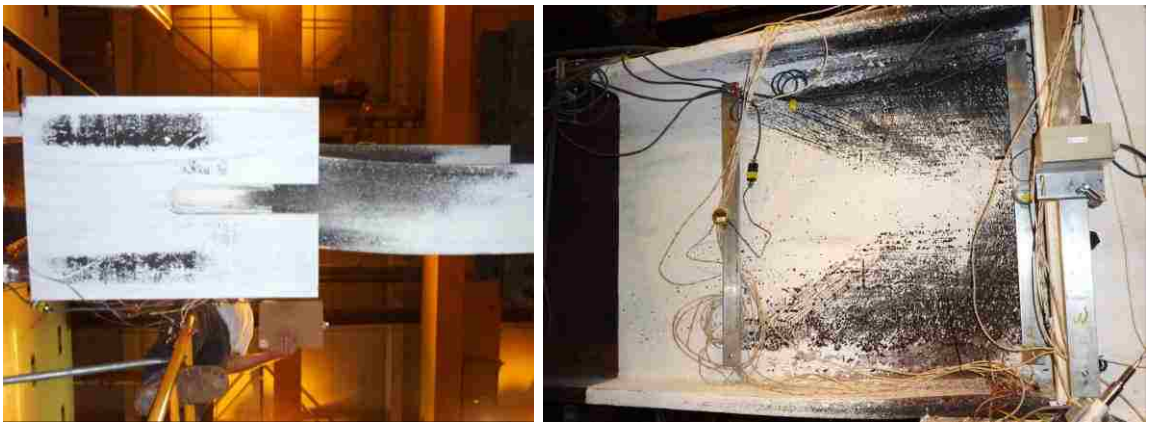

Figure 5.6. Photos from Test A Damage Class 6

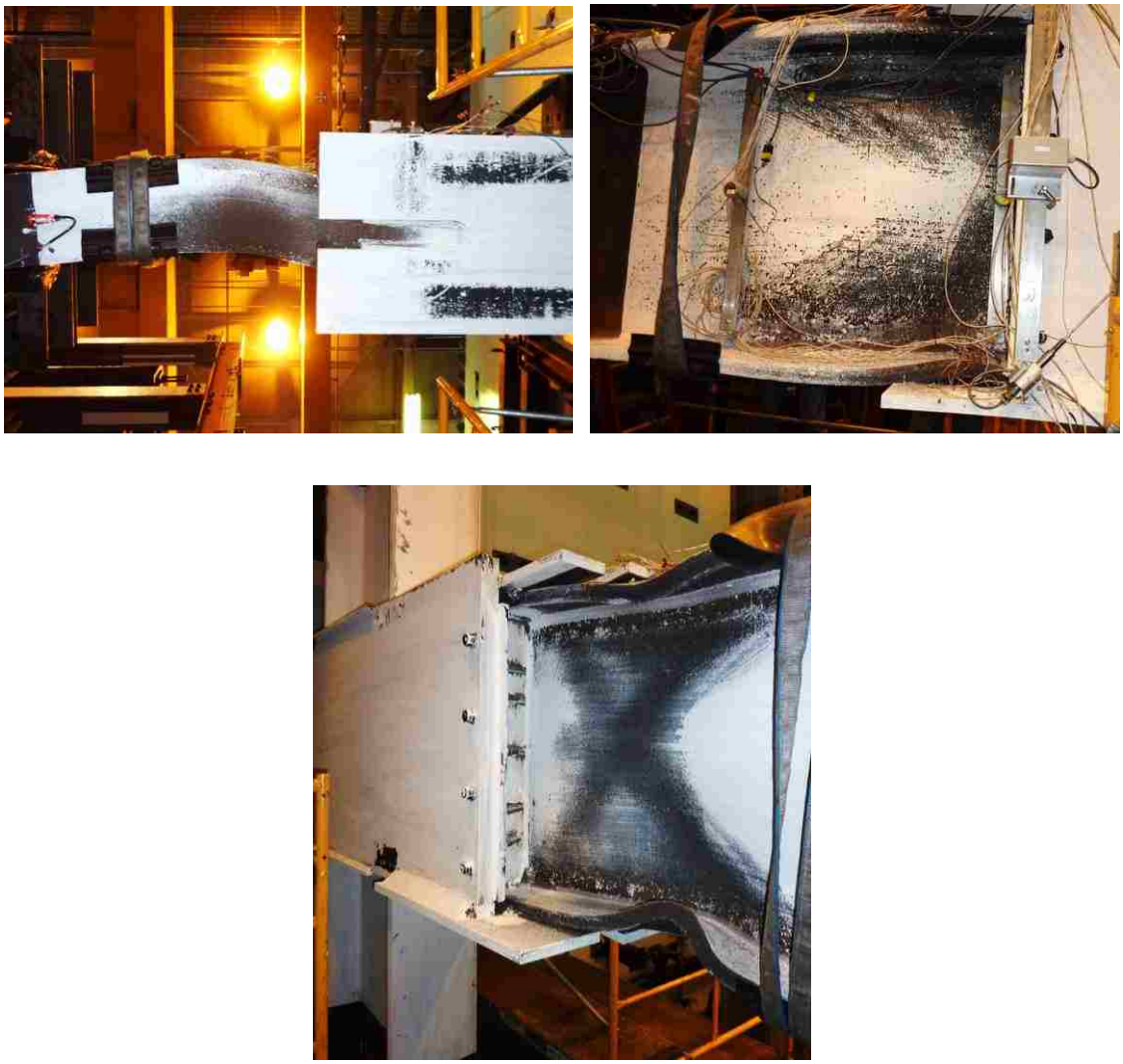

Figure 5.7. Photos from Test A Damage Class 7

Figure 5.8. Photos from Test A Damage Class 8

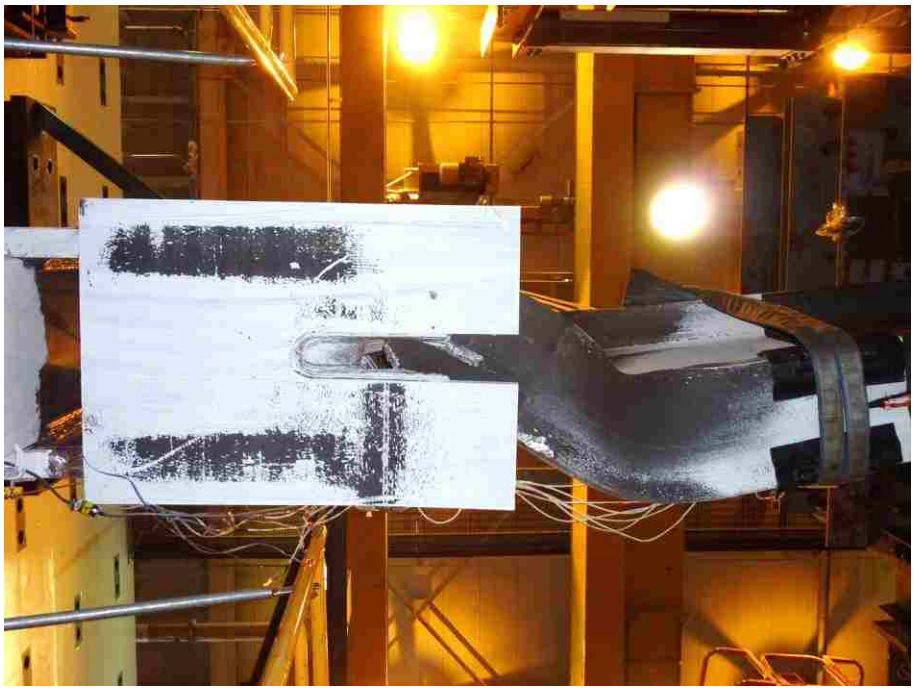

Figure 5.9. Photos from Test A Damage Class 9 (Failure)

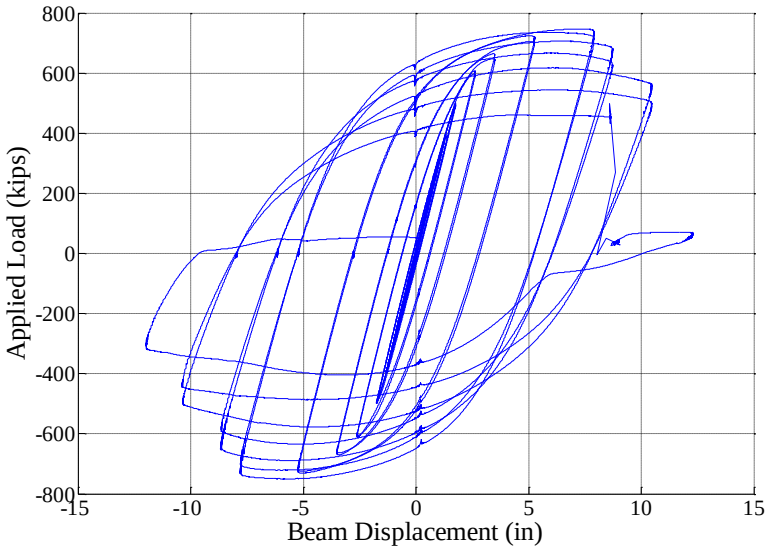

Figure 5.10. Force-displacement curve for Test A

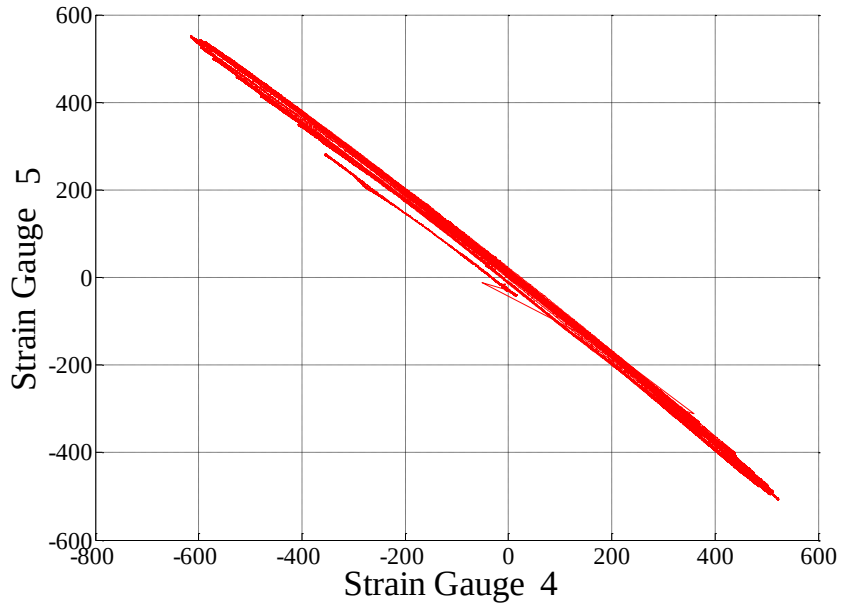

Figure 5.11. Relationship between strain gauges 4 and 5 in Test A

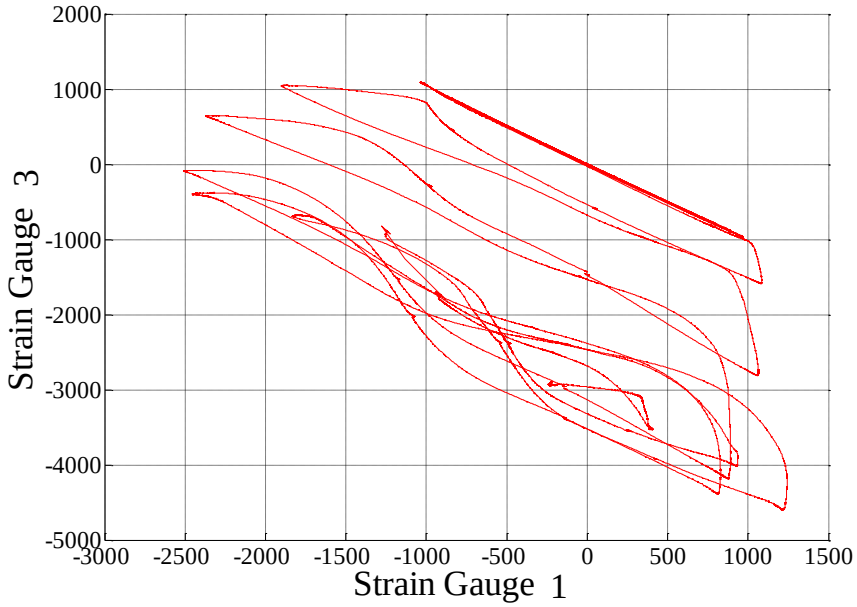

Figure 5.12. Relationship between strain gauges 1 and 3 in Test A

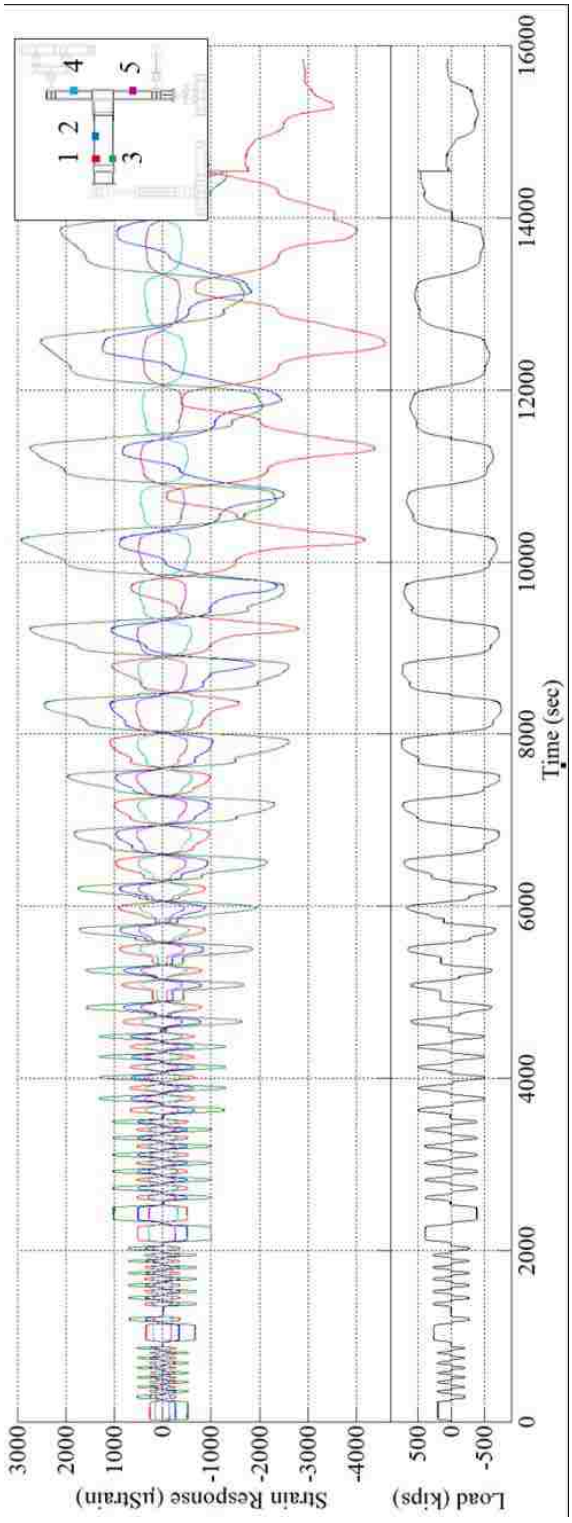

Figure 5.13. Strain response and applied load time histories for Test A

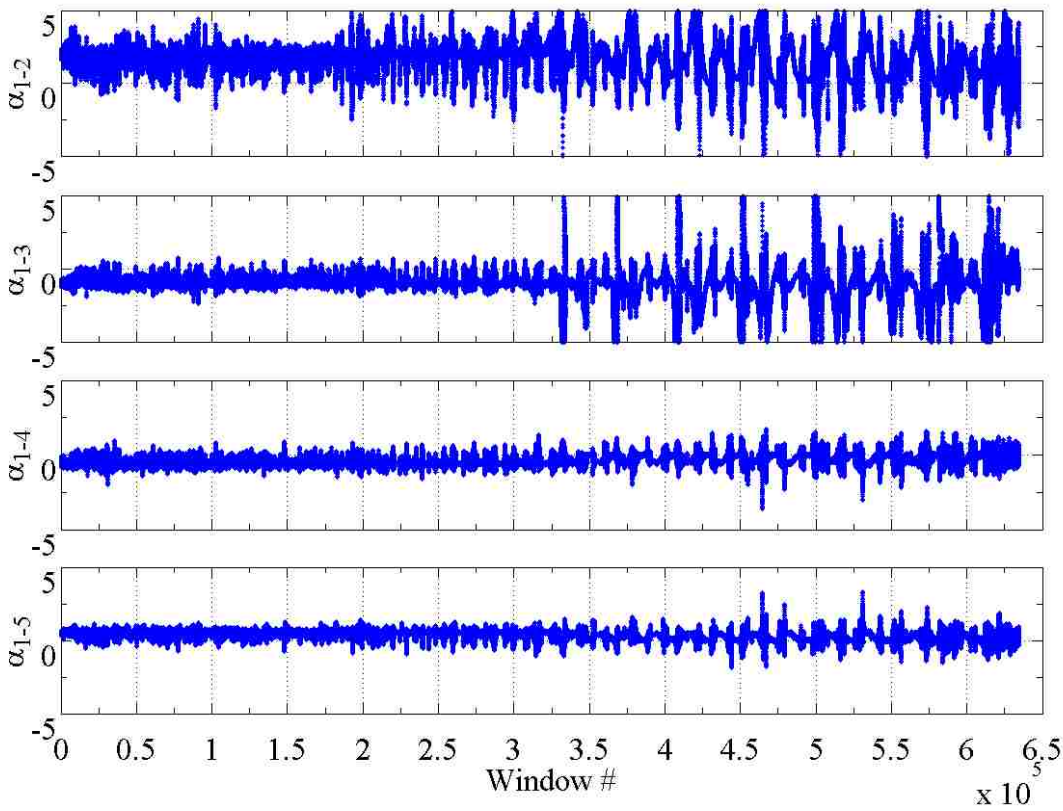

Figure 5.14. A selection of preliminary influence coefficients calculated for entire dataset using a 50-sample moving window for Test A

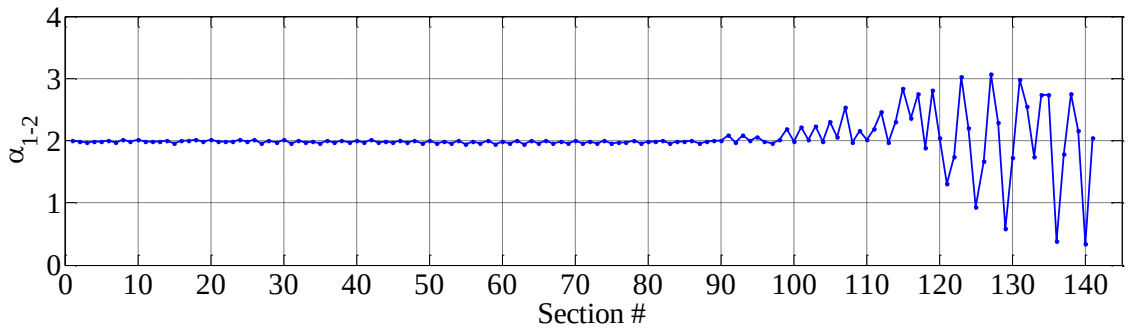

Figure 5.15. Preliminary influence coefficient, α_{1-2}, considering loading and unloading sections of Test A data only

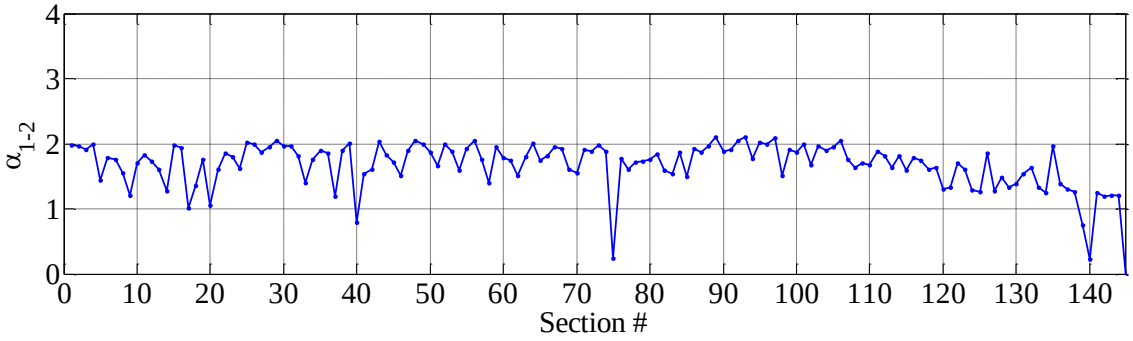

Figure 5.16. Preliminary influence coefficient considering holding sections of Test A data only

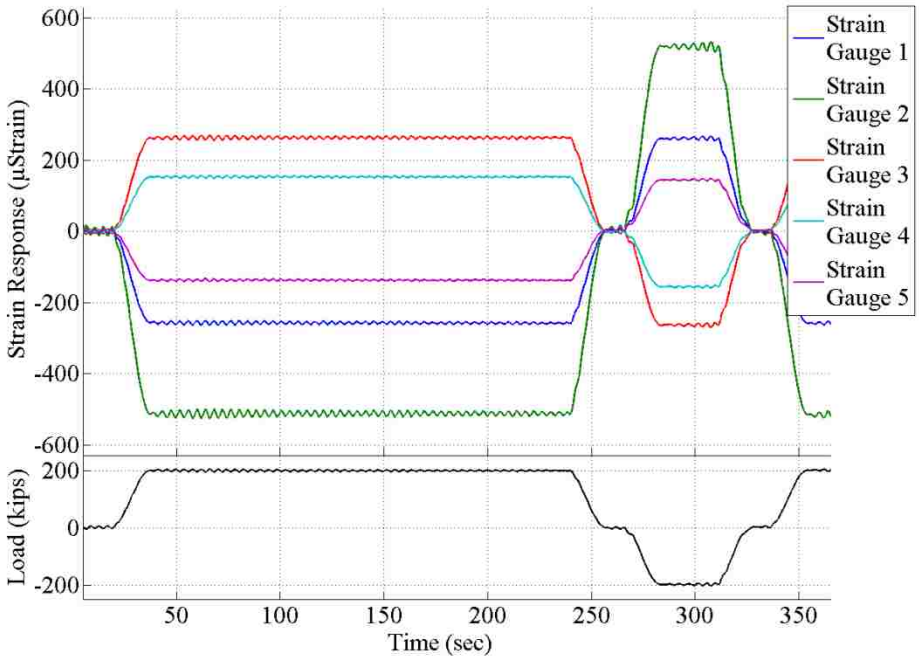

Figure 5.17. Strain response and applied load histories show greater noise at constant load for Test A data

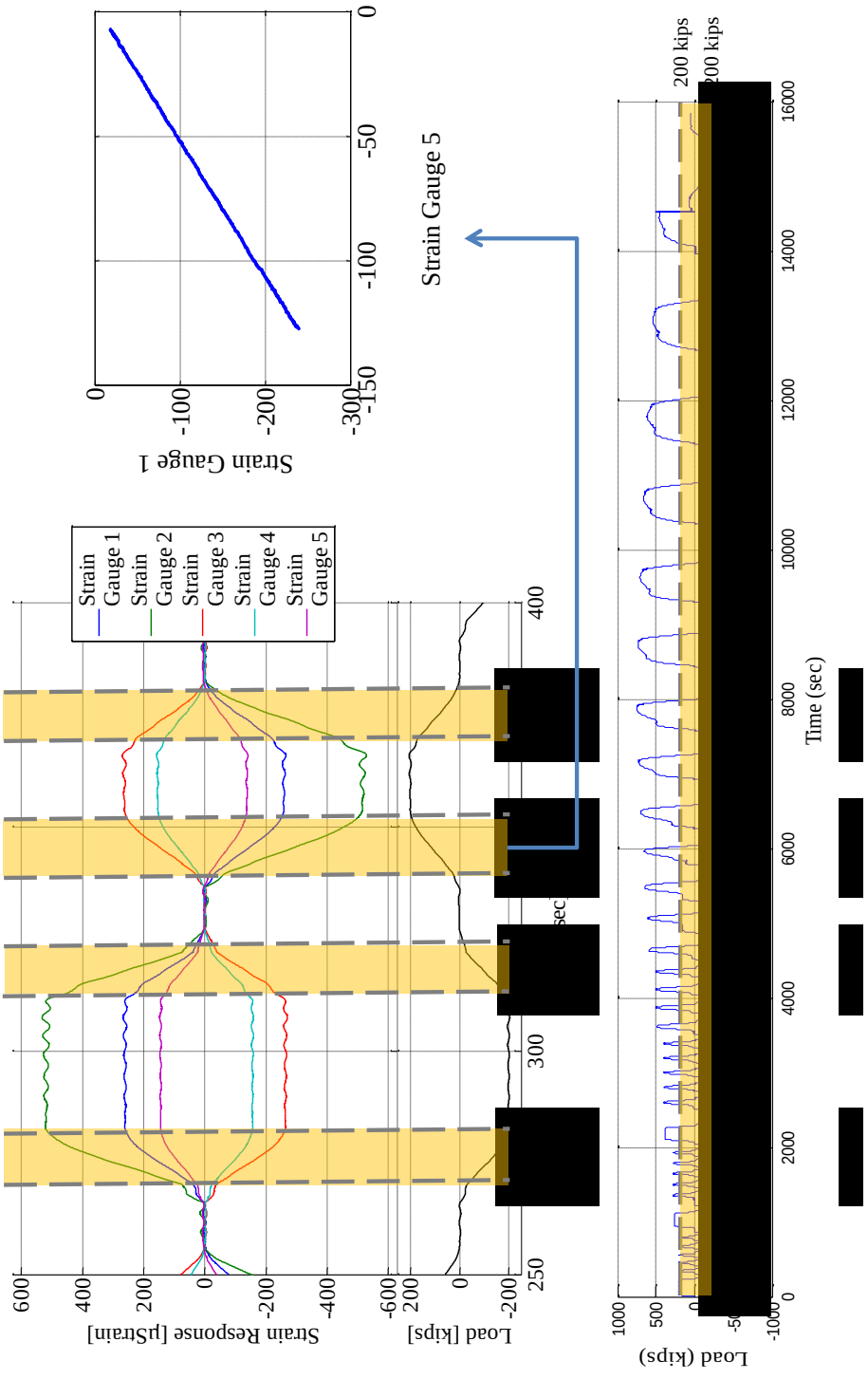

Figure 5.18. Holding and loading sections trimmed by load to capture linear-elastic behavior of data for Test A data

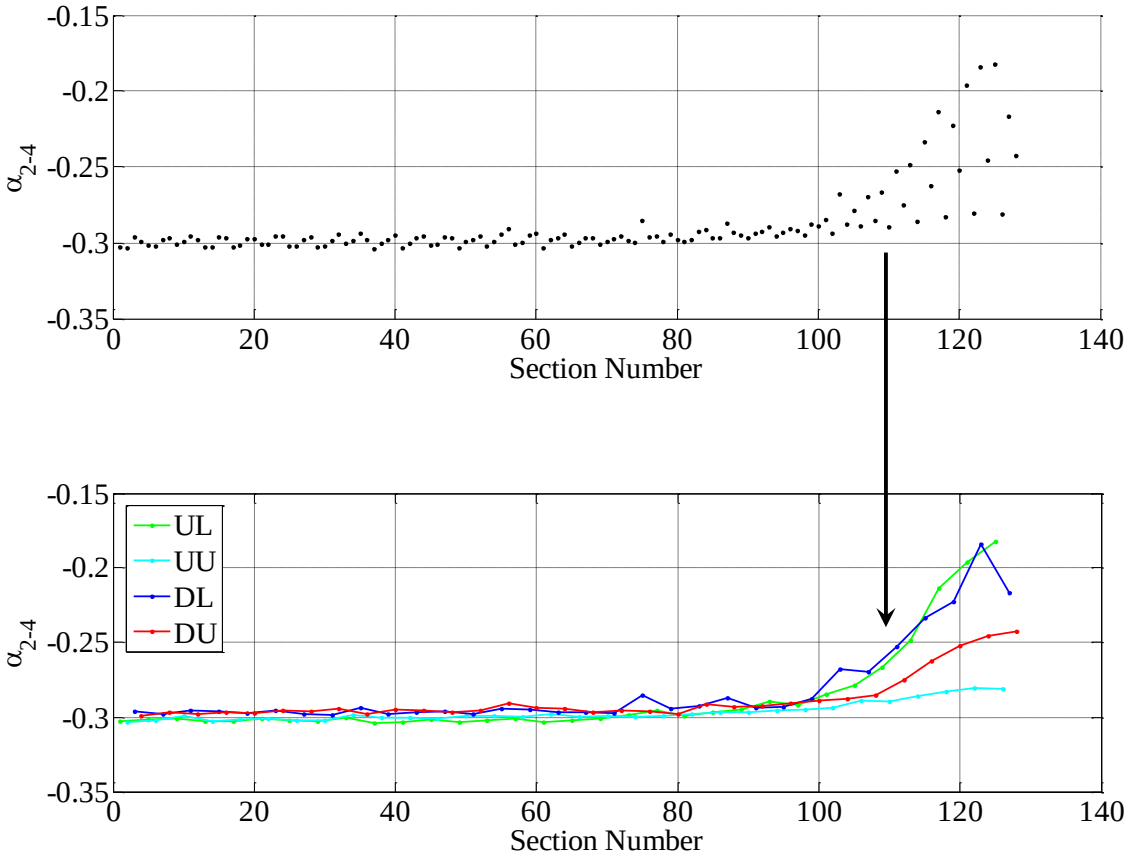

Figure 5.19. Separating the coefficients according to loading type shows more consistency in the deviation of coefficients

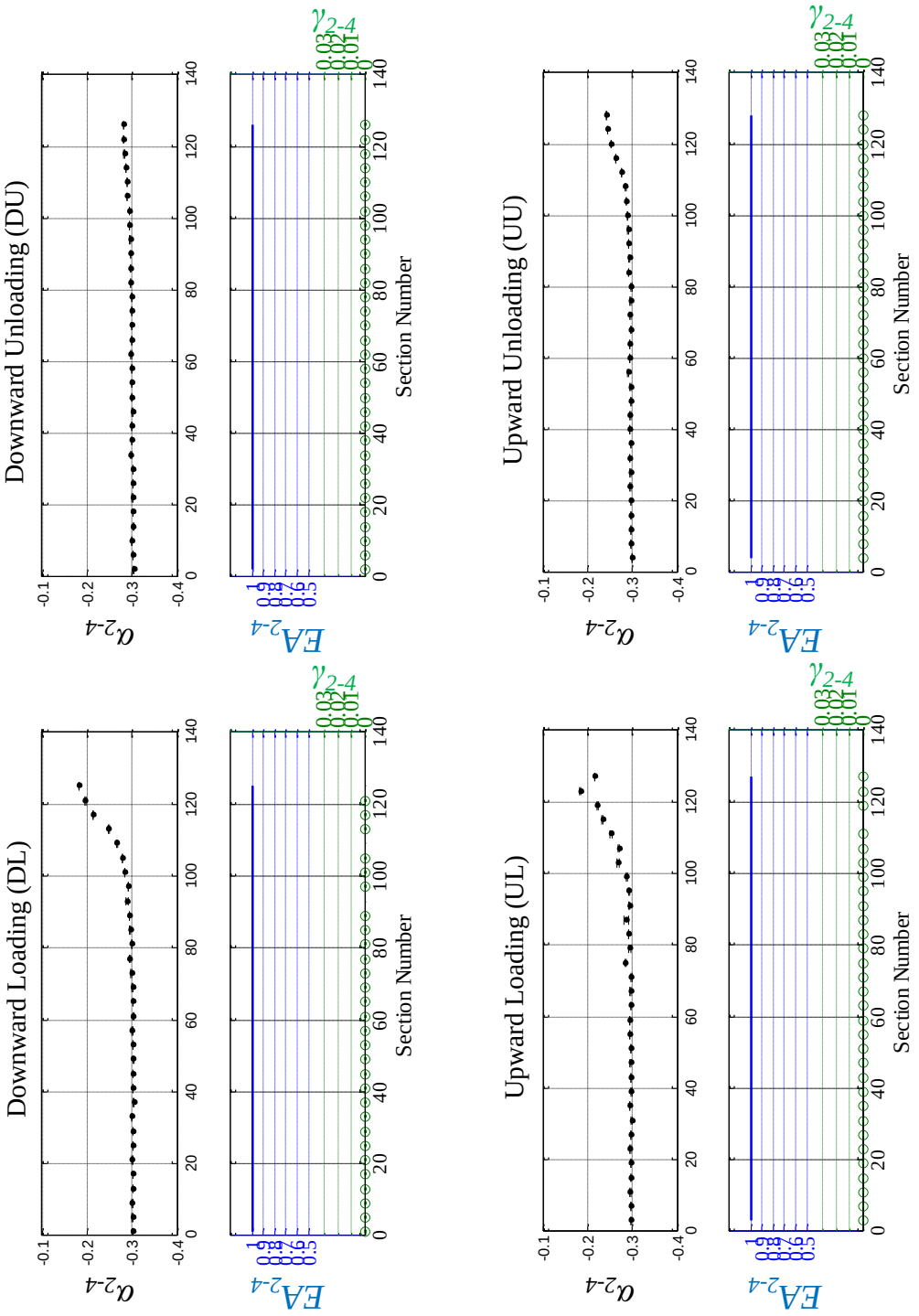

Figure 5.20. *α*, *EA*, and *γ* for all four loading conditions for Test A nodal pair 2-4

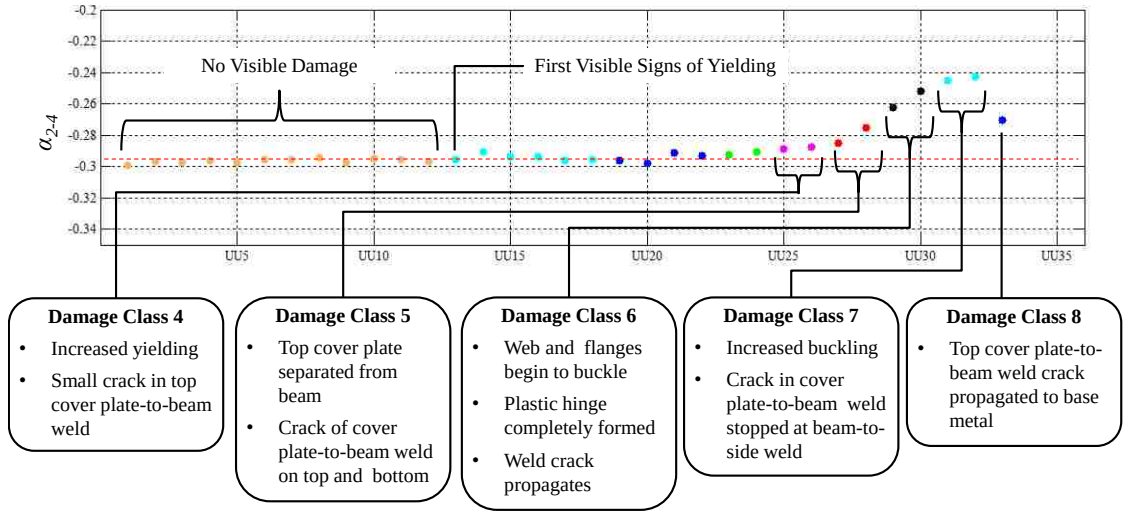

Figure 5.21. α_{2-4} for Test A UU sections shown with progressive damage classes

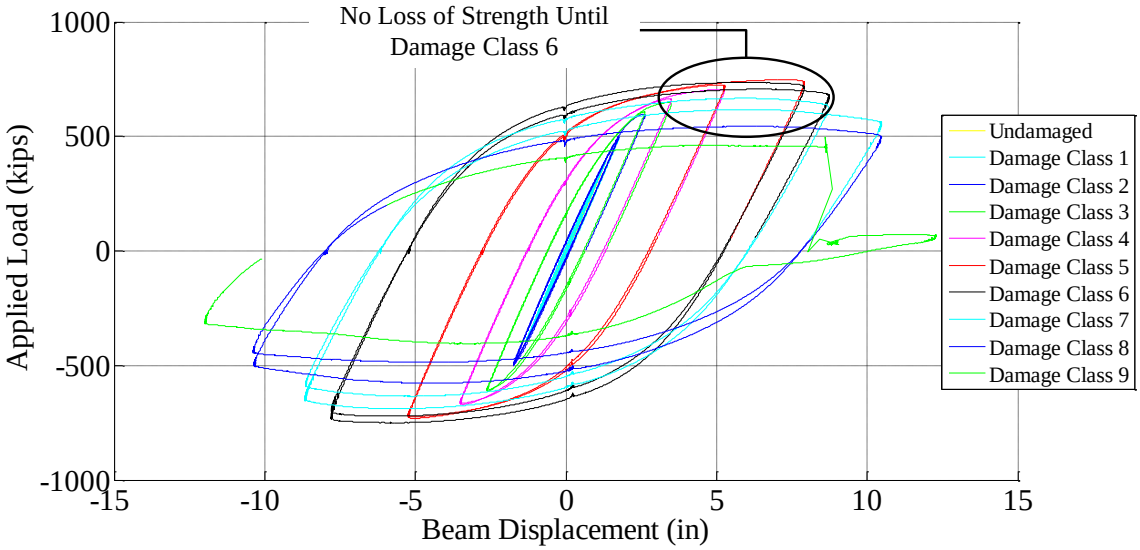

Figure 5.22. Test A load-displacement plotted by damage class showing where loss of strength occurs

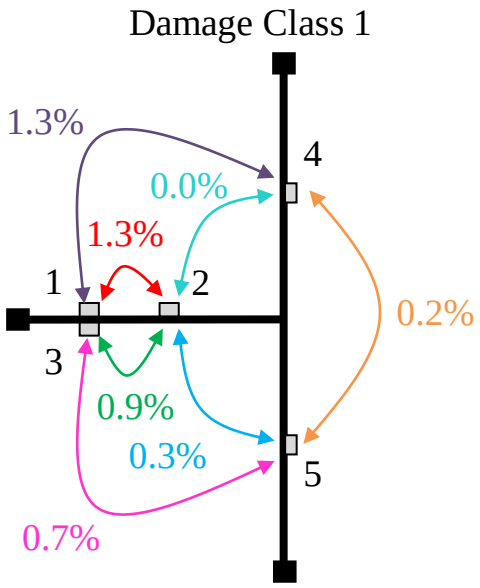

Figure 5.23. Relative change for DL Damage Class 1 (Test A)

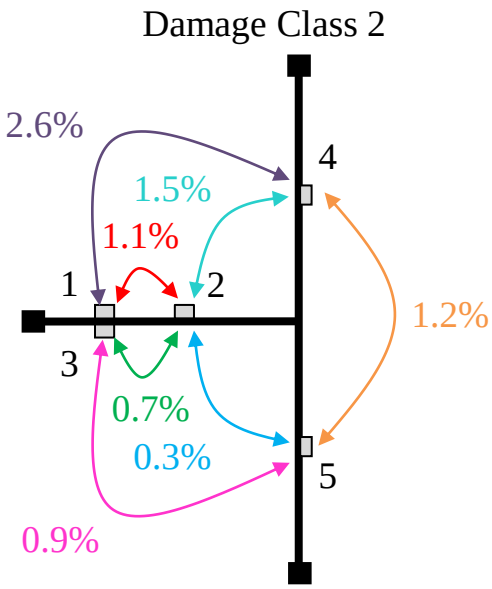

Figure 5.24. Relative change for DL Damage Class 2 (Test A)

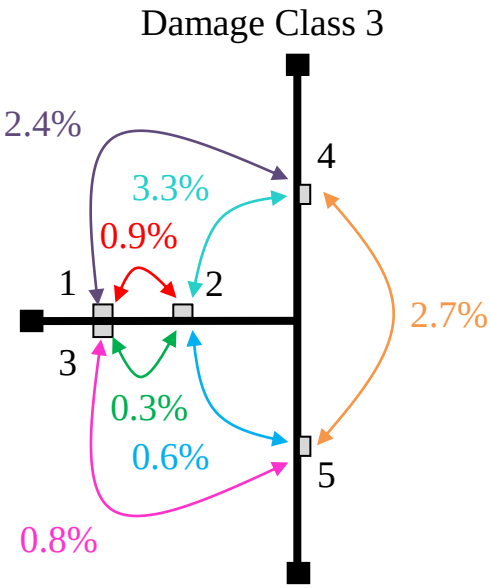

Figure 5.25. Relative change for DL Damage Class 3 (Test A)

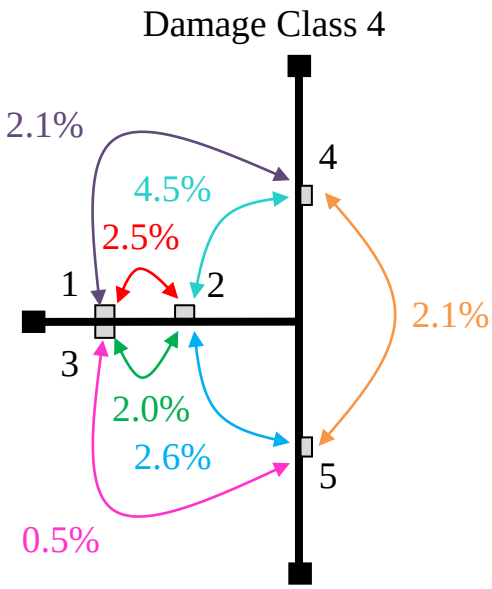

Figure 5.26. Relative change for DL Damage Class 4 (Test A)

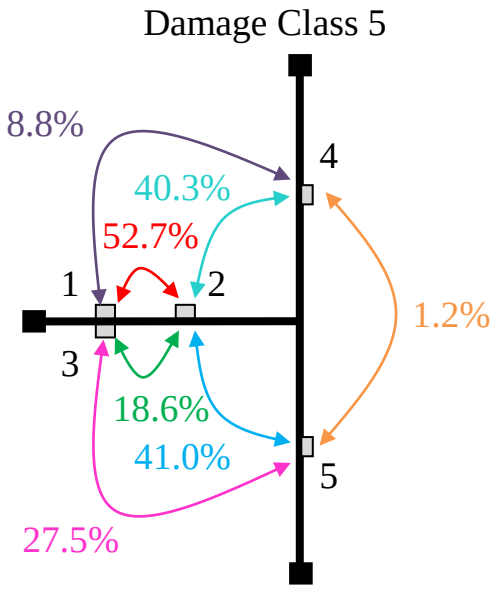

Figure 5.27. Relative change for DL Damage Class 5 (Test A)

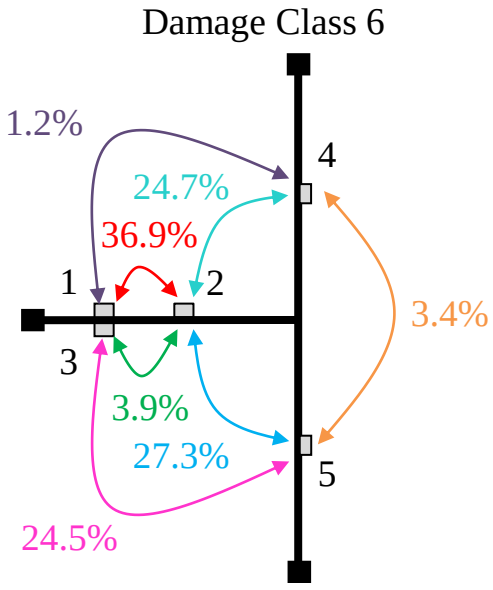

Figure 5.28. Relative change for DL Damage Class 6 (Test A)

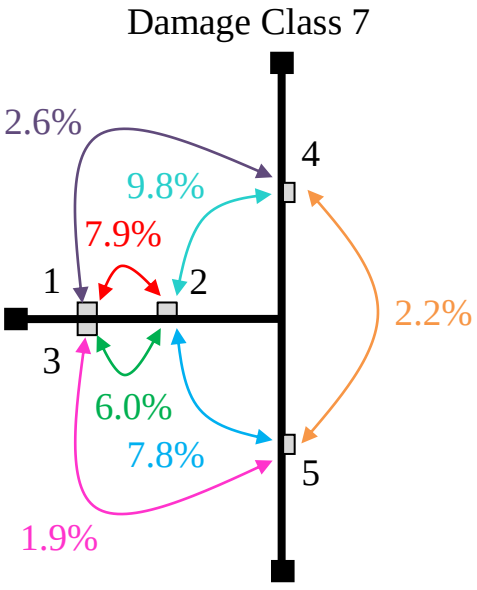

Figure 5.29. Relative change for DL Damage Class 7 (Test A)

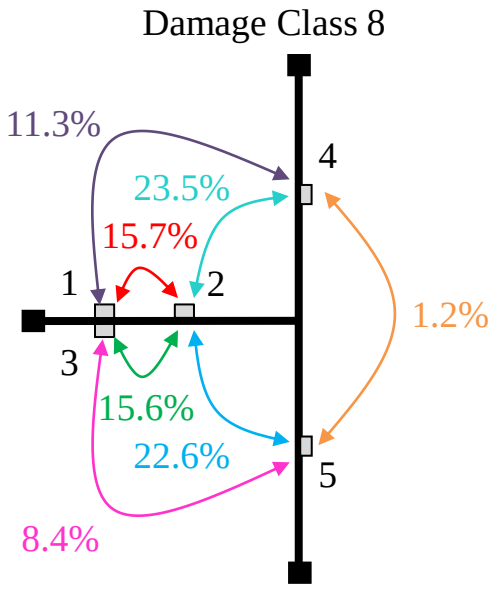

Figure 5.30. Relative change for DL Damage Class 8 (Test A)

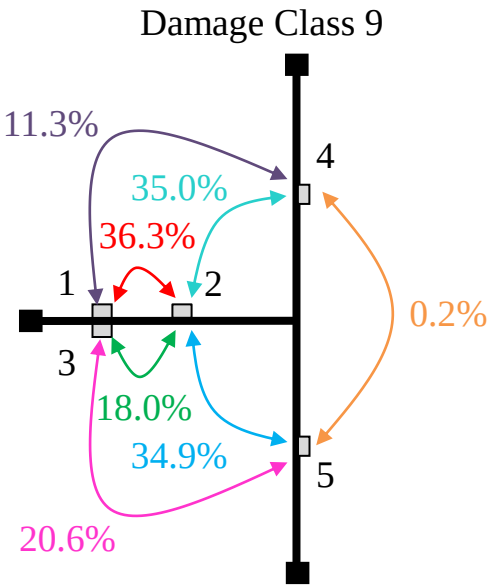

Figure 5.31. Relative change for DL Damage Class 9 (Test A)

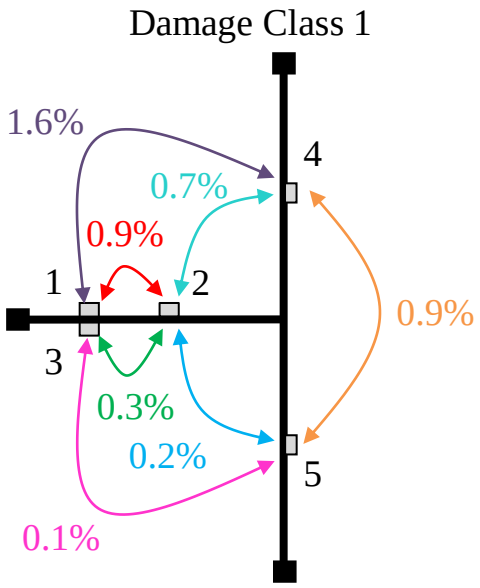

Figure 5.32. Relative change for DU Damage Class 1 (Test A)

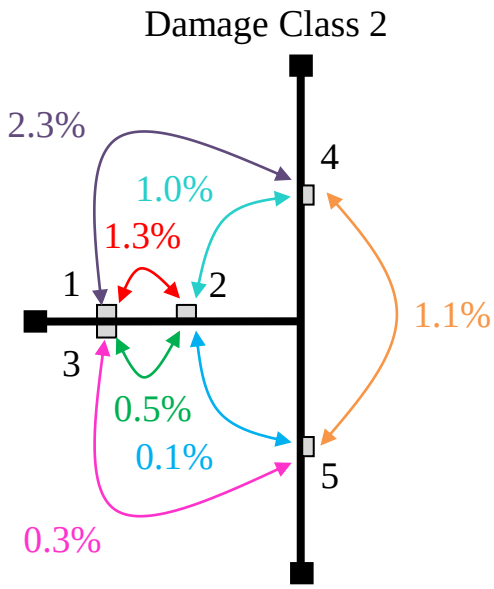

Figure 5.33. Relative change for DU Damage Class 2 (Test A)

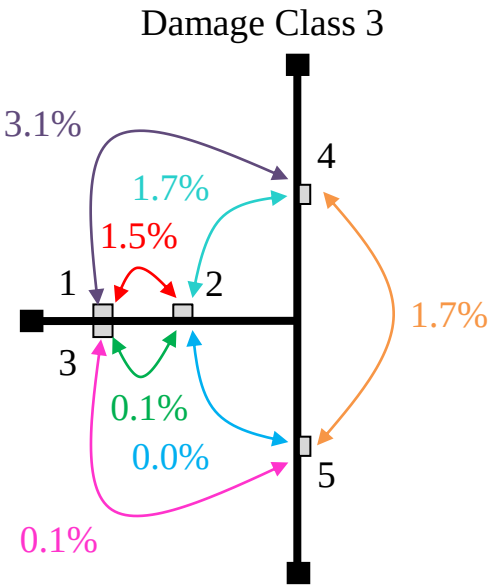

Figure 5.34. Relative change for DU Damage Class 3 (Test A)

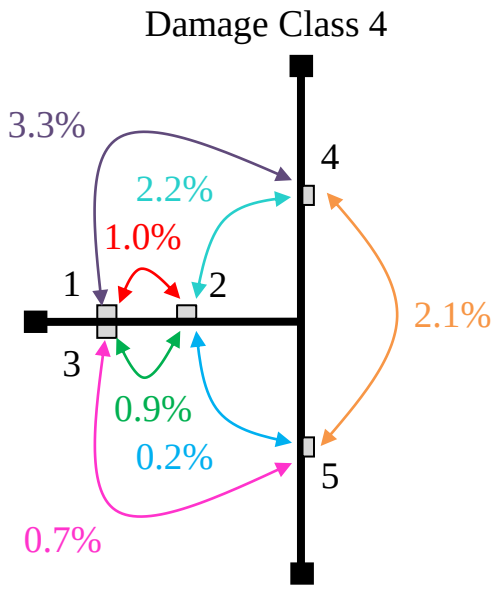

Figure 5.35. Relative change for DU Damage Class 4 (Test A)

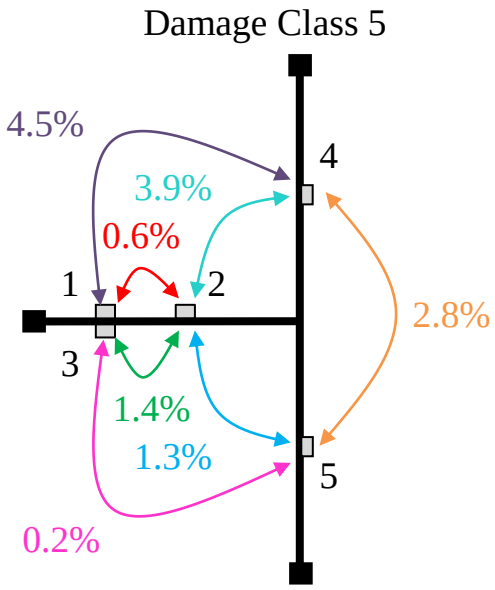

Figure 5.36. Relative change for DU Damage Class 5 (Test A)

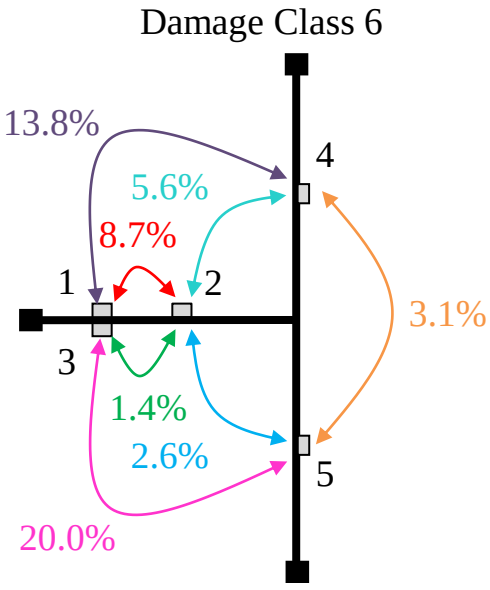

Figure 5.37. Relative change for DU Damage Class 6 (Test A)

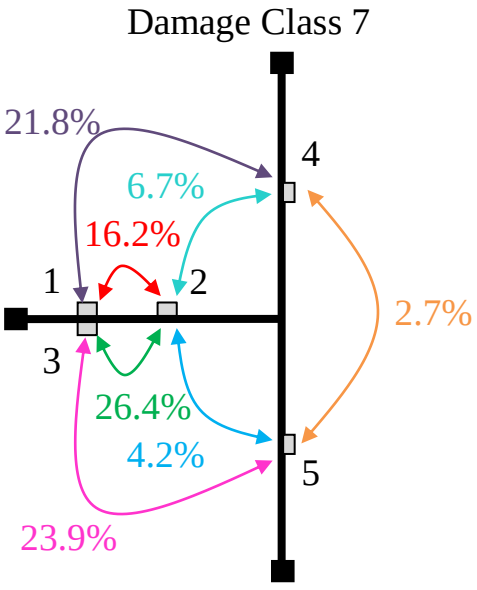

Figure 5.38. Relative change for DU Damage Class 7 (Test A)

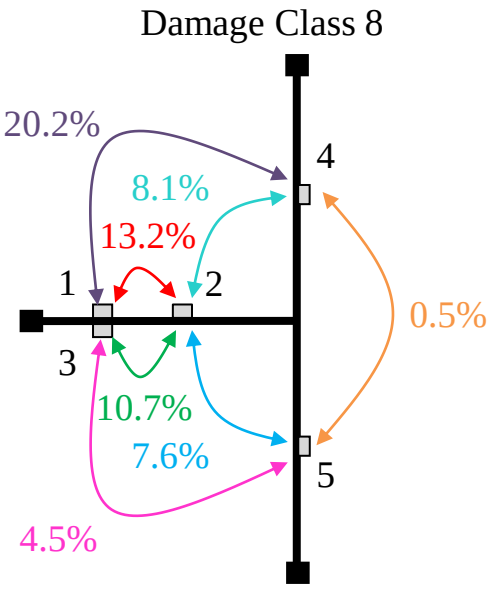

Figure 5.39. Relative change for DU Damage Class 8 (Test A)

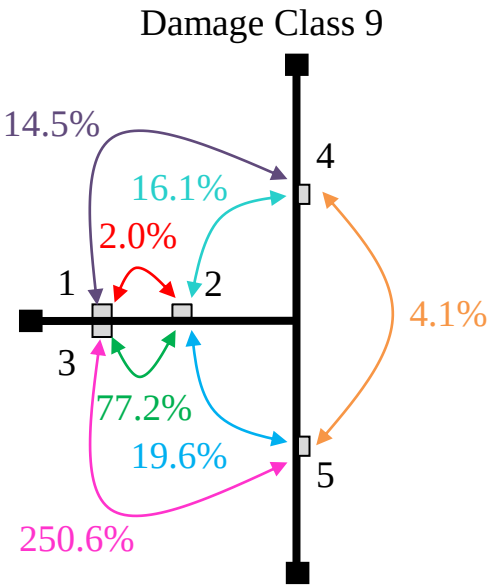

Figure 5.40. Relative change for DU Damage Class 9 (Test A)

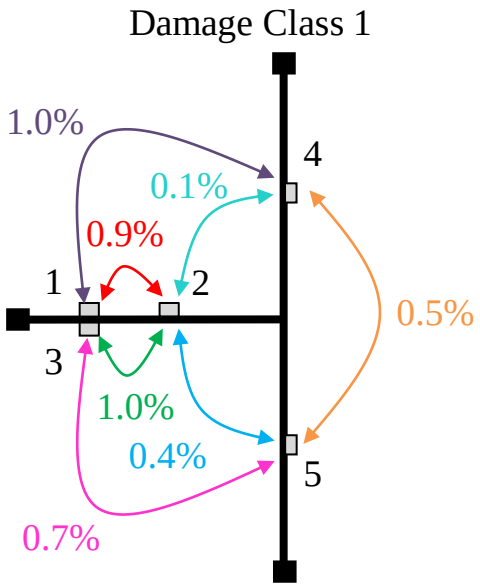

Figure 5.41. Relative change for UL Damage Class 1 (Test A)

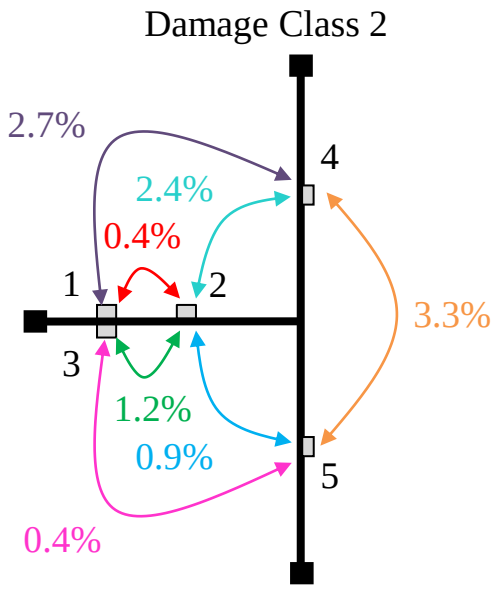

Figure 5.42. Relative change for UL Damage Class 2 (Test A)

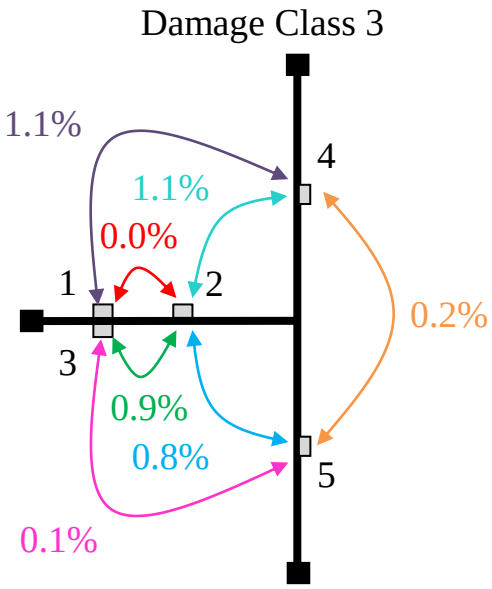

Figure 5.43. Relative change for UL Damage Class 3 (Test A)

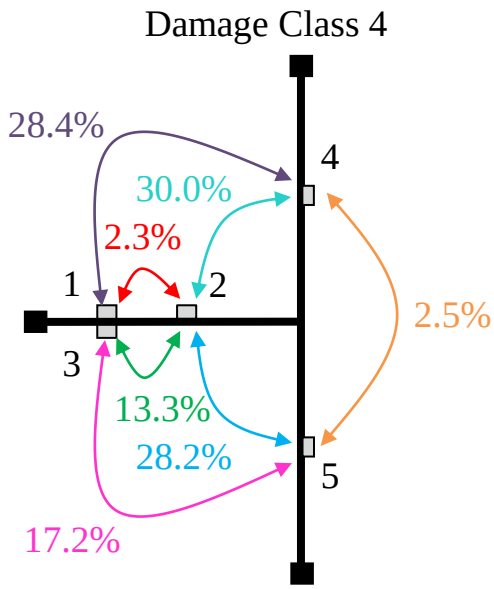

Figure 5.44. Relative change for UL Damage Class 4 (Test A)

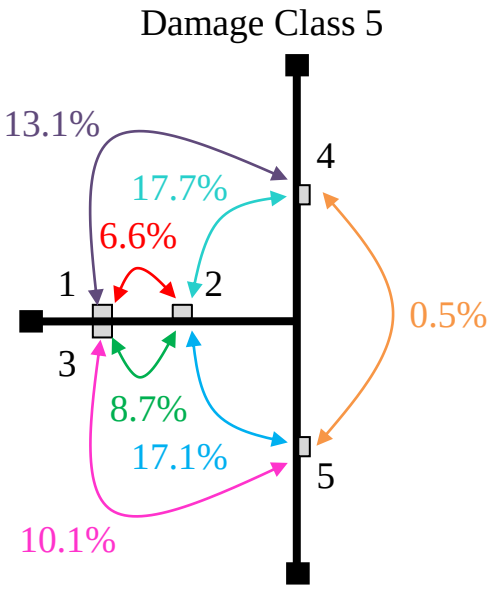

Figure 5.45. Relative change for UL Damage Class 5 (Test A)

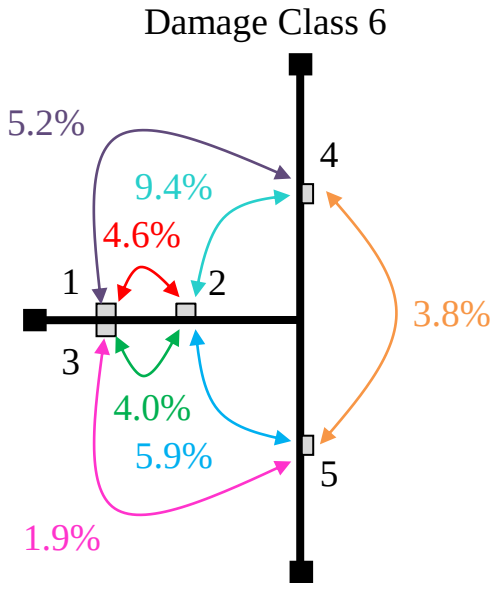

Figure 5.46. Relative change for UL Damage Class 6 (Test A)

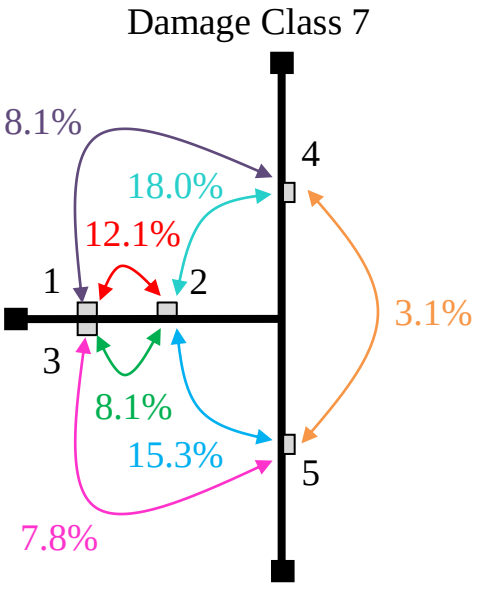

Figure 5.47. Relative change for UL Damage Class 7 (Test A)

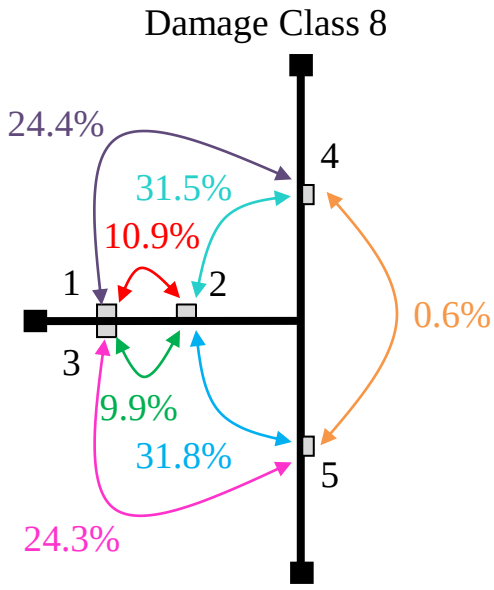

Figure 5.48. Relative change for UL Damage Class 8 (Test A)

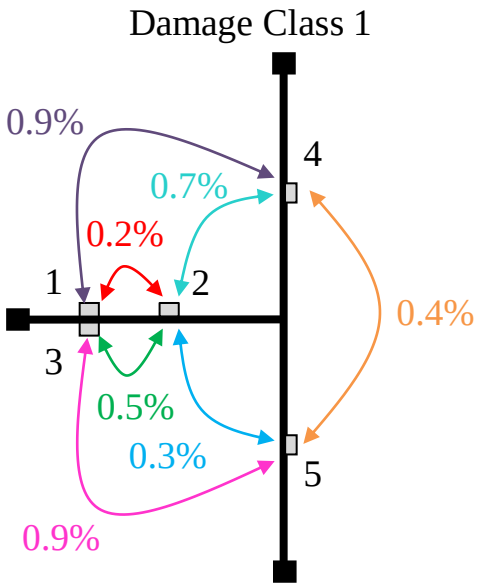

Figure 5.49. Relative change for UU Damage Class 1 (Test A)

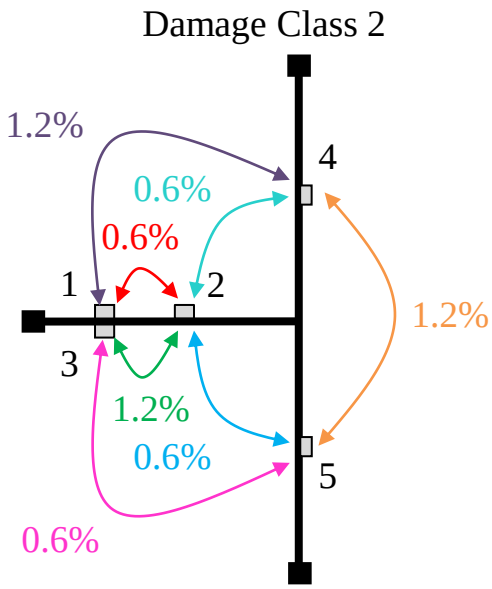

Figure 5.50. Relative change for UU Damage Class 2 (Test A)

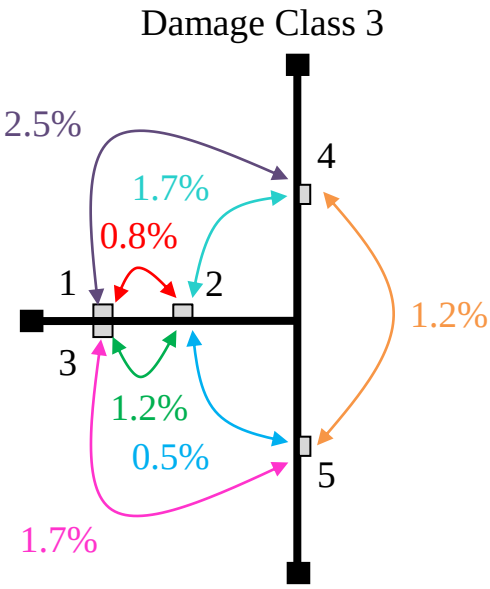

Figure 5.51. Relative change for UU Damage Class 3 (Test A)

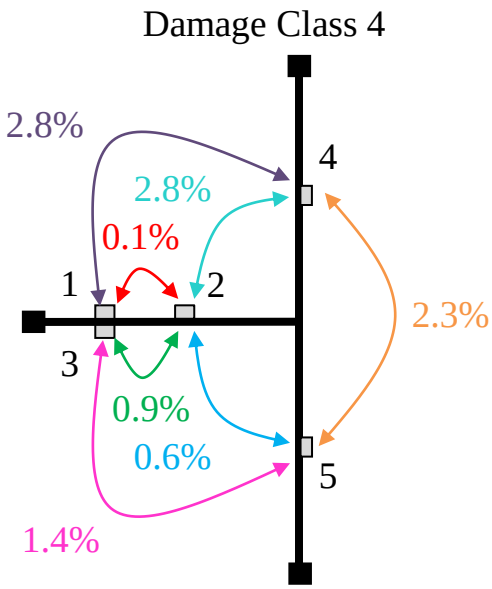

Figure 5.52. Relative change for UU Damage Class 4 (Test A)

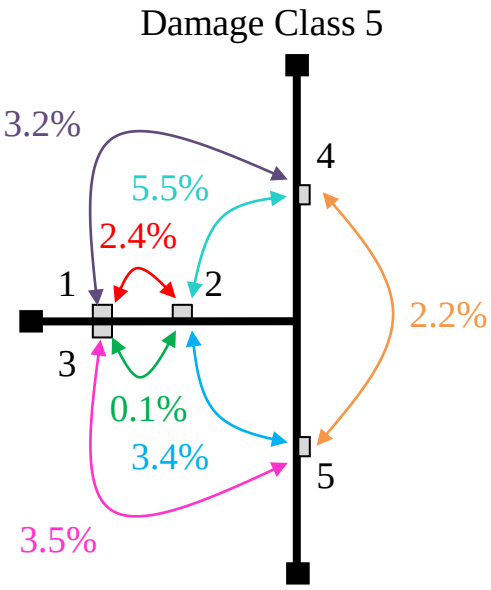

Figure 5.53. Relative change for UU Damage Class 5 (Test A)

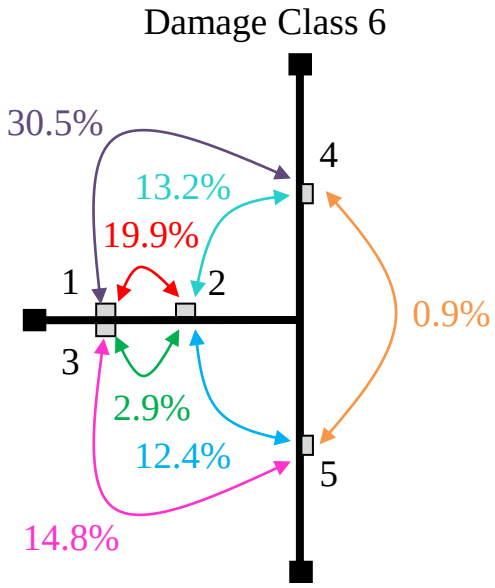

Figure 5.54. Relative change for UU Damage Class 6 (Test A)

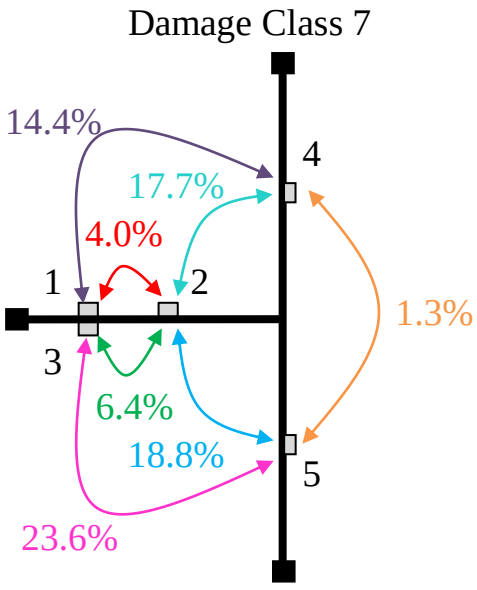

Figure 5.55. Relative change for UU Damage Class 7 (Test A)

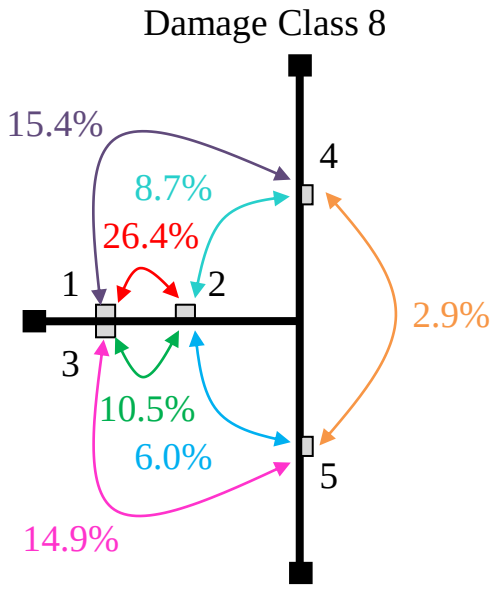

Figure 5.56. Relative change for UU Damage Class 8 (Test A)

Chapter 6 Summary, Conclusions, and Future Work

An innovative localized damage detection method that uses structural responses collected via a densely clustered sensor network to effectively identify damage is presented in this thesis. The proposed method is an output-only method that is not limited to specific structural materials types or loading conditions. Knowledge of a baseline healthy state condition is required to which to compare the state in question to determine if damage has occurred.

The damage indicating parameters are influence coefficients obtained by regressing the responses from two different points on the structure. Linear regression analysis is used for finding these parameters under the assumption of linear-elastic behavior in the structure before and after a damaging event. When damage occurs in the structure, the relationship between these two points change, in turn causing a change in the influence coefficient. With a densely clustered network of sensors, multiple influence coefficients can be determined. The pattern of change in this system of influence coefficients points to not only the existence, but also to the location of damage.

A statistical framework is adopted to determine the change-point in the influence coefficient to determine damage to a significant level. This statistical analysis allows for simplified monitoring of changes in the influence coefficients as data is collected over time. Additionally, two parameters, evaluation accuracy and normalized estimation error, were introduced to determine which influence coefficients will be the most reliable damage indicators in a system. This is particularly useful in the instrumentation of a structure with a large sensor network, in which case the number of possible influence

coefficients likewise becomes large. Being able to determine the most reliable parameters reduces processing, allowing for more efficient damage identification.

This thesis presented three experimental applications for validation of the proposed localized damage detection method. The first specimen was a small-scale beam-column connection that served to represent the local portion of a larger beam and column as they come to a joint. This model was also simulated in SAP2000 to verify the experimental prototype. The results of this application demonstrated the importance of using *EA* and γ for identifying reliable damage indicators. Additionally, it was seen that a typical pattern of change for damage shows the largest changes for pair-wise coefficients where each node is on an opposite side of the damage location. The coefficients with the smallest change are intuitively from nodes that are remote from the damage member. Hypothesis testing was used to statistically identify the damage. It was found that the test statistic will cross the confidence bounds earliest when the influence coefficient exhibits a large change in conjunction with large accuracy and low error values. The beam-column was instrumented with parallel networks of wired and wireless accelerometers. The data was processed for each and compared side by side to investigate the performance of the WSN. The results showed that while the WSN data contained more noise than that of the wired network, the WSN was still effective in identifying damage.

The second application that was presented involved simulated models and an experimental prototype of a two-bay, uneven span frame that was instrumented with wired accelerometers. The frame was developed with the intention of representing either a building frame or a bridge girder. Additionally, it was built with capability for a variety of damage combinations with nine distinct locations along the structure. The larger

structure also allowed for the implementation of a larger sensor network of 21 accelerometers. In order to reduce the number of insignificant influence coefficient parameters, coefficients were obtained only for pairs within one of the three local joints.

Simulated results showed that the damage that was created by a 20% stiffness reduction in the section, equal to a global stiffness reduction below 1%, had negligible effects on the global properties of a structure. Therefore, global methods would be unable to decisively identify the damage. However, simulations and preliminary experimental results showed that the proposed local method was successful in detecting damage within a local joint of the frame. The results showed difficulty, however, in identifying damage when it was simulated at the midspans, where no sensors were placed. This demonstrates the importance of a densely clustered sensor network; a higher density of sensors along the structure translates to a higher resolution picture of the structure's condition.

Experimental results were collected for four different loading types. One of the loading types was chosen as the optimal load for the experiment based on the evaluation accuracy and error terms associated with its data. However, the results were only preliminary and it is recommended that more research be done to find the ideal experimental conditions for the frame. The frame was also instrumented with 6 LVDTs and static testing was performed. The experimental displacements were compared to results for a model given all fixed and then all pinned supports. The experimental results matched neither simulation, but rather fell in between the two, indicating the need for an updated finite element model. However, this updating process is beyond the scope of this research.

The third and final application of the algorithm was an experimental large-scale earthquake moment connection. The connection was instrumented with 5 strain gauges for the purpose of this application and cyclically loaded to failure. Damage observations that were made throughout testing were used as a comparison point for the changes in influence coefficients as damage progressed. It was discovered that throughout the cycle of loading there were four distinct loading conditions, referred to as upward loading, upward unloading, downward loading, and downward unloading. Some of the damage identification was inconsistent between loading conditions, which points to the importance of recognizing the role that damage location and loading type play in damage detection. In certain combinations, they can cause damage to become more prominent or to go unnoticed by the influence coefficients. While data associated with each loading condition captured slightly different behavior of the structure, damage was decisively identified in all four cases. Furthermore, the influence coefficients obtained from the strain data exhibited very high accuracy and negligible error, compared to that of the acceleration data. Strain data was successfully used with the proposed algorithm. Therefore, one of the benefits of the proposed method is its applicability with a variety of common, easy-to-use, and affordable sensor types and loading conditions.

While experimental tests and finite element model simulations have demonstrated the success of each of the localized damage detection method, there is still much to be done in the way of developing this method for application to full-scale, in-situ structures for continuous structural health monitoring. A number of benefits would result from continuous SHM including the abilities to monitor for early detection of damage, make educated decisions about repairs, save on costs, and prevent tragic structural failures.

Furthermore, the proposed local damage detection method could potentially be applied to earthquake-prone structures in order to get instant feedback on the health of a structure immediately following an earthquake load.

Future research should focus on determining the optimal spatial density of the sensor network. Additionally, further experiments should be conducted using the frame, or another experimental prototype, using varied combinations of damage location and severity to more quantitatively infer about the robustness of the method. The possible use of multivariate regression analysis should also be explored for cases in which linear regression does not suitably capture the relationships between nodal responses, such as in nonlinear behavior or cases where there are multiple dominant loading sources. Once the method has been proven extensively in the laboratory setting, a WSN should be deployed for semi-continuous monitoring of an in-situ structure to evaluate the performance of the method in a real-world application. Finally, a damage detection method is only as effective as the sensor network used to monitor the structure. Further research is required to develop a WSN that can realistically and reliably be implemented on real structures for long-term monitoring and to reap the potential benefits of this method.

References

Alvandi, A., and Cremona, C. (2006). “Assessment of vibration-based damage.” Journal of Sound and Vibration 292, 179–202.

American Society of Civil Engineers (2010). “2009 Report Card for America’s Infrastructure.” <http://www.infrastructurereportcard.org>.

Bernal, D., M.ASCE (Jan 2002). “Load Vectors for Damage Localization.” Journal of Engineering Mechanics, 7-14.

Campbell Scientific, Inc. (2005). “Anti-Alias Filter & FFT Spectrum Analyzer Modules.”

Campbell Scientific, Inc. (2009). “CR9000X & CR9000XC Specifications.”

Chang, M. (2010). “Damage detection and modal identification of structural systems using sensor data.” MS thesis, Lehigh University, Bethlehem, PA.

Chang, P. C., Flatau, A., and Liu, S. C. (2003). “Review paper: health monitoring of civil infrastructure.” *Structural Health Monitoring*, 2, 257-267.

Chen, J., and Gupta, A.K. (2000). “Parametric change point analysis,” Birkhäuser, Boston.

Crossbow Technology, Inc. (2007). “MICAz Wireless Measurement System,” San Jose, CA.

Computer and Structures, Inc. (2009). “SAP2000 Educational 14.1.0 Structural Analysis Program,” Berkeley, CA.

Doebling, S.W., Farrar, C.R., and Prime, M.B. (1998). “A Summary Review of Vibration-Based Damage Identification Methods,” The Shock and Vibration Digest 30, 91-105.

Farrar, C.R., Allen, D.W., Ball, S., Masquelier, M.P., and Park. G. (2005). “Coupling Sensing Hardware with Data Interrogation Software for Structural Health Monitoring,” Proc. 6th Int’l Symp. Dynamic Problems of Mechanics, Ouro Preto, Brazil.

Farrar, C.R., Baker, W.E., Bell, T.M., Cone, K.M., Darling, T.W., Duffey, T.A., Eklund, A., and Migliori, A. (1994). “Dynamic characterization and damage detection in the I-40 bridge over the Rio Grande.” *Los Alamos National Laboratory Report*, LA 12767-MS.

Hodgson, I.C, and Ricles, J.M. (2010). “Cyclic Testing of Beam-Column Subassemblages Connected with SidePlate™ Steel Moment Frame Connections.”

Intel Corporation Research (2005). “Intel Mote2 Overview, Version 3.0,” Santa Clara, CA.

Koh, C.G., See, L.M., and Balendra, T. (Aug 1995). “Damage Detection of Buildings: Numerical and Experimental Studies.” J. Struct. Engrg. 121(8), 1155-1160.

Lynch J.P., Loh K.J. (2006). “A summary review of wireless sensors and sensor networks for structural health monitoring,” The Shock and Vibration Digest ISSN 0583-1024, vol. 38, pp. 91-128.

Macro Sensors (2010). “GHSD 750 Series: Spring-Loaded DC-LVDT Position Sensors.” Pennsauken, NJ.

MB Dynamics (1990). “MODAL 50A Vibration Exciter.” Cleveland, OH.

MB Dynamics (2001). “CAL50 Exciter, SL500VCF Amplifier.”

McMaster-Carr (2010). “Tubing.” <http://www.mcmaster.com/#tubing/=br3fe9>.

Morassi, A., and Rovere, N. (1997). “Localizing a Notch in a Steel Frame from Frequency Measurements,” J. Engrg. Mech. 123(5), 422-432.

Omega Engineering, Inc. (2005). “All Stainless Steel “S” Beam Load Cells.” Stamford, CT.

Pakzad, S.N. (2008). “Statistical approach to structural monitoring using scalable wireless sensor networks.” PhD dissertation, University of California, Berkeley.

PCB Piezotronics, Inc. (2004). “Series 3701,3702, and 3801 Capacitive Accelerometers,” Depew, NY.

Quickfilter Technologies, Inc. (2007). “QF4A512 4-Channel Programmable Signal Conditioner,” Allen, TX.

Ratcliffe, C.P. (1997). “Damage Detection Using a Modified Laplacian Operator on Mode Shape Data.” Journal of Sound and Vibration 204(3), 505-517.

Rice, J.A. and Spencer Jr., B.F. (2008). "Structural health monitoring sensor development for the Imote2 platform," Proc. SPIE Smart Structures/NDE.

Rice, J.A. and Spencer, B.F. (2009). "Flexible Smart Sensor Framework for Autonomous Full-scale Structural Health Monitoring," *NSEL Report Series*, No. 18, University of Illinois at Urbana-Champaign. <http://hdl.handle.net/2142/13635>.

Sen, A. and Srivastava, M.S. (1975). "On tests for detecting change in mean." *The Annals of Statistics*, 3, 98-108.

Silicon Designs, Inc. (2010). "Model 2210 Analog Accelerometer Module."

Sohn, H., and Law, K.H. (1997). "A Bayesian Probabilistic Approach for Structure Damage Detection." Earthquake Engineering and Structural Dynamics 26, 1259-1281.

Spectral Dynamics, Inc. (2001). "SigLab User Guide S2022D1/A." San Jose, CA.

Spencer, Jr., B.F. and Agha, Gul (2009). "Illinois Structural Health Monitoring Project". <http://shm.cs.uiuc.edu/software.html>.

STMicroelectronics (2005). "LIS3L02AS4 MEMS Inertial Sensor," Geneva, Switzerland.

Straser, E.G. and Kiremidjian, A.S. (1998). "A Modular, Wireless Damage Monitoring System for Structures," Technical Report 128, John A. Blume Earthquake Engineering Center, Stanford University, Stanford, CA.

Trimm, Marvin. (2003). “An overview of nondestructive evaluation methods.” Journal of Failure Analysis and Prevention 3(3), 17-31.

Yoon, M.K., Heider, D., Gillespie Jr., J.W., Ratcliffe, C.P., and Crane, R.M. (2005). “Local damage detection using the two-dimensional gapped smoothing method.” Journal of Sound and Vibration 279, 119-139.

Vita

Elizabeth Lauren Labuz, daughter of James and Gina Labuz, was born on April 19, 1987 in Evanston, IL. In June 2009, Elizabeth earned a Bachelor of Science in Civil Engineering from the Massachusetts Institute of Technology in Cambridge, MA. Elizabeth began her graduate studies in the Department of Civil and Environmental Engineering at Lehigh University in Bethlehem, PA in August 2009. She will receive her Master of Science in Structural Engineering in May of 2011.